3-22-2012

A Dempster-Shafer Method for Multi-Sensor Fusion

Bethany G. Foley

Follow this and additional works at: https://scholar.afit.edu/etd

Part of the Statistics and Probability Commons

A Dempster-Shafer Method for Multi-Sensor
Fusion

THESIS

Bethany G. Foley, Captain, USAF

AFIT/GAM/ENC/12-03

DEPARTMENT OF THE AIR FORCE
AIR UNIVERSITY

AIR FORCE INSTITUTE OF TECHNOLOGY

Wright-Patterson Air Force Base, Ohio

APPROVED FOR PUBLIC RELEASE; DISTRIBUTION UNLIMITED.

AFIT/GAM/ENC/12-03

A Dempster-Shafer Method for Multi-Sensor Fusion

THESIS

Presented to the Faculty

Department of Mathematics and Statistics

Graduate School of Engineering and Management

Air Force Institute of Technology

Air University

Air Education and Training Command

In Partial Fulfillment of the Requirements for the

Degree of Master of Science

Bethany G. Foley, Captain, USAF, BS

March 2012

AFIT/GAM/ENC/12-03

A Dempster-Shafer Method for Multi-Sensor Fusion

Bethany G. Foley, Captain, USAF, BS

Approved:

/signed/		9 March 2012
Dr. Aihua Wood (Chairman)		Date

/signed/		9 March 2012
Dr. Prabir Bhattacharya (Member)		Date

/signed/		9 March 2012
Dr. Mark Oxley (Member)		Date

AFIT/GAM/ENC/12-03

Abstract

The Dempster-Shafer Theory, a generalization of the Bayesian theory, is based on the idea of belief and as such can handle ignorance. When all of the required information is available, many data fusion methods provide a solid approach. Yet, most do not have a good way of dealing with ignorance. In the absence of information, these methods must then make assumptions about the sensor data. However, the real data may not fit well within the assumed model. Consequently, the results are often unsatisfactory and inconsistent. The Dempster-Shafer Theory is not hindered by incomplete models or by the lack of prior information. Evidence is assigned based solely on what is known, and nothing is assumed. Hence, it can provide a fast and accurate means for multi-sensor fusion with ignorance. In this research, we apply the Dempster-Shafer Theory in target tracking and in gait analysis. We also discuss the Dempster-Shafer framework for fusing data from a Global Positioning System (GPS) and an Inertial Measurement Unit (IMU) sensor unit for precise local navigation. Within this application, we present solutions where GPS outages occur.

Acknowledgements

First and most importantly, I thank my parents, James and Marcia Foley, who through their amazing example taught me what hard work and perseverance really are and that you can never have too many degrees. I thank the AFIT Advanced Navigation Technology (ANT) Center, specifically Major Kenneth Fisher and Dr. John Raquet, who provided me with my thesis data and helped me understand more about navigation systems and sensors. I appreciate Dr. Prabir Bhattacharya and Dr. Mark Oxley for their contributions as thesis committee members. Finally, I thank my thesis advisor, Dr. Aihua Wood. Dr. Wood challenged me academically more than any other professor I have had. I hope I can be as good an instructor as she was.

<div align="right">Bethany G. Foley, Captain, USAF</div>

Table of Contents

A Dempster-Shafer Method for Multi-Sensor Fusion

I. Introduction

In his 1976 book, Glenn Shafer introduced the Theory of Evidence, later referred to as the Dempster-Shafer Theory (DST). This data fusion method is based on the idea of belief and as such can handle ignorance. According to Shafer, this theory was a "reinterpretation of Dempster's work" from the 1960's; whereas, according to Arthur Dempster, Shafer "greatly extended, refined, and recast" his original work [53].

The DST is considered a generalization of the Bayesian Theory. It has been greatly utilized in the fields of computer science and artificial intelligence although it is not widely accepted [28]. However, it is still applied to many of the same problems as the Bayesian and the fuzzy set theories. These three theories are often used as comparisons to one another [3; 5; 14; 40; 41; 50]. In some applications, the DST has even been used in conjunction with other methods, such as particle filters [13; 29; 47; 48].

In the DST, ignorance can be represented. Instead of assigning unknown evidence to prior probabilities, we assign this evidence to 'ignorance'. We can then distinguish between the amount of evidence supporting a proposition and the lack of evidence refuting this proposition [1] or between ignorance and contradiction [63].

In addition, the DST can easily deal with ignorance. Its application is not hindered by incomplete models or by no prior information [30]. We assign evidence based solely on what information we do obtain, and with specific knowledge missing, nothing has to be assumed about the data.

When all of the required information is available, other methods, such as the Bayesian Theory, provide a solid approach for combining evidence. However, most do not have a good way to handle ignorance. For example, the Bayesian Theory requires the prior probabilities to be defined or assumed [30]. The lack of this information

creates a significant problem for data fusion [1; 7]. All of the evidence must still be divided among the hypotheses. How to assign the evidence to each hypothesis becomes an issue [30]. Then the combined evidence often produces unsatisfactory and inconsistent results [1; 5]. As ignorance is already accounted for in the DST, it does not affect the final results.

In the absence of information, many fusion methods and techniques must make assumptions about the sensor or source data. The most common is how the data is modeled. The uncertainty for a sensor is usually modeled as Gaussian, and the error terms from each sensor are assumed to be independent [1; 43; 44; 45]. The problem is that these assumptions tend to work well in theory, but when put into practice become hard to apply. The real sensor data may not fit well within the assumed model [1; 44]. Because the DST does not make these assumptions, it can provide an accurate means for multi-sensor fusion.

For this method, evidence is assigned to belief through a probability mass function. These functions are established by 'expert opinion' [4; 5]. The user can determine them either from experience or through statistical sampling tests. There is much freedom in this determination. One author used hazard detection algorithms and classification and regression trees (CART) to obtain his probability masses [52]. Yet as the results rely greatly on the mass functions, this determination can be a difficult task [4].

The DST has applications in many different areas. A common use is detection. This can include detection of signals, vehicles, ship wakes, objects, fire, and even intrusions in computer systems [5; 7; 8; 13; 24; 39; 48; 65; 66]. Similar to detection, recognition, specifically pattern, object, or target recognition, is a highly applied area [3; 6; 10; 13; 19; 26; 31; 37; 40; 48; 62]. Within the topic of recognition, there is classification. This includes everything from land cover and terrain to target and image classification [24; 31; 34; 37; 50; 51; 52].

Two less common applications for DST are decision-making [2; 9; 14; 19; 28; 51; 55; 59; 62] and navigation for autonomous vehicles with a focus on map building [41; 49; 60; 63]. This method can even be used in medical applications [21; 24; 39; 51]. Finally, one of the least utilized areas, where the DST is still applicable, is location determination [39]. In this research, we demonstrate how the Dempster-Shafer Method can be used to determine the exact location of a moving object and then used along with gait analysis to make an assessment.

Chapter II summarizes the framework of the DST. It also discusses several advantages and disadvantages for this method and provides an illustration for one of its most highly criticized disadvantages. Chapter III presents the tracking of an aircraft's trajectory by two external sensors. Applying two fusion methods, we demonstrate how well this method stands up to a more commonly used method. In Chapter IV we fuse the data from a multi-sensor unit for precise local navigation. Chapter V shows how we can apply the DST in gait analysis for decision-making.

II. Basics

2.1   Framework

According to Shafer, the Dempster-Shafer Theory consists of two theories: a theory of evidence and a theory of probable reasoning. "It is a theory of evidence because it deals with weights of evidence and with numerical degrees of support based on evidence. It is a theory of probable reasoning because it focuses on the fundamental operation of probable reasoning: the combination of evidence" [53, 3].

2.1.1   Theory of Evidence.   Assume there exists a set of n elemental propositions, called the frame of discernment. A proposition can be a hypothesis or a combination of hypotheses [30]. These propositions can contain overlapping and even conflicting hypotheses [23]. However, the frame of discernment, denoted by θ, is a set of mutually exclusive and exhaustive propositions. The power set, 2^θ, is the set of all subsets of θ and the empty set, $\emptyset$ [30].

Given 2^θ, the probability mass function m: $2^\theta \rightarrow [0,1]$, also called the basic probability assignment, represents evidence assigned to a proposition based on the data. The probability mass function has the following properties:

$$m(\emptyset) = 0 \tag{1}$$

$$\sum m(b_j) = 1 \quad \forall \, b_j \, \in \, 2^\theta \tag{2}$$

[53]. Any mass that is not directly assigned to the propositions is assigned to θ, denoted m(θ). This "represents the uncertainty ... concerning the accuracy and interpretation of the evidence" [30, 151].

From the probability mass functions, we obtain the degrees of belief and the degrees of plausibility. The degree of belief is the total evidence in support of or committed to a proposition, measured by the belief function. A belief function over

θ, Bel: $2^\theta \to [0,1]$, is given by

$$Bel(b_i) = \sum_{b_j \subset b_i} m(b_j) \quad \forall\ b_j, b_i\ \in\ 2^\theta. \tag{3}$$

The plausibility function calculates the extent to which the evidence finds a proposition to be credible or plausible. So for a belief function over θ, the plausibility function, Pl: $2^\theta \to [0,1]$, is defined by

$$Pl(b_i) = 1 - Bel(\bar{b}_i) \tag{4}$$

$$= \sum_{b_j \cap b_i \neq \emptyset} m(b_j) \quad \forall\ b_j, b_i\ \in\ 2^\theta \tag{5}$$

where $\bar{b}_i$ is the negation of b_i [53].

With these functions, we define the uncertainty interval for a proposition b_i to be $[Bel(b_i), Pl(b_i)]$ where $Bel(b_i) \leq Prob(b_i) \leq Pl(b_i)$. Here the degrees of belief and of plausibility "show what proportion of evidence is truly in support of a proposition and what proportion results merely from ignorance" [30, 152]. Because of uncertainty in the data, instead of having an exact value for the probability of b_i, there exists a range in which it lies. The length of this interval is called the uncertainty or the ignorance [3; 50]. Thus, when the length is zero, $Prob(b_i) = Bel(b_i)$.

2.1.2   Theory of Probable Reasoning.   Dempster's Rule of Combination is a method to combine evidence from multiple independent sources. More specifically it is used to combine the probability mass functions. Let Bel_A and Bel_B be two belief functions over the same frame of discernment, θ, with probability masses m_A and m_B, respectively. Then the total probability mass committed to proposition c is

$$m(c) = K \sum_{a_i \cap b_j = c} m_A(a_i) * m_B(b_j) \tag{6}$$

where K is the normalizing constant. This function is called the orthogonal sum of Bel_A and Bel_B, denoted $Bel_A \oplus Bel_B$ [53]. This sum can also be denoted $m_A \oplus m_B$ [41] if there is no sum in (6), i.e.,

$$m(c) = K[m_A(a_i) * m_B(b_j)].$$

The normalizing constant, K, "serves as a measure of the extent of the conflict" between the two belief functions [53, 65]. It is defined by

$$K = \frac{1}{1 - \kappa} = \frac{1}{1 - \sum_{a_i \cap b_j = \emptyset}[m_A(a_i) * m_B(b_j)]}. \qquad (7)$$

Here κ is called the degree of conflict between the two belief functions. If Bel_A and Bel_B do not conflict, then $\kappa = 0$. If the functions completely contradict each other, $\kappa = 1$, and $Bel_A \oplus Bel_B$ does not exist [53]. The issues that arise with degrees of conflict are shown in Section 2.3.

Finally, there are usually more than two sources of evidence for a proposition. To combine multiple belief functions, Dempster's Rule is repeatedly applied to pairs of functions. For example, take these four belief functions: Bel_A, Bel_B, Bel_C, and Bel_D. Bel_A and Bel_B are first combined. Then $Bel_A \oplus Bel_B$ is combined with Bel_C, and so on. The final sum is $((Bel_A \oplus Bel_B) \oplus Bel_C) \oplus Bel_D$. However, the order of combination does not matter. The end result will be the same [53].

2.2 Advantages and Disadvantages

Like all fusion methods, the DST has positive and negative aspects in its application. Some aspects make it very useful. Other aspects make it less attractive. These have led people to develop modified or improved methods [19; 57; 61; 66]. Here we briefly discuss the main advantages and disadvantages of the DST.

As stated in Chapter I, this method can represent ignorance. The unknown evidence is not assigned to prior probabilities [1]. Thus, the DST can discern between

the lack of evidence (ignorance) and negative evidence (contradiction) [51; 63]. In the Bayesian Theory, any evidence not assigned to a hypothesis is assigned to its negation [21]. However, this may not be true to the real model. As a result of representing ignorance, the DST has a "freedom of motion." The probability of a proposition is contained within the uncertainty interval; it is not set to a specific value [30].

A similar advantage is accepting incomplete information. As discussed previously, evidence is assigned based on our current knowledge. Prior probabilities and likelihood functions do not have to be known [30]. Also with the lack of knowledge, no assumptions have to be made as real data does not always fit into an assumed model [1].

Another advantage is the use of propositions instead of hypotheses. As Hall points out in [23], this is a major distinction from the Bayesian Theory. In the Bayesian Theory, we can only assign evidence to one hypothesis. In the DST, evidence can be assigned to multiple hypotheses, which make up a proposition. Again these hypotheses can even be conflicting. Thus we are not constrained to assign evidence to mutually exclusive hypotheses but rather have fewer limitations with propositions [23].

A major disadvantage arises in the computation time. The DST tends to be more computationally complex than other methods. "For two or three sensors in a nonparallel implantation, the Dempster-Shafer technique requires approximately twice the computational effort of Bayesian inference" [23, 228]. Recall that probability mass is assigned to elements of a power set. Given a frame of discernment with n elements, the power set has 2^{n-1} elements. So, as n increases, the number of computations required will increase exponentially. However, in most cases not every element in the power set is assigned evidence. The actual significance of the increased computation time is dependent on the specific application. Also other aspects of the DST make it easier to use. Klein explains further in [30].

For the DST, another disadvantage is in dealing with high degrees of conflict. This is also the biggest criticism of this theory, brought to light by Zadeh [40]. In some scenarios, two probability mass functions (or belief functions) highly contradict one another. Thus, κ approaches 1. Consequently, Dempster's Rule of Combination tends to produce counterintuitive and erroneous results [30]. In the next section, we go through an example that shows what can happen with such a case. It should be noted that several authors have argued that Zadeh's criticism is not justified. Mahler proposed that this issue is actually a criticism of Bayes' Rule, not Dempster's [35]. Xiong stated in [58] that this result is caused by the necessary condition of independence not being satisfied. Finally, Haenni concluded the problem is not with Dempster's Rule but rather with misapplication of Dempster's Rule [22].

In summary in the DST, the main advantages are in accepting ignorance and in assigning evidence to propositions. Its disadvantages relate to computation time and problems with high conflict. Despite these disadvantages, it still remains a useful method for multi-sensor fusion as we illustrate in later chapters.

2.3   Degrees of Conflict

The degree of conflict between two belief functions is defined by

$$\kappa = \sum_{a_i \cap b_j = \emptyset} [m_A(a_i) * m_B(b_j)]. \tag{8}$$

If two belief functions do not conflict, then $\kappa = 0$. If the functions completely contradict each other, $\kappa = 1$, and the orthogonal sum does not exist [53]. As κ approaches one, the results from Dempster's Rule are often inaccurate. The following example shows how contradicting beliefs lead to the wrong conclusion. This is often referred to as "Zadeh's paradox" [35].

Based on a patient's symptoms, the evidence supports three possible diagnoses: flu (F), ulcer (U), or internal infection (I). Thus, the frame of discernment is $\theta = \{F, U, I\}$. There are two independent sources of evidence: Doctor A and Doctor B.

Doctor A believes his patient has the flu or an ulcer with probability masses of 0.8 and 0.2, respectively. Doctor B supports a diagnosis of the flu or an internal infection with masses of 0.9 and 0.1, respectively. So the probability masses are m_A(F, U, I)=(0.8, 0.2, 0) and m_B(F, U, I)=(0.9, 0, 0.1). Notice each proposition is mutually exclusive, and the probability masses of A and B each sum to one. In this case, the degrees of belief equal their probability masses.

The unnormalized results of applying Dempster's Rule are shown in Table 1. Adding up the empty sets, $\kappa = 0.28$. After normalizing, $[m_A \oplus m_B](F) = 1$ and, thus, $[Bel_A \oplus Bel_B](F) = 1$. So the diagnosis, or proposition, of flu is determined to be true with a low degree of conflict.

Table 1: Case 1 Low Conflict

	m_A(F) = 0.8	m_A(U) = 0.2	m_A(I) = 0
m_B(F) = 0.9	m(F) = 0.72	m(∅) = 0.18	m(∅) = 0
m_B(U) = 0	m(∅) = 0	m(U) = 0	m(∅) = 0
m_B(I) = 0.1	m(∅) = 0.08	m(∅) = 0.02	m(I) = 0

Now suppose Doctors A and B still support the same diagnoses but with different probability masses: m_A(F, U, I)=(0.2, 0.8, 0) and m_B(F, U, I)=(0.1, 0, 0.9). Table 2 shows the unnormalized orthogonal sums of the masses. In this example, $\kappa = 0.98$. After normalizing, $m_A \oplus m_B$(F) is still equal one. So the patient is again diagnosed with the flu, but the degree of conflict between the two doctors is very high.

Table 2: Case 2 High Conflict

	m_A(F) = 0.2	m_A(U) = 0.8	m_A(I) = 0
m_B(F) = 0.1	m(F) = 0.02	m(∅) = 0.08	m(∅) = 0
m_B(U) = 0	m(∅) = 0	m(U) = 0	m(∅) = 0
m_B(I) = 0.9	m(∅) = 0.18	m(∅) = 0.72	m(I) = 0

In combining the evidence, both cases result in the same diagnosis, the flu. Yet, in Case 2, both doctors considered this to be a very unlikely cause. With a high

degree of conflict, Dempster's Rule produced an erroneous diagnosis. However, the Dempster-Shafer Method performed well when the degrees of conflict were lower [1].

III. External Tracking

3.1 Introduction

In this chapter, we demonstrate how the Dempster-Shafer Method compares to the Kalman filter, a more commonly used method. We take multiple sensors placed separately across a space. The sensors may or may not generate the same amount of noise. As an object moves into the space, the sensors individually track it and report its position over a given time. Then we must apply a fast and accurate method to combine all of the sensor data.

Many fusion methods produce excellent results if information is known or assumed about the sensor or its data. The Kalman filter is one such method. It is used "to fuse dynamic low-level redundant data in real-time." This filter assumes that the noise generated by the sensors is independent Gaussian with mean zero and standard deviation σ' [1, 41].

However, in many cases, this information is not available or is incomplete. Also the real sensor data may not fit well within the assumed model [1]. As stated in Chapter I, the DST does not require prior knowledge to combine evidence. The probability mass function is merely determined by the user. Nothing else is required to be known.

The sensor data used in this chapter was generated through a MATLAB program. The code was provided by Major Kenneth Fisher from the AFIT Advanced Navigation Technology (ANT) Center. The MATLAB program generates a random trajectory of an object. Then it adds noise to corrupt the true measurements, producing two new measurements. These new values are the sensors' outputs. The noise is actually modeled as Gaussian with a specific standard deviation. This standard deviation, denoted σ_i, is considered the sensor's error and can be changed within the program.

In the following, we used the DST and the Kalman filter to combine the two sensors' data. For the Dempster-Shafer Method, we made no assumptions about the

data. We chose to assign the probability masses by (11) and (12), but these equations were not the only option. We did, however, assume knowledge of the sensors' errors, σ_i. Yet, this would not hinder the use of the DST if these errors were not known.

3.2 Scenario

An aircraft is moving across the space with a constant speed. Two external sensors are tracking its position. Each sensor returns the measured range in meters and the measured angle in radians to the aircraft as a function of time. Over a 30 second window, the sensors return the measured positions every 0.2 seconds. Laid out on a grid, Sensor 1 is located at (0, 30), and Sensor 2 is at (0, -30) in Cartesian coordinates. In addition, each sensor has a range error associated with it, denoted by $\sigma_i > 0$ for $i \in \{1, 2\}$.

Because this scenario was simulated, the true position of the aircraft is always known. For each case, this simulation was run multiple times to complete a Monte Carlo analysis. The number of runs varies depending on the case. See Table 3.

Since each measurement is relative to the location of the sensors, a common point of reference was needed. Thus, the polar coordinates were converted to Cartesian coordinates $\mathbf{x} = (x_1, x_2)$. The sensor errors for the new coordinates were then assumed to be the same as the range error. Let $\mathbf{x}_{t,1}$ and $\mathbf{x}_{t,2}$ be the position measurements at time t from Sensor 1 and Sensor 2, respectively. Thus, $\mathbf{x}_{t,i} = \mathbf{x}_{t,\text{ACTUAL}} + \mathbf{n}_{t,i}$, where $\mathbf{x}_{t,\text{ACTUAL}}$ is the actual position of the aircraft and $\mathbf{n}_{t,i}$ is the noise from Sensor i.

3.3 Approach

To combine the position measurements from the two sensors, we had four different approaches. Each is denoted Kalman, DST True, DST Mean, or DST Mean Mod. For the last three approaches, we used the Dempster-Shafer Method, but each approach had slightly different probability mass and, thus, a different result. Then

with the four approaches, we evaluated five cases with different variances and different numbers of runs. The cases are shown in Table 3.

Table 3: The Five Different Cases

CASE #	# OF RUNS	σ_1	σ_2
1	8	2	4
2	10	2	2
3	30	2	4
4	30	2	2
5	30	2	8

Table 4 defines the subscript indicators that are used for the variables in this chapter. Note that all of the variables use indicators j and t. If an indicator is not used, then it is not applicable to that particular variable. In many cases, indicators i and l will not be used at the same time. If indicator k is not shown, then all of the variables are from the same run.

Table 4: Variable Subscript Indicators

Indicator	Meaning	Input
j	coordinate	1, 2
t	time	1-149
i	sensor	1, 2
l	approach	KAL, TRUE, MEAN, MEAN MOD
k	run #	1-30

For a comparison to the Dempster-Shafer Method, a Kalman filter was applied to the sensor data. As this data was originally generated to implement navigation filters, the Kalman filter provided a good method for data fusion and for comparison. Then as the code was designed, the measurement noises were modeled as independent Gaussian with mean zero and variance σ_i^2. Note this variance is equal to the sensor range error squared. Thus, the combined position for the Kalman approach is given by

$$x_{j,t,KAL} = \frac{\sigma_2^2}{\sigma_1^2 + \sigma_2^2} \, x_{j,t,1} + \frac{\sigma_1^2}{\sigma_1^2 + \sigma_2^2} \, x_{j,t,2} \tag{9}$$

13

and the combined variance becomes [1]

$$\sigma^2 = \frac{\sigma_1^2 \sigma_2^2}{\sigma_1^2 + \sigma_2^2}.$$ (10)

With the formulas for the Kalman filter established, we moved on to applying the DST. For the probability masses, we have two propositions: aircraft present (A) and aircraft not present (N). Thus, the frame of discernment is $\theta = \{A, N\}$, and the power set is $2^\theta = \{\emptyset, A, N, A \cup N\}$. Then the probability mass functions are defined as follows:

$$m_{j,t,i,l}(A) = \frac{1}{\sqrt{2\pi}\sigma_i} \exp\left(-\frac{(x_{j,t,i} - \mu^*)^2}{2\sigma_i^2}\right),$$ (11)

$$m_{j,t,i,l}(N) = 1 - m_{j,t,i,l}(A).$$ (12)

The total probability masses become:

$$m_{j,t,l}(A) = K * [m_{j,t,1,l}(A) * m_{j,t,2,l}(A)],$$ (13)

$$m_{j,t,l}(N) = K * [m_{j,t,1,l}(N) * m_{j,t,2,l}(N)],$$ (14)

where K, the normalizing constant, was calculated by (7). Note the degrees of belief are equal to their probability masses, i.e. $Bel_{j,t,l}(A) = m_{j,t,l}(A)$.

For the parameter, σ_i^2, required in (11), the squared error of Sensor i was used. Since the variance of total probability mass of A, $m_{j,t,l}(A)$, improves, the combined variance was calculated by (10).

Then μ^* was set in two different ways for the DST True and the DST Mean approaches. The first μ^*, denoted $\mu_{j,t,TRUE}$, is equal to the actual position, $x_{j,t,ACUTAL}$. Again because this was a simulation, this value was known. However, in most cases, this information would not be available. The results using first μ^* served as yet another comparison for the latter results. By having knowledge of the true position, we were able to improve the definitions of the probability mass functions for the situations where $x_{j,t,ACTUAL}$ is unknown. For the DST Mean approach, μ^*, denoted

14

$\mu_{j,t,MEAN}$, was calculated as the average of the sensor measurements for all of the simulation runs. So

$$\mu_{j,t,i,MEAN} = \frac{1}{N} \sum_{k=1}^{N} x_{j,t,i,k}. \tag{15}$$

Then for the total probability mass, $\mu_{j,t,MEAN}$ is the average of the $\mu_{j,t,1,MEAN}$ and $\mu_{j,t,2,MEAN}$.

Each of the five cases was completed two times using $\mu_{j,t,TRUE}$ and $\mu_{j,t,MEAN}$. The results of the total probability mass using $\mu_{j,t,MEAN}$, denoted $x_{j,t,MEAN}$, were then compared to the positions determined from the Kalman filter, $x_{j,t,KAL}$, and from the total probability mass using $\mu_{j,t,TRUE}$, denoted $x_{j,t,TRUE}$. Finally, after going through each run, we averaged the results for each case, called the Averaged Run. Thus $x_{j,t,l,\text{AVG}} = \frac{1}{N} \sum_{k=1}^{N} x_{j,t,l,\text{k}}$.

While evaluating Case 1, we noticed that several of the total probability masses, $m_{2,t,MEAN}(A)$, were equal to zero or one. So $m_{2,t,MEAN}(A)$ produced infinite or undefined values for the aircraft's position, $x_{2,t,MEAN}$. This may have been due to the precision within the MATLAB function used. To resolve this issue, the probability masses were modified to be the following:

$$m^*_{j,t,MEAN}(A) = \begin{cases} m_{j,t,MEAN}(A) - 10^{-16}, & \text{if } m_{j,t,MEAN}(A) = 1 \\ m_{j,t,MEAN}(A) + 10^{-16}, & \text{if } m_{j,t,MEAN}(A) = 0 \\ m_{j,t,MEAN}(A), & \text{otherwise.} \end{cases} \tag{16}$$

Another problem arose in evaluating Case 2 Run 5. In the Figure 1, the plot shows how $\mathbf{x}_{t,MEAN}$ cuts through the middle of the true trajectory, $\mathbf{x}_{t,\text{ACTUAL}}$. This clearly indicated that the total probability mass, $m^*_{2,t,MEAN}$, produced weak results over these times. Similar problems occurred in other cases, as well. Table 5 lists these runs.
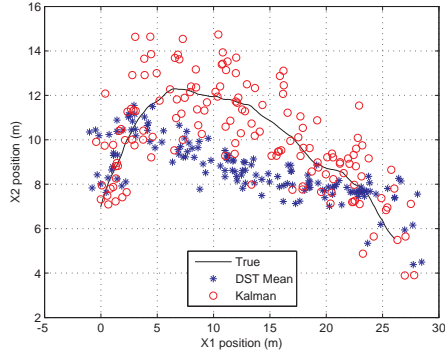
Figure 1: Case 2 Run 5 - Problem Run

Table 5: Problem Runs

CASE #	RUN #
1	NONE
2	5
3	17, 25, 30
4	1, 5, 9, 11, 14, 27, 28
5	30

To resolve this, we again had to make modifications to the probability mass functions. First, a determination had to be made about at which times the mass functions generated bad outputs. To do so, an error value was calculated by taking the absolute difference between the average of the two sensor measurement positions and the result from the Dempster-Shafer Method,

$$error_{j,t} = |\frac{1}{2}(x_{j,t,1} + x_{j,t,2}) - x_{j,t,MEAN}|. \tag{17}$$

Notice that this error was completed for both the x_1 and the x_2 coordinates. As hinted earlier, many of the points were off in only one of these axes.

Figure 2 shows the error values for Run 5. The errors for x_1 are all less than one, but for x_2 the errors spike in the middle with the largest values at $t \in [7, 18]$. Based on these values, we chose to examine times that had errors greater than 2, denoted α, for Case 2 Run 5. Using the same process, α was determined for other problematic

16

runs. They are listed in Table 6. Notice α values were set for all of the runs. Thus, if $\text{error}_{j,t} > \alpha$, then $\text{m}_{j,t,i,MEAN}$ was changed, regardless of whether or not the run was problematic.
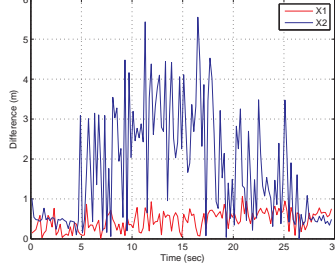

Figure 2: Case 2 Run 5 Error Values

Table 6: Alpha Values

CASE #	RUN #	α
2	ALL	2
2	2	1
3	ALL	4
3	17, 25	2
3	30	1.5
4	ALL	2
4	27, 28	1
5	ALL	2

Rather than modifying (11), μ^* was changed from (15) to the average of the absolute value of sensor measurements for all of the simulation runs. So the new μ^* is

$$\mu_{j,t,i,MEAN\ MOD} = \frac{1}{N} \sum_{k=1}^{N} |x_{j,t,i,k}|, \tag{18}$$

and $\mu_{j,t,MEAN\ MOD} = \frac{1}{2}(\mu_{j,t,1,MEAN\ MOD} + \mu_{j,t,2,MEAN\ MOD})$. This approach is called DST Mean Mod. Again this modification only affected the x_j-coordinate if $\text{error}_{j,t} > \alpha$. In many cases, only one x_j-coordinate was changed, not both. The results using this new μ^* are denoted $x_{j,t,MEAN\ MOD}$.

Like $m_{2,t,MEAN}(A)$, $m_{j,t,MEANMOD}(A)$ was equal to one or zero at several points. Thus, the probability masses were modified using the same equations that are in (16). The new mass is then denoted $m^*_{j,t,MEANMOD}(A)$.

After initially setting the α values based on error$_{j,t}$ and evaluating $\mathbf{x}_{t,\text{MEAN MOD}}$, several of the problematic runs did not show improved results. So the α values were modified; this change is already reflected in Table 6. Although Case 2 Run 2 was not a problematic run, its α value was changed, as well.

As this approach was applied to all of the runs, most of the runs also showed improvement. However, several, shown in Table 7, did not. For these runs, μ^* was not changed even if the error values exceeded α.

Table 7: Unmodified Runs

CASE #	RUN #
1	ALL
3	1, 7, 10, 15, 16, 26
5	2, 5, 9, 15, 20, 21, 25, 26, 27, 28

We have outlined the four different approaches to combine our sensor data: Kalman, DST True, DST Mean, and DST Mean Mod. Note that for the DST Mean Mod approach, if any case's runs used $\mu_{j,t,MEAN\ MOD}$, then all of the results for that case are denoted $\mathbf{x}_{t,\text{MEAN MOD}}$. So in some of the runs, $\mathbf{x}_{t,\text{MEAN MOD}} = \mathbf{x}_{t,\text{MEAN}}$. Note that often the results of the approaches are referred to by the name of the approach only, instead of $\mathbf{x}_{t,l}$. Section 3.5 provides the results for each case.

3.4   Comparison Techniques

With the positioning results from each run, we used three comparison techniques to provide indications on how well each approach performed against the others. Every comparison was completed for the individual runs and the Averaged Runs. Note that not every run is shown in Section 3.5, but every run was examined.

We first compared the three results by plotting the points on the same graph with the true position, $x_{j,t,ACTUAL}$. These are referred as Point Plots. We looked for position results for DST Mean Mod (or DST Mean for Case 1) to follow the same general path as the true aircraft. Also, if the points diverged from the true track, we looked to see if the same trend existed for the Kalman position measurements.

Next, the differences between the actual position and the combined positions were plotted, called Difference Plots. The difference was calculated by the Euclidean norm of the difference of the pairs,

$$\sqrt{(x_{1,t,l} - x_{1,t,ACTUAL})^2 + (x_{2,t,l} - x_{2,t,ACTUAL})^2}.$$

Two Difference Plots were produced for each run. One compared Kalman and DST Mean Mod (or DST Mean), and the other compared DST True and DST Mean Mod (or DST Mean). For these plots, we looked for the differences for DST Mean Mod (or DST Mean) to be less than or close to the other differences. Also, the differences for DST Mean Mod (or DST Mean) should have followed a similar increasing/decreasing trend, and finally, they should not have had any significant deviations from other approaches except the occasional spike.

Finally, we found the Mean Average Deviation (MAD) and the Mean Square Error (MSE), where

$$MAD_l = \frac{1}{n} \sum_{t=1}^{n} \sqrt{(x_{1,t,l} - x_{1,t,ACTUAL})^2 + (x_{2,t,l} - x_{2,t,ACTUAL})^2}$$

$$MSE_l = \frac{1}{n} \sum_{t=1}^{n} ((x_{1,t,l} - x_{1,t,ACTUAL})^2 + (x_{2,t,l} - x_{2,t,ACTUAL})^2).$$

Here, we looked for DST Mean Mod (or DST Mean) values to be less than DST True and preferably Kalman. If they were not, then the MAD and the MSE for DST Mean Mod (or DST Mean) should have been close to Kalman. Finally, if again the values for DST Mean Mod (or DST Mean) were not smaller than Kalman, the

difference between the DST Mean Mod (or DST Mean) and the Kalman should have been smaller than the difference between DST Mean Mod (or DST Mean) and DST True.

3.5 Results

3.5.1 Case 1. For Case 1, the errors, σ_i, for Sensor 1 and Sensor 2 were set to 2 and 4, respectively. Eight runs were completed. Figure 3 shows the position measurements, $\mathbf{x}_{t,i}$, for six of the runs. Since Sensor 2 has a larger error, its measurements were further from the true position, $\mathbf{x}_{t,\mathrm{ACTUAL}}$, than those of Sensor 1. Figure 4 shows the measurements for the Averaged Run.
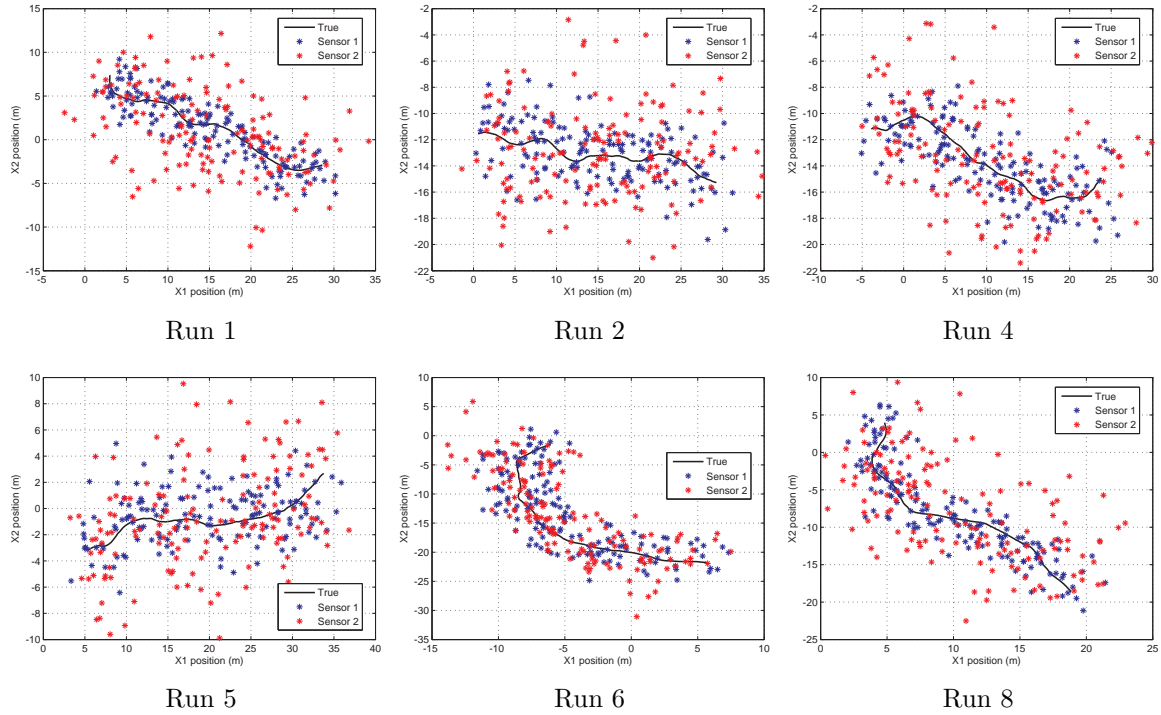
Figure 3: Case 1 Sensor Measurements

As there were no problematic runs, the DST Mean Mod approach was not used for Case 1. So we applied the following three: Kalman, DST True, and DST Mean. With the results, we examined the Point Plots, the Difference Plots, and the MAD and the MSE values for the individual runs and the Averaged Run.
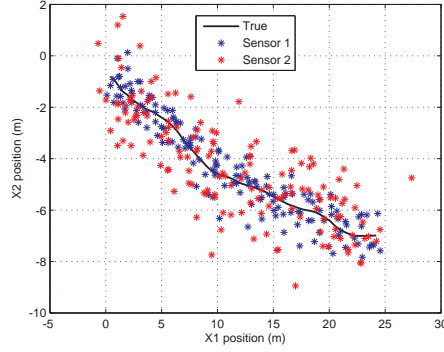
Figure 4: Case 1 Averaged Sensor Measurements

The Point Plot for Case 7 is shown in Figure 5. The DST Mean points followed the true trajectory of the aircraft. Its results were similar to those for DST True and Kalman. Also DST Mean had the same clustering of points as the others specifically for $x_1 \in [17, 22]$. The other runs in Case 1 had similar plots.
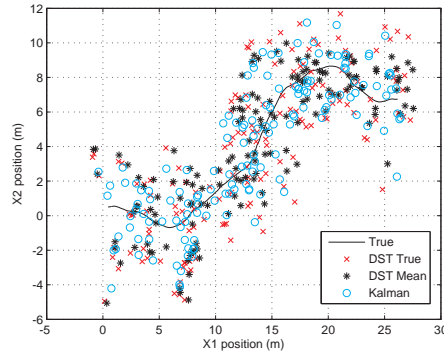

Figure 5: Run 7 Point Plot

The Difference Plots for Run 7 are shown in Figure 6. For the most part, the differences for the Kalman approach were smaller than those for the DST Mean. However, there were still many instances where DST Mean was smaller. Also DST Mean followed the same trend as Kalman. The plot for DST True and DST Mean showed the reversal of the previous plot. At almost every time t, the DST Mean had smaller differences than DST True, and spikes occurred at the same times t. So we saw what we had expected. Again for the other runs, the same patterns were present.

21

Kalman   DST True
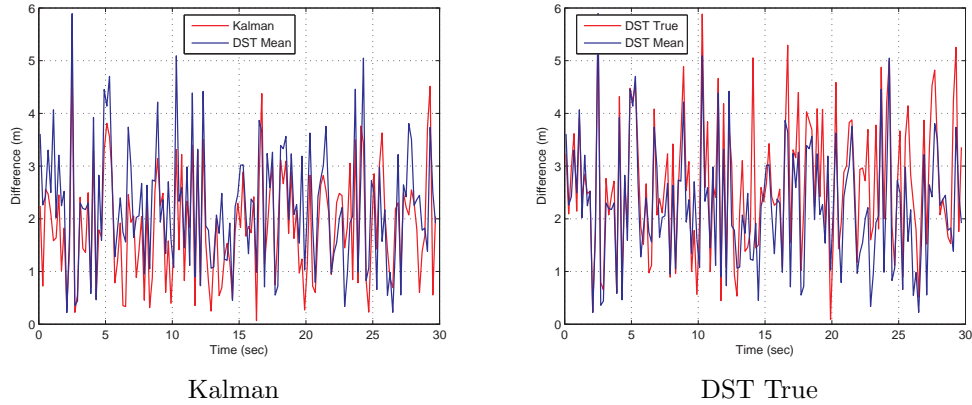
Figure 6: Run 7 - Difference Plots

Figure 7 shows the Point Plot for the Averaged Run. We can see that DST Mean had very good results. The points followed closely along the true trajectory and were similar to the position measurements for the other approaches. Except for a few points, such as $\mathbf{x} \approx (16, -7.5)$, DST Mean provided solid positioning data.
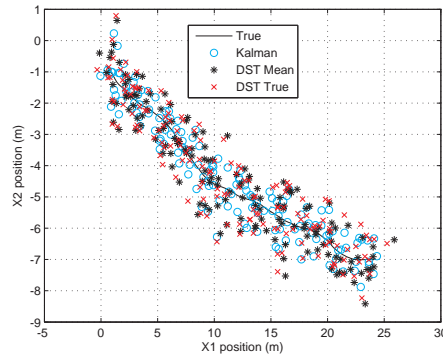

Figure 7: Averaged Run

The differences for the Averaged Run are shown in Figure 8. Here we saw similar results to the individual runs except the differences were smaller values. The DST Mean differences were slightly greater than the Kalman, with significant spikes around t = 14, 19, and 29, but again both differences presented a similar trend. For the other plot, DST Mean had slightly smaller differences than DST True, but they still had the same trend. DST True even had spikes around t = 14, 19, and 29.
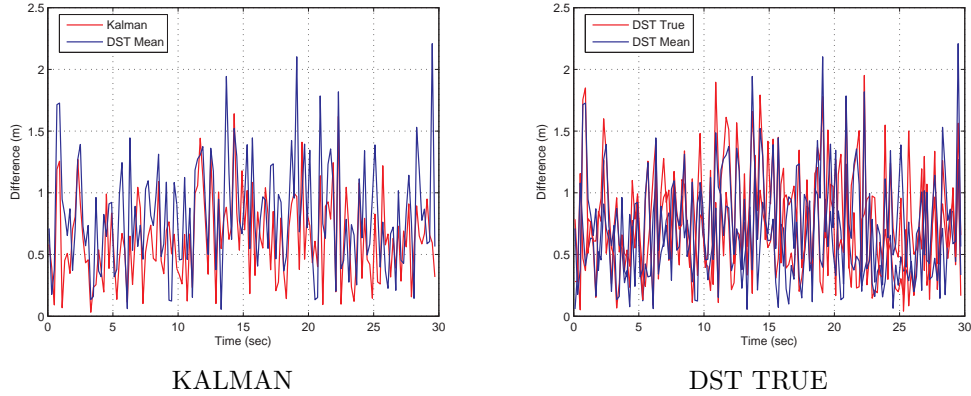
22

| KALMAN | DST TRUE |

Figure 8: Averaged Run - Difference Plots

After examining the plots, we compared the values for the MAD and the MSE in Table 8. For the individual runs, both values for DST Mean were smaller than DST True but larger than Kalman. However, in half of the runs, the MAD's for the DST Mean were closer to the Kalman value than to the DST True, and in all but Runs 5 and 8, the MSE values were closer. For example, in Run 3, the difference between DST Mean MAD and Kalman MAD was 0.1587, but the difference between DST Mean and DST True was 0.5946.

For the Averaged Run, all of the values decreased significantly. Yet based on the Point Plot, this decrease was expected. The MAD values for Kalman, DST True, and DST Mean were 0.6268, 0.8456, and 0.8205, respectively. The MSE was 0.5102 for Kalman, 0.9062 for DST True, and 0.8653 for DST Mean. For both values, we had DST Mean less than DST True but still greater than Kalman. According to these values, the DST Mean approach provided a slightly improved result to DST True. While Kalman still had smaller values, all of the MAD and the MSE values were very similar.

Table 8: Case 1-MAD/MSE Values

			DST	
RUN #	MEASURE	KALMAN	TRUE	MEAN
1	MAD	1.7870	2.5372	2.0790
	MSE	4.1199	7.9433	5.6830
2	MAD	1.9787	2.6386	2.1695
	MSE	4.9544	8.4459	6.0358
3	MAD	1.8180	2.5713	1.9767
	MSE	4.3538	8.1536	5.0067
4	MAD	1.8172	2.3856	2.1551
	MSE	4.1316	6.9015	5.8396
5	MAD	1.8474	2.4699	2.2011
	MSE	4.4920	7.6822	6.2921
6	MAD	1.9980	2.5860	2.0629
	MSE	5.0641	8.2987	5.2934
7	MAD	1.8561	2.6433	2.2406
	MSE	4.4915	8.5819	6.2995
8	MAD	1.8298	2.4427	2.3100
	MSE	4.3190	7.4400	6.6446
AVG	MAD	0.6268	0.8456	0.8205
	MSE	0.5102	0.9062	0.8653

3.5.2 Case 2. For Case 2, the sensors' errors, σ_1 and σ_2, were both set to 2. Then ten runs were completed. Figure 9 shows the position measurements, $\mathbf{x}_{t,i}$, for a sample of the runs. Unlike the previous case, the measurements for the sensors showed a similar spread. One did not appear worse than the other. Figure 10 shows the measurements for the Averaged Run.

For Case 2, we had one problematic run: Run 5. Because of this, we used the DST Mean Mod approach, in addition to the other three. Again in some runs, $\mathbf{x}_{t,\text{MEAN MOD}} = \mathbf{x}_{t,\text{MEAN}}$. As with Case 1, we looked at the Point Plots, the Difference Plots, and the MAD and the MSE values for the individual runs and the Averaged Run.
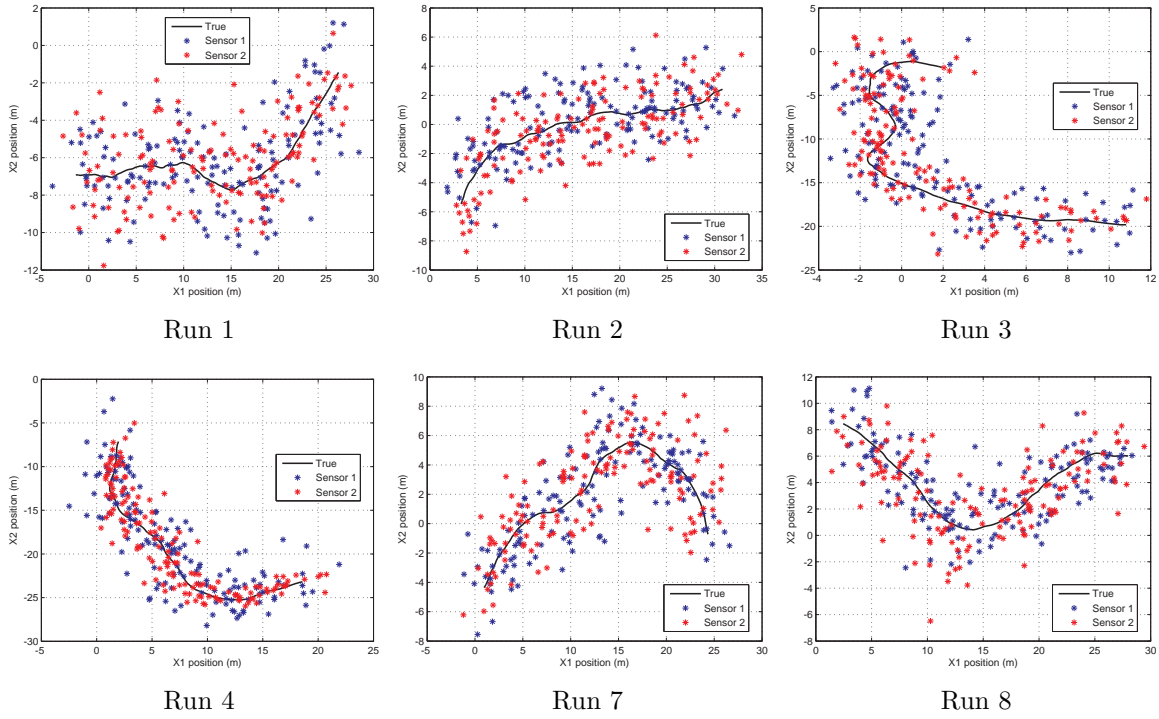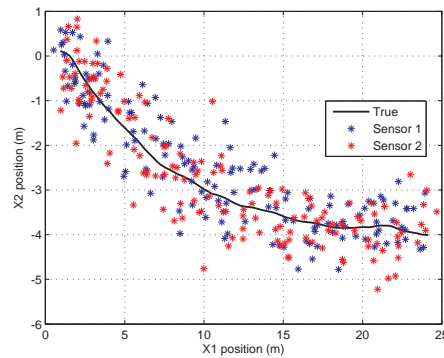
Figure 9: Case 2 Sensor Measurements

Figure 10: Case 2 Averaged Sensor Measurements

The Point Plots for Runs 2 and 10 are shown in Figure 11. Notice how more of the DST Mean Mod points fell slightly above but still followed the True line. Yet, these points were similar to those for Kalman and DST True. Also, there were no obvious deviations from the true trajectory. The other runs in Case 2 had similar plots.
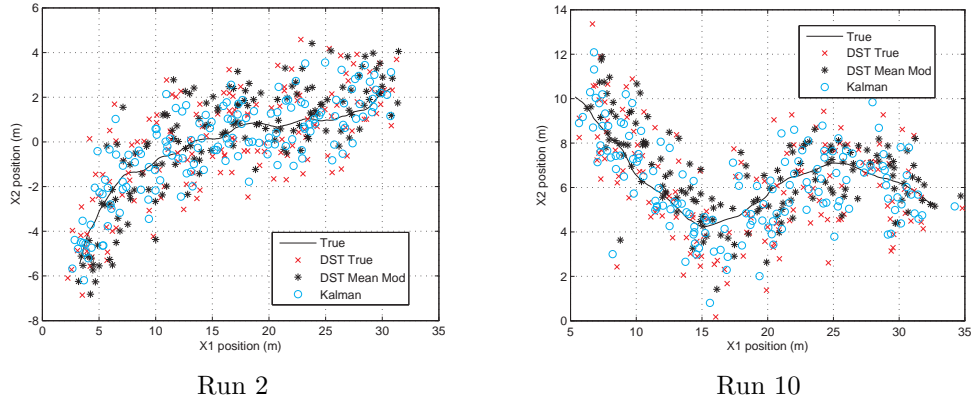
Run 2   Run 10

Figure 11: Case 2 Point Plots

The Difference Plots are shown in Figures 12 and 13 for Runs 2 and 10. For the first plot with Kalman, the differences for both methods had the same trend. For most of the times t where DST Mean Mod had a large spike, Kalman did too. Again for the most part, the Kalman differences were slightly less than the DST Mean Mod. For Run 2, the DST Mean Mod differences were not as good as Run 10. However, in the second plot with DST True, there still was significant improvement from DST True to DST Mean Mean. At almost every time t, DST Mean Mod was smaller than DST True. The other runs had similar results.

Kalman   DST True
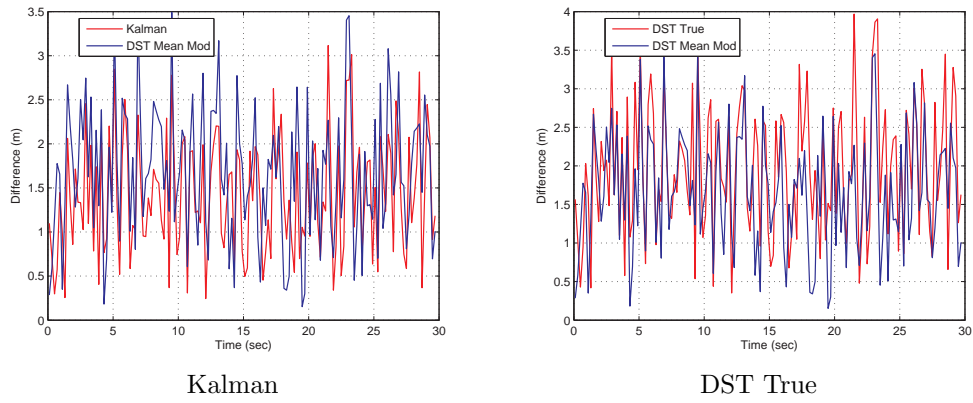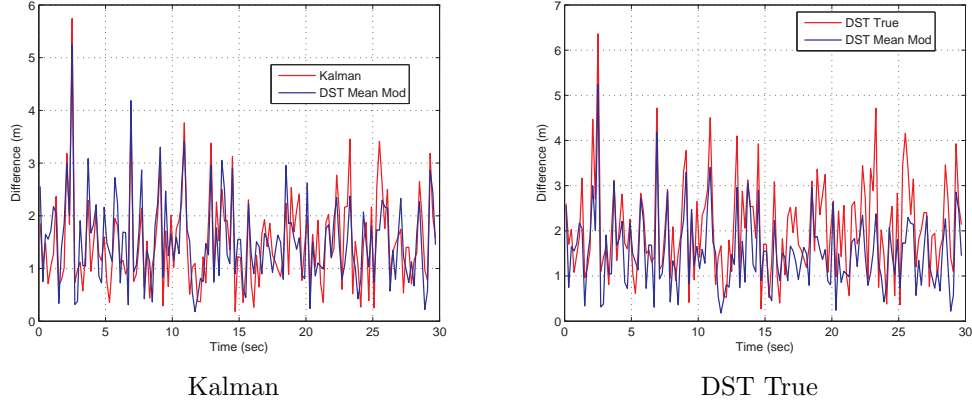
Figure 12: Run 2 - Difference Plots

Figure 13: Run 10 - Difference Plots

As previously mentioned, Run 5 had poor results using $\mu_{j,t,MEAN}$. This is clear in the Before Plots in Figures 14 and 15. The DST Mean results fell well below but run parallel to the actual position, and the differences formed an arch above the Kalman differences. Also, the DST Mean MAD increased from 2.1670 for DST True to 2.2353, and in every other run, this value decreased. Then the MSE value went from 5.7576 to 6.0238.
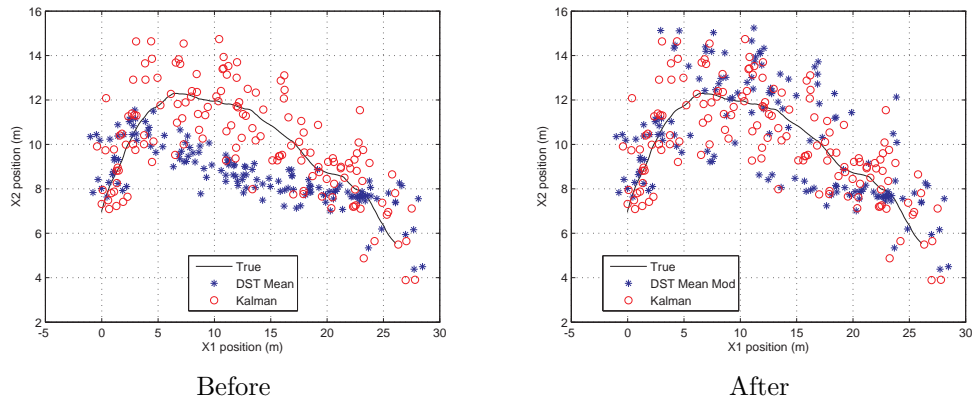

Figure 14: Run 5 - Point Plot

Thus, based on the Error Plot in Figure 16, α was set to 2 , and $\mathrm{m}^*_{j,t,i,MEAN\ MOD}$ was calculated. The change is very evident in the After Plots. The differences for DST Mean Mod no longer had the large jump for the middle times. Although there were still some spikes around t = 12, 21, and 25, there were similar patterns as the
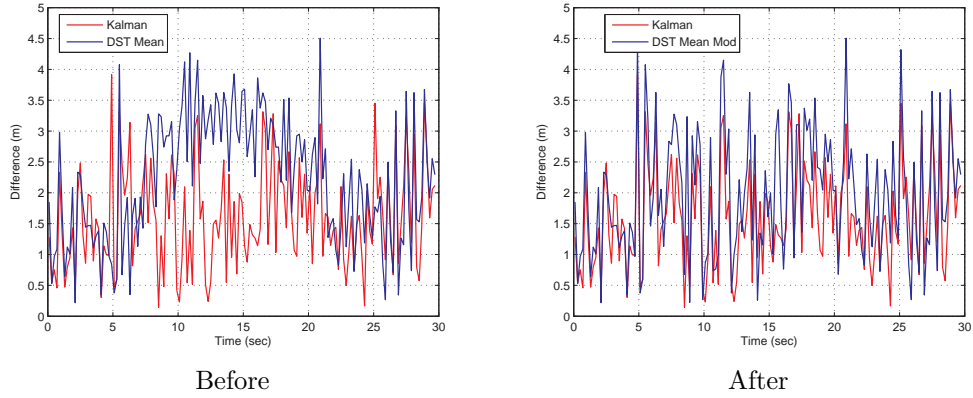
| Before | After |

Figure 15: Run 5 - Difference Plot

other Difference Plots. Finally, the MAD and the MSE values decreased to 1.9725 and 4.9349, both below the values for DST True. Therefore, we got the improvement expected from using the DST Mean Mod approach.
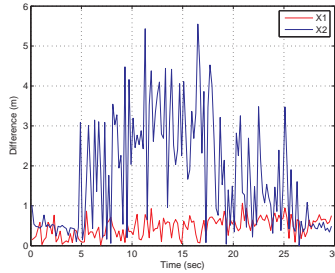

Figure 16: Case 2 Run 5 Error Plot

In addition to the improvements in Run 5, Run 2 also improved from using the DST Mean Mod approach. Recall for Run 2, α was set to 1 instead of 2. For the remaining eight runs, the errors for $x_{j,t,MEAN}$ did not exceed the α threshold. The results from these two improved runs positively affected the Averaged Run. Notice the subtle changes in the two Point Plots in Figure 17. In the Before Plot, there was a larger DST Mean grouping below the true path after $x_1 = 9$, but, in the After Plot, the positions for DST were more evenly spread around the true position and closer to the Kalman results. This change can also be seen in the Difference Plots for the Averaged Run in Figure 18. Note that the plots have a different scale. In the After Plot, many of the large spikes for DST Mean decreased or disappeared. At t = 11,

28

the spike decreased from 1.8 to 1.5 and became equal to the Kalman difference. Also notice the grouping of spikes at $t \in [16, 23]$ that decreased, as well. Thus, these two runs improved the Averaged Run.
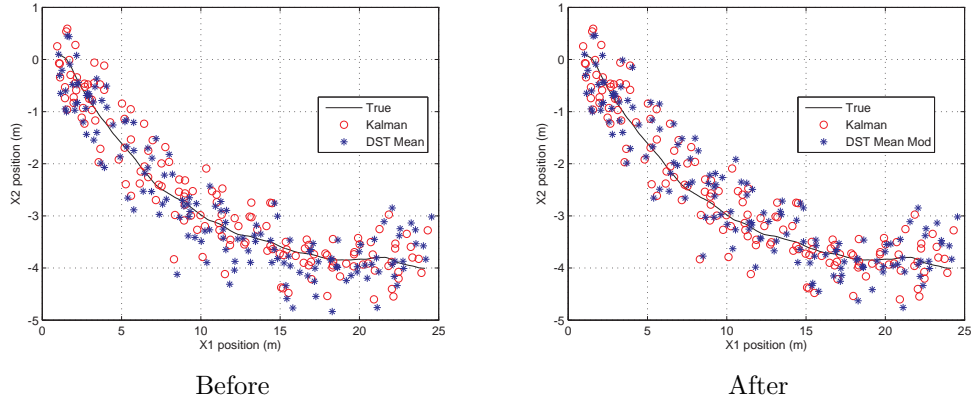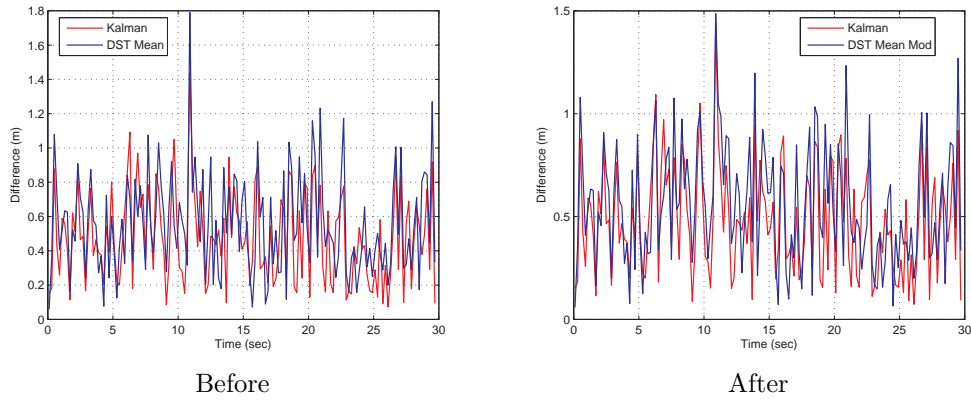

Figure 17: Averaged Run - Point Plot

Figure 18: Averaged Run - Difference Plot

Again only Runs 2 and 5 changed between the DST Mean and the DST Mean Mod approach. NO CHANGE in Table 9 indicates this. However, there was still a decrease in values from DST True to DST Mean for all of the runs. For example, Run 3's MAD went from 1.9266 to 1.5498 and became closer to the Kalman value of 1.4115.

For the Averaged Run, we got slightly different results. From DST Mean to DST Mean Mod, there was a small increase in the MAD and the MSE. The MAD

went from 0.5561 to 0.5604. Similarly the MSE increased from 0.3936 to 0.3973. Note that these increases were less than 1%. Also, both were still less than the DST True values and closer the Kalman values. In addition, the Point Plots and Difference Plots indicated improvement from Mean to Mean Mod, so there did not appear to be a problem with the DST Mean Mod approach. It still provided a good result.

Table 9: Case 2-MAD/MSE Values

				DST	
RUN #	MEASURE	KALMAN	TRUE	MEAN	MEAN MOD.
1	MAD	1.4542	1.9998	1.7706	NO CHANGE
	MSE	2.5905	4.7672	3.8512	NO CHANGE
2	MAD	1.4137	1.9620	1.6834	1.6693
	MSE	2.4353	4.5678	3.4060	3.3588
3	MAD	1.4115	1.9266	1.5498	NO CHANGE
	MSE	2.6945	4.7487	3.3166	NO CHANGE
4	MAD	1.4307	1.9759	1.5651	NO CHANGE
	MSE	2.7783	5.1077	3.2210	NO CHANGE
5	MAD	1.5961	2.1670	2.2353	1.9725
	MSE	3.2275	5.7576	6.0238	4.9349
6	MAD	1.4226	1.9464	1.5498	NO CHANGE
	MSE	2.6245	4.7627	3.1645	NO CHANGE
7	MAD	1.4937	2.0398	1.8306	NO CHANGE
	MSE	2.8541	5.1140	4.2218	NO CHANGE
8	MAD	1.4950	2.0564	1.6328	NO CHANGE
	MSE	2.8873	5.2720	3.3334	NO CHANGE
9	MAD	1.4261	1.9620	1.7790	NO CHANGE
	MSE	2.5784	4.7170	4.0041	NO CHANGE
10	MAD	1.4973	2.0398	1.5206	NO CHANGE
	MSE	2.9701	5.2365	2.9677	NO CHANGE
AVG	MAD	0.4811	0.6490	0.5561	0.5604
	MSE	0.3004	0.5456	0.3936	0.3973

3.5.3 Case 3.   For Case 3, the errors, σ_i, for Sensor 1 and Sensor 2 were set to 2 and 4, respectively. Then thirty runs were completed. This was done as a comparison to Case 1 to see if increased number of runs would show better results. Figure 19 shows the position measurements, $\mathbf{x}_{t,i}$, for a sample of the thirty runs. Because Sensor 2 has a larger error, note that its measurements were further from the

true position, $x_{t,ACTUAL}$. Then Figure 20 shows the measurements for the Averaged Run.
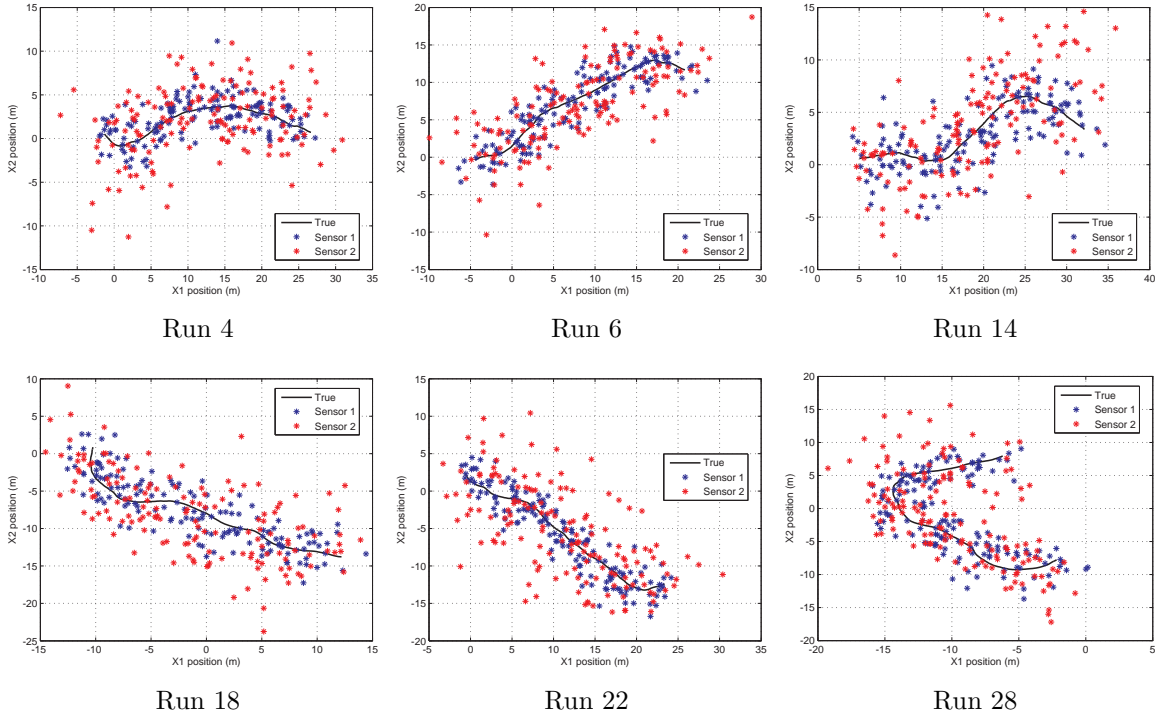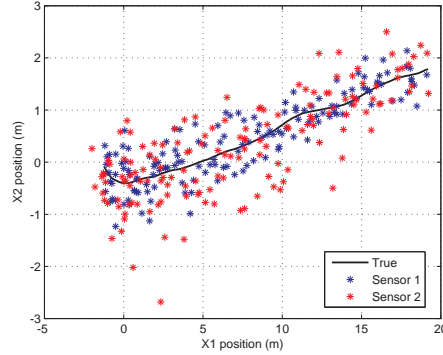

Figure 19: Case 3 Sensor Measurements

Figure 20: Case 3 Averaged Sensor Measurements

For Case 3, we had three problematic runs: Run 17, Run 25, and Run 30. Because of this, we used the DST Mean Mod approach. As before, depending on the run, $\mathbf{x}_{t,\text{MEAN MOD}}$ may have equaled $\mathbf{x}_{t,\text{MEAN}}$. Then unless specified $\alpha = 4$. Also for this case, several runs did not improve when using the DST Mean Mod approach. So

even if $\text{error}_{j,t} > \alpha$, the following runs were not modified: 1, 7, 10, 15, 16, and 26. The three problem runs are examined after the Difference Plots.

The Point Plots for Runs 2 and 5 are shown in Figure 21. In Run 2, all of the approaches' points formed a tight grouping around the True line, and the points for DST Mean Mod and Kalman clustered at the same places. In Run 5 all three points were more scattered, but DST Mean Mod had better results than the other two. Notice its points formed a slightly tighter grouping along the true trajectory than Kalman's. The other runs in Case 3 had similar plots to these two.

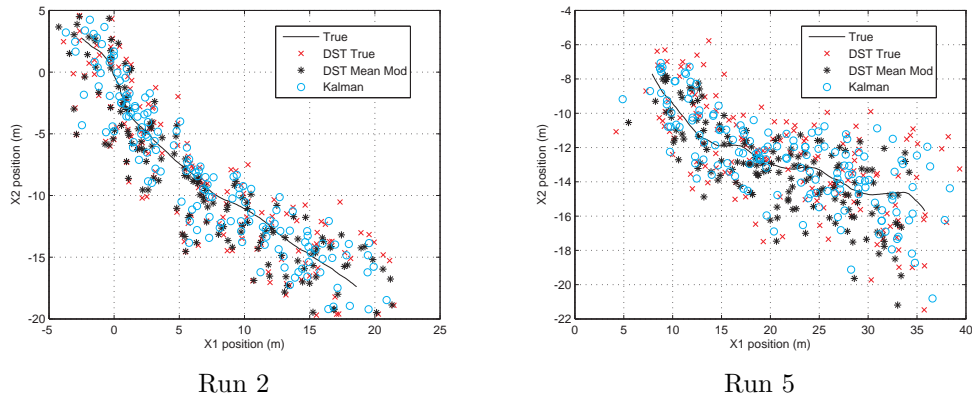Run 2   Run 5

Figure 21: Case 3 Point Plots

The Difference Plots are shown in Figures 22 and 23. For the first plot, the differences for both methods had the same trend. DST Mean Mod and Kalman had spikes at most of the same times t. In Run 5 DST Mean Mod appeared to have more smaller differences while in Run 2 Kalman's differences were smaller over the most times t. Yet, the Point Plot for Run 2 showed better results than Run 5. In the Difference Plots with DST True, the usual patterns existed. The differences for DST Mean Mod were less than DST True. In Run 5, there was a significant decrease in value from DST True to DST Mean Mean. In other run, there was not as much of a decrease but still a decrease. For the remaining 28 runs, there were similar results with some closer to Run 2 and others closer to Run 5.
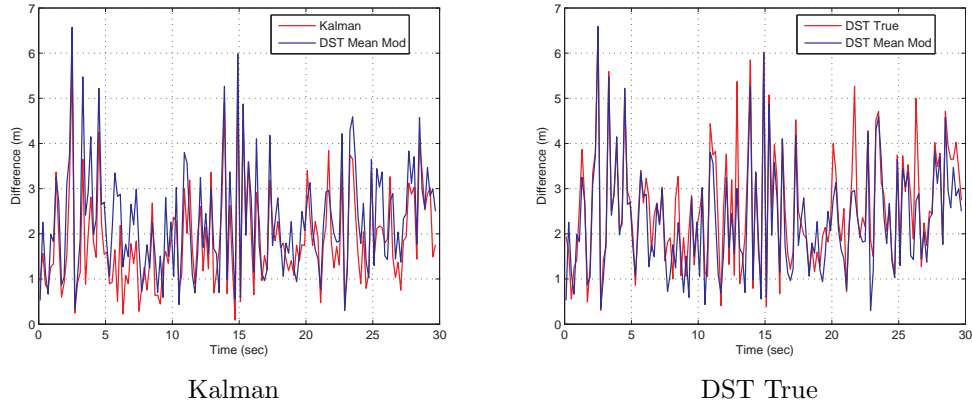
Kalman   DST True

Figure 22: Run 2 - Difference Plots

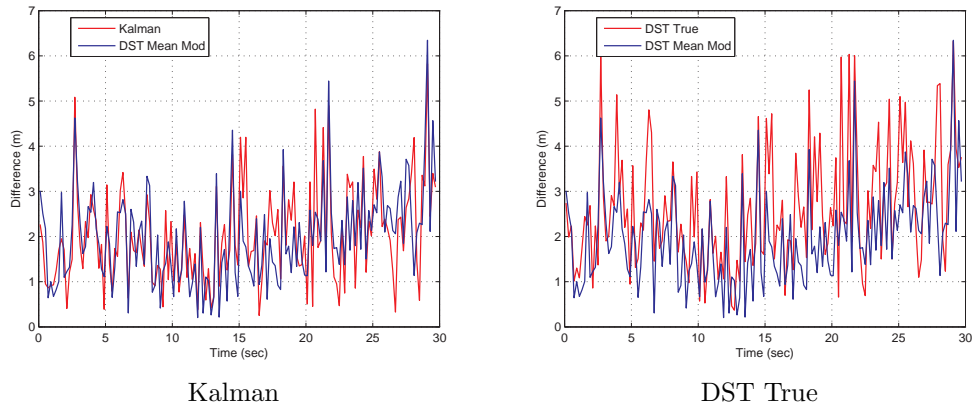Kalman   DST True

Figure 23: Run 5 - Difference Plots

As previously mentioned, Runs 17, 25, and 30 had poor results using $\mu_{j,t,MEAN}$. This is clear the Before Plots in Figures 24 - 29. For Run 17 in the Point Plot, $\mathbf{x}_{t,MEAN}$ seemed to level off at $x_2 = 16$, and in the Difference Plot, the DST Mean values curved up after t = 24. Run 30 had the same trend but more severe. For Run 25, the Point Plot showed a large grouping of $\mathbf{x}_{t,MEAN}$ above the $\mathbf{x}_{t,ACTUAL}$ at $x_1 \in [15 - 25]$, and the Difference Plot had an arch at $t \in [7, 17]$. Despite the obvious problems indicated in the plots, the MAD and the MSE values for the first two runs did not increase from DST True to DST Mean, but in Run 30 there was a fairly significant increase. The MAD went from 2.4535 to 3.2294 and the MSE from 7.2419 to 13.9755.
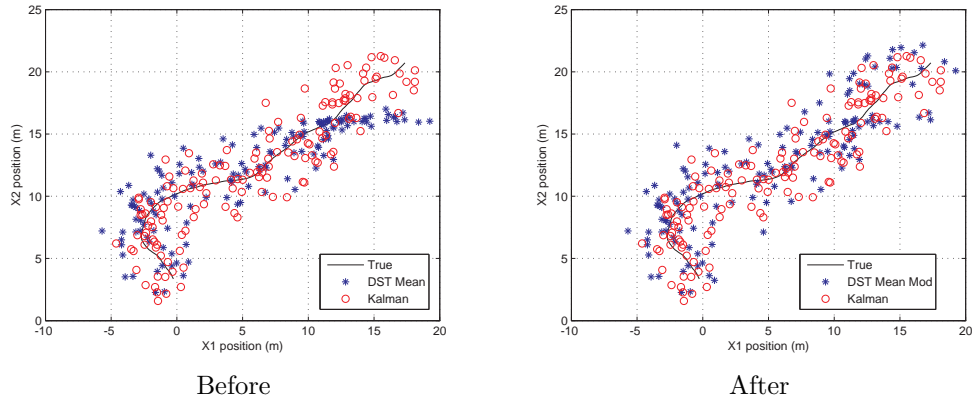
33

Before   After

Figure 24: Run 17 - Point Plot

Before   After

Figure 25: Run 17 - Difference Plot

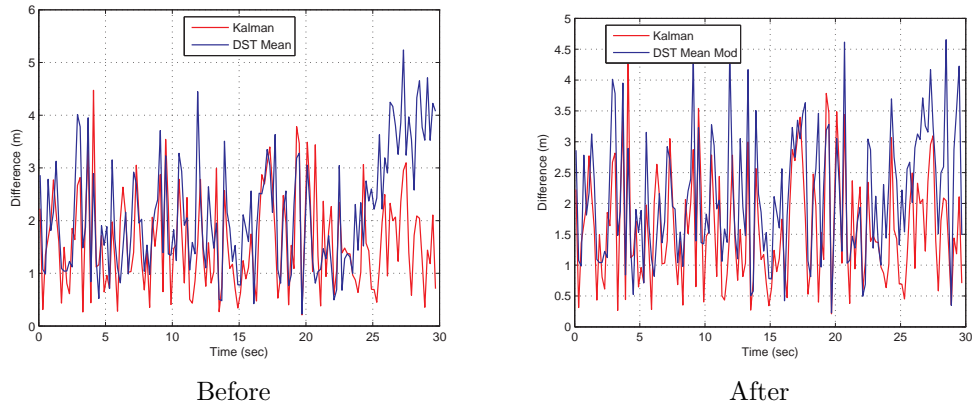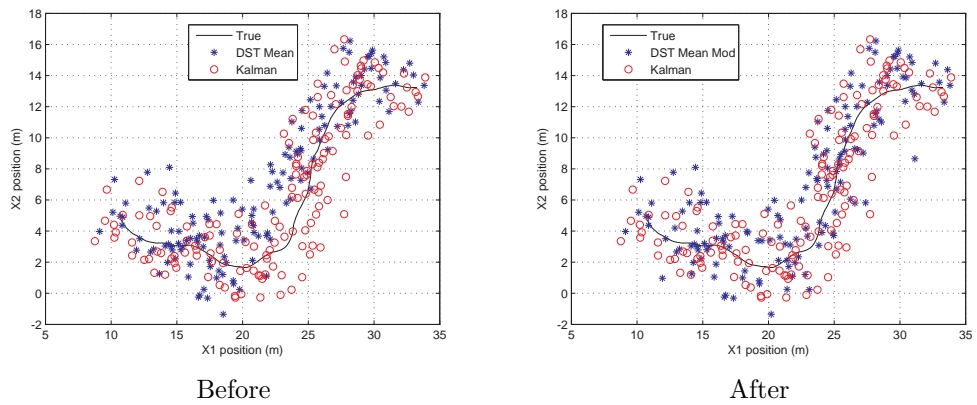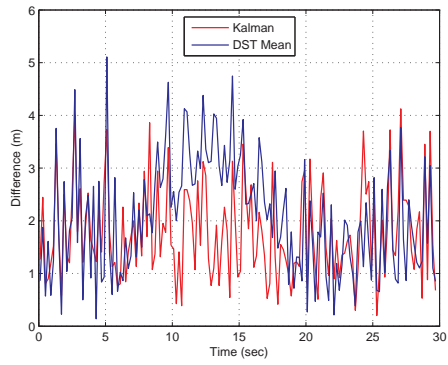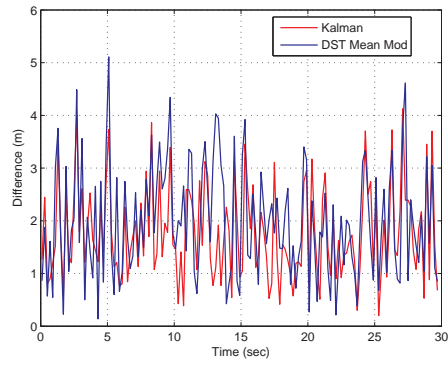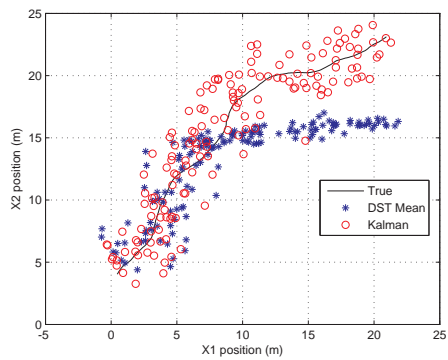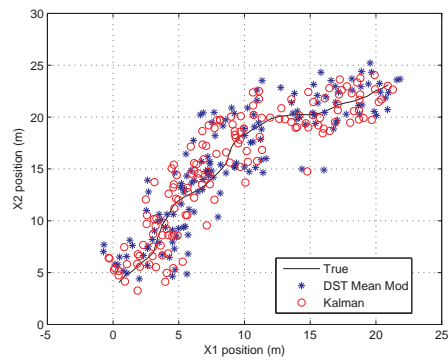Before   After

Figure 26: Run 25 - Point Plot

34

Figure 27: Run 25 - Difference Plot
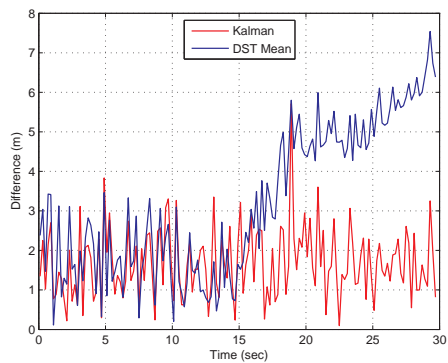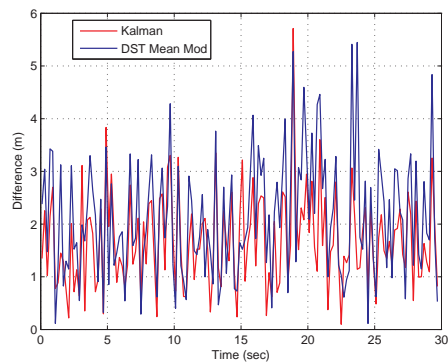

Figure 28: Run 30 - Point Plot

Figure 29: Run 30 - Difference Plot

Recall the discussion in Section 3.3 where α was slightly modified for more accurate results. Based on this and the Error Plots in Figure 30, $\alpha = 2$ for Runs 17 and 25, and $\alpha = 1.5$ for Run 30. Notice for Runs 17 and 30, $error_{2,t}$ was significantly larger than the other, and for Run 30, $error_{1,t}$ was larger. With this, $m^*_{j,t,i,MEAN\ MOD}$ was calculated. The change is very evident in the After Plots. So $\mathbf{x}_{t,MEANMOD}$ no longer diverged from the actual trajectory and formed a tighter grouping. Also the differences for DST Mean Mod no longer had large jumps or arches over the Kalman differences. Although there still were some spikes, more so in Run 17, similar patterns appeared as seen in the non-problematic runs. Finally, all of the values for the MAD and the MSE decreased in each run. However, Run 30 significantly dropped to 2.1222 for the MAD and 5.8125 for the MSE. The other values are listed in Table 10.

| Run 17 | Run 25 | Run 30 |
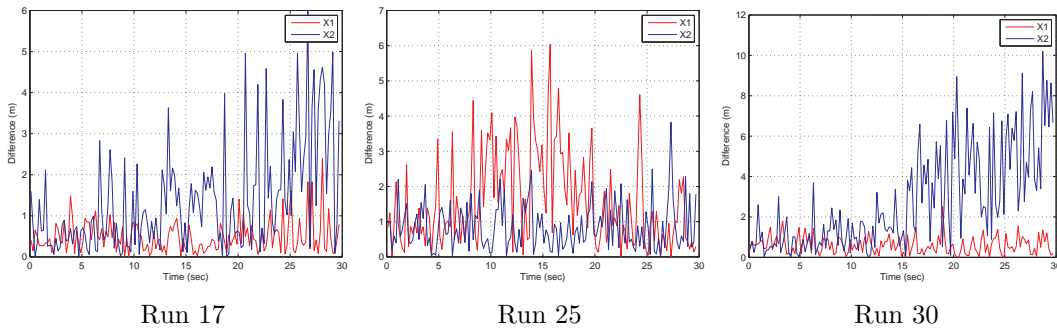
Figure 30: Case 3 - Error Plots

In addition to the problematic runs, several other runs showed improvement from using the DST Mean Mod approach. They are indicated in Tables 10 and 11. We saw that the results from all of the improved runs again positively affected the Averaged Run. In Figure 31, the After Point Plot shows a tighter grouping for DST Mean Mod, and the values were closer to the actual. Particularly notice the points below the True line. Except for a few outlying points, all moved up closer to the line. In Figure 32, the After Difference Plot also shows the improvement. The largest decreases were at $t \in [15, 20]$ and $t \in [24, 30]$. However, the four large spikes still exist in the After Plot. These correspond to the four major outlying points seen in the Point Plot.

Before   After
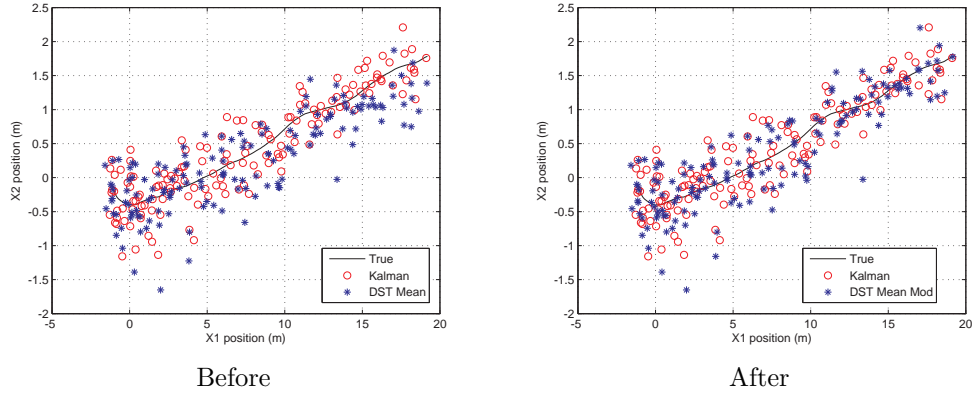
Figure 31: Averaged Run - Point Plot

Before   After
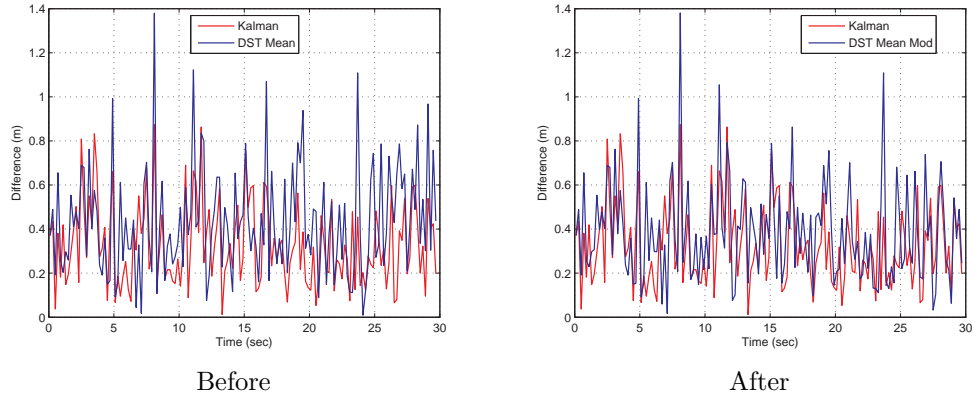
Figure 32: Averaged Run - Difference Plot

The MAD and the MSE values for Case 3 are listed in Tables 10 and 11. In some of the runs, the errors for $x_{j,t,MEAN}$ did not exceed the α threshold. NO CHANGE indicates this. Also NA indicates the purposely unmodified runs, mentioned in Table 7. Among all of the runs, we saw a decrease in values from DST True to DST Mean or DST Mean Mod. Also in most of the runs, the MAD and the MSE values for the final DST method were closer to the Kalman values than to the DST True values. In Run 1, the MSE was even less than the Kalman.

For the Averaged Run, notice the values were significantly smaller than those in Case 1. The increased number of runs improved the results for every approach. Because of the problem runs, the MSE for the DST Mean increased from 0.2459 to 0.2483, but the MAD did not. It slightly changed from 0.4359 to 0.4348. However,

37

both values for DST Mean Mod did decrease to 0.3877 for MAD and 0.2010 for MSE. Again neither were smaller than the Kalman, but all the values were very close together.

Table 10: Case 3-MAD/MSE Values

			DST		
RUN #	MEASURE	KALMAN	TRUE	MEAN	MEAN MOD.
1	MAD	1.7850	2.5984	1.7638	NA
	MSE	4.0879	8.2231	3.9217	NA
2	MAD	1.8706	2.5647	2.2813	NO CHANGE
	MSE	4.6031	8.2004	6.6323	NO CHANGE
3	MAD	1.9331	2.5808	2.2881	NO CHANGE
	MSE	4.9441	8.5165	6.8480	NO CHANGE
4	MAD	1.7958	2.4871	2.3151	NO CHANGE
	MSE	4.3172	7.8514	6.7731	NO CHANGE
5	MAD	2.0169	2.6353	2.0201	1.9950
	MSE	5.2295	8.7032	5.2345	5.0822
6	MAD	1.6727	2.3711	2.1356	NO CHANGE
	MSE	3.6806	7.2079	5.7310	NO CHANGE
7	MAD	1.7860	2.6309	1.8884	NA
	MSE	4.3772	8.8052	4.7483	NA
8	MAD	1.6664	2.4112	2.1155	NO CHANGE
	MSE	3.7657	7.3619	5.6868	NO CHANGE
9	MAD	1.8194	2.4351	2.1569	NO CHANGE
	MSE	4.5143	7.5526	6.2350	NO CHANGE
10	MAD	1.7694	2.5281	2.1650	NA
	MSE	4.2507	8.0447	5.8663	NA
11	MAD	1.8412	2.5286	2.0452	2.0416
	MSE	4.4500	8.0086	5.4763	5.4514
12	MAD	1.6759	2.5074	2.0604	NA
	MSE	3.8710	8.1109	5.8232	NA
13	MAD	1.9058	2.5617	2.0890	2.0881
	MSE	4.5364	7.9886	5.7343	5.7335
14	MAD	1.9772	2.7190	2.2578	NO CHANGE
	MSE	5.2073	9.2093	6.3594	NO CHANGE
15	MAD	1.7020	2.4510	1.8247	NA
	MSE	3.9159	7.5972	4.5661	NA
16	MAD	2.0715	2.6832	2.2116	NA
	MSE	5.3821	8.9582	6.2883	NA

Table 11: Case 3-MAD/MSE Values (cont.)

| RUN # | MEASURE | KALMAN | DST | | |
			TRUE	MEAN	MEAN MOD.
17	MAD	1.5899	2.3413	2.1451	2.1176
	MSE	3.3426	6.9255	5.8034	5.5190
18	MAD	1.8501	2.4634	2.0980	2.0940
	MSE	4.5027	7.6928	5.6886	5.6812
19	MAD	1.6473	2.3342	2.0461	NO CHANGE
	MSE	3.6045	6.9024	5.3230	NO CHANGE
20	MAD	1.8575	2.4802	2.0307	NO CHANGE
	MSE	4.6257	7.9737	5.8447	NO CHANGE
21	MAD	1.8365	2.6406	2.0850	NO CHANGE
	MSE	4.4394	8.4232	5.5977	NO CHANGE
22	MAD	1.8027	2.4729	2.2021	NO CHANGE
	MSE	4.1508	7.5592	6.1950	NO CHANGE
23	MAD	1.7165	2.3004	1.9272	1.9245
	MSE	3.9523	6.6892	5.0595	5.0316
24	MAD	1.8942	2.6901	2.2858	NO CHANGE
	MSE	4.6789	8.8159	6.7208	NO CHANGE
25	MAD	1.7664	2.4821	2.0776	1.9769
	MSE	3.8955	7.5207	5.5010	5.0341
26	MAD	1.9931	2.7201	2.3724	NA
	MSE	5.0843	8.9256	6.7993	NA
27	MAD	1.9526	2.5849	2.2164	NO CHANGE
	MSE	4.9460	8.2385	6.2563	NO CHANGE
28	MAD	1.8958	2.5238	2.0674	NO CHANGE
	MSE	4.4195	7.6982	5.3690	NO CHANGE
29	MAD	1.6550	2.2806	2.1223	NO CHANGE
	MSE	3.6214	6.5452	5.8159	NO CHANGE
30	MAD	1.6803	2.4535	3.2294	2.1222
	MSE	3.5930	7.2419	13.9755	5.8125
AVG	MAD	0.3284	0.4359	0.4348	0.3877
	MSE	0.1426	0.2459	0.2483	0.2010

3.5.4   Case 4.   For Case 4, the errors, σ_i, for both Sensor 1 and Sensor 2 were set to 2. Then thirty runs were completed. This was done as a comparison to Case 2. Figure 33 shows the position measurements, $\mathbf{x}_{t,i}$, for a sample of the runs. Because the sensors had the same error, their outputs were similar. One's measurements did not appear further from the true position, $\mathbf{x}_{t,i,ACTUAL}$, than the other's. Figure 34 shows the measurements for the Averaged Run.
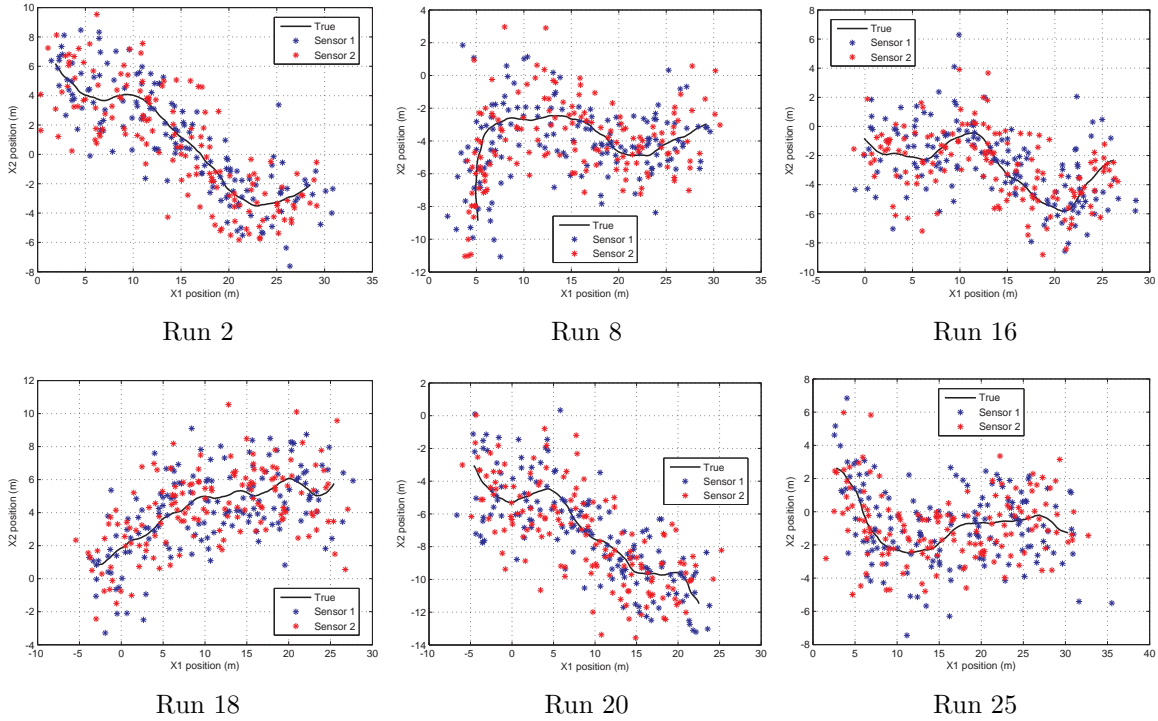
Figure 33: Case 4 Sensor Measurements

Figure 34: Case 4 Averaged Sensor Measurements
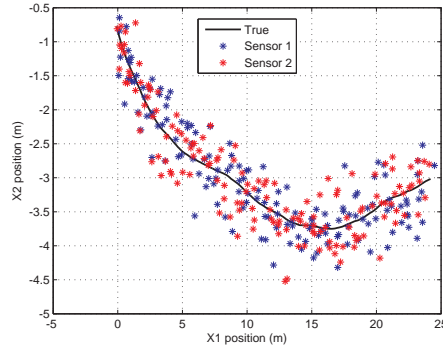
For Case 4, there was an increase in problematic runs. Runs 1, 5, 9, 11, 14, 27, and 28 produced poor results from DST Mean. Thus, all four approaches were used. Unless specified in Table 7, $\alpha = 2$. Again depending on the run, $\mathbf{x}_{t,\text{MEAN MOD}}$ may have been equal to $\mathbf{x}_{t,\text{MEAN}}$. The problem runs are explained after the Difference Plots.

Figure 35 shows the Point Plots for Runs 3 and 12. Clearly $\mathbf{x}_{t,\text{MEAN MOD}}$ for Run 3 showed better results than for Run 12. In Run 3, the DST Mean Mod points were very similar to the Kalman points, and many of these were closer to the actual, $\mathbf{x}_{t,\text{ACTUAL}}$. In Run 12 all of the points were more spread out. We see the DST Mean Mod were again close to but not as good as the Kalman points. The remaining runs in Case 4 had similar plots to these two.

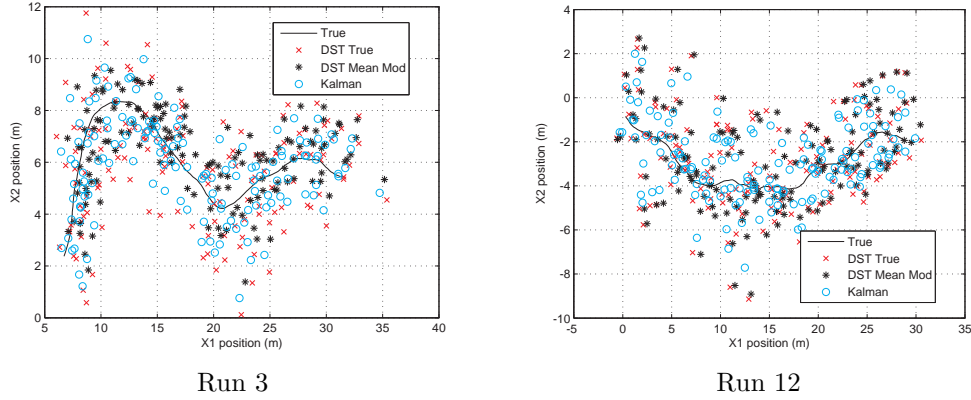Run 3   Run 12

Figure 35: Case 4 Point Plots

The Difference Plots are shown in Figures 36 and 37. For both plots, we had the same patterns as with the other cases. The three approaches showed similar trends. Again Run 3 had slightly better results for DST Mean Mod. Runs 12 did not have as strong of results. For the most part, the differences for DST Mean Mod were larger than the Kalman but smaller than those for DST True. Also all of the approaches seemed to have large spikes at the same times t. The remaining runs had similar results to Runs 3 and 12.

Runs 1, 5, 9, 11, 14, 27, and 28 were problematic runs. This is clear in the Before Plots in Figures 38 - 41. Note that Run 9 is evaluated later. Because of the similarities between the plots of Runs 1, 5, 11, 14, and 28, only Run 1 is shown. For these runs, the $\mathbf{x}_{t,\text{MEAN}}$ values leveled off around $x_2 = 9$, and in the Difference Plots, the DST Mean values increasingly diverged as time t increased. Then Run 27 was very similar to Case 2 Run 5. Instead of following the true aircraft path, $\mathbf{x}_{t,\text{MEAN}}$ cut

41

Kalman   DST True
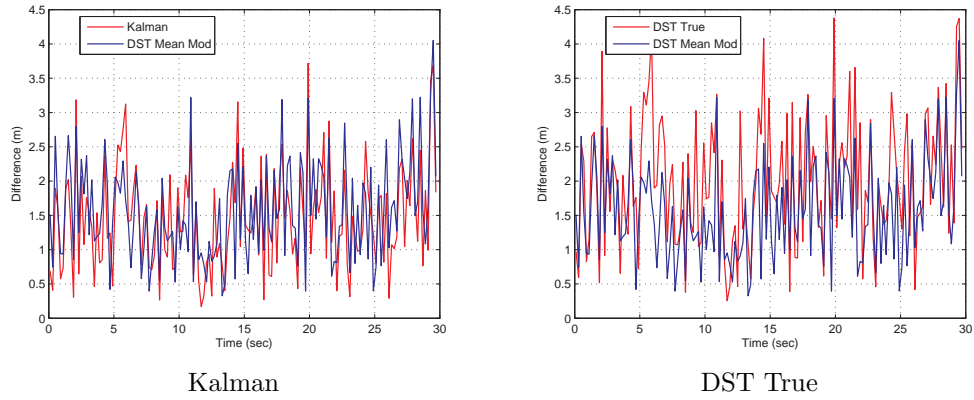
Figure 36: Run 3 - Difference Plots

Kalman   DST True
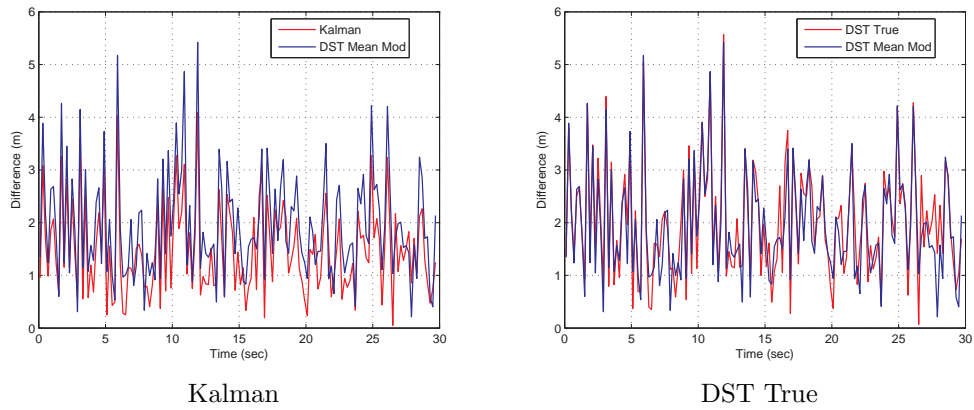
Figure 37: Run 12 - Difference Plots

through the middle. This is also indicated in the Difference Plot where DST Mean arced between t = 10 and 20. For Runs 5 and 27, the MAD and MSE values actually decreased from DST True to DST Mean despite the indications on their plots. Runs 14 and 28 showed a slight increase, but the DST Mean MSE values in Runs 1 and 11 were more than double those from the DST True. The MSE for Run 1 increased from 6.1524 to 13.0258. Table 12 shows the other values.
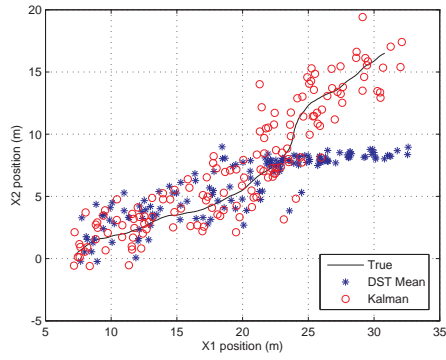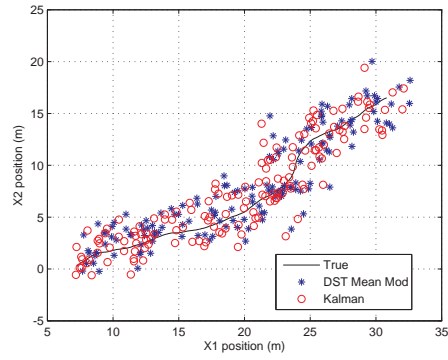
Figure 38: Run 1 - Point Plot
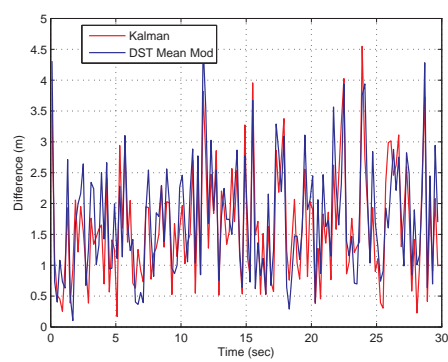
Figure 39: Run 1 - Difference Plot
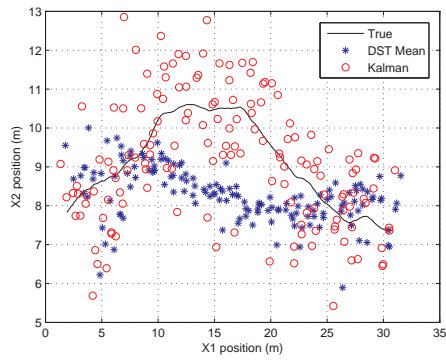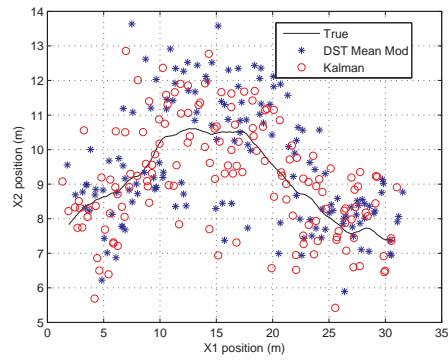
Figure 40: Run 27 - Point Plot

Before   After
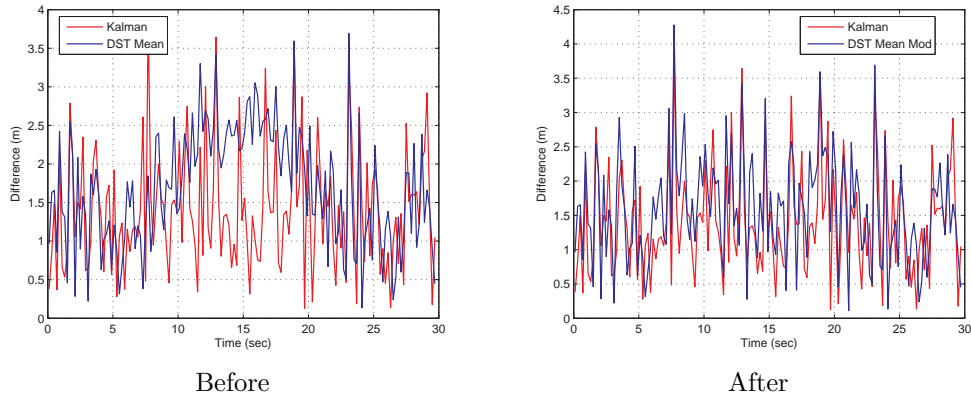
Figure 41: Run 27 - Difference Plot

The Error Plots are shown in Figures 42 and 43. All of the runs, except Run 9, had large errors for x_2, which was excepted from the Point Plots. Run 9 had large x_1 errors. Based these plots, $\alpha = 2$ for all of the runs, excluding 27 and 28. For these, $\alpha = 1$. After implementing the DST Mean Mod approach, the After Plots showed the results that we anticipated. Note these results exclude Run 9. So $\mathbf{x}_{t,\text{MEAN MOD}}$ followed the actual trajectory closer, as well as the Kalman results. Also the differences for DST Mean Mod no longer had large jumps but instead stayed level. As seen in Table 12, the MAD and the MSE for all of the runs decreased below the DST True values. For example, Run 14's MAD value decreased from 1.9378 to 1.8011 and MSE value from 4.7513 to 4.0236. Also Runs 1 and 27 also produced values closer to the Kalman than the DST True values.

Run 1   Run 5   Run 9   Run 11
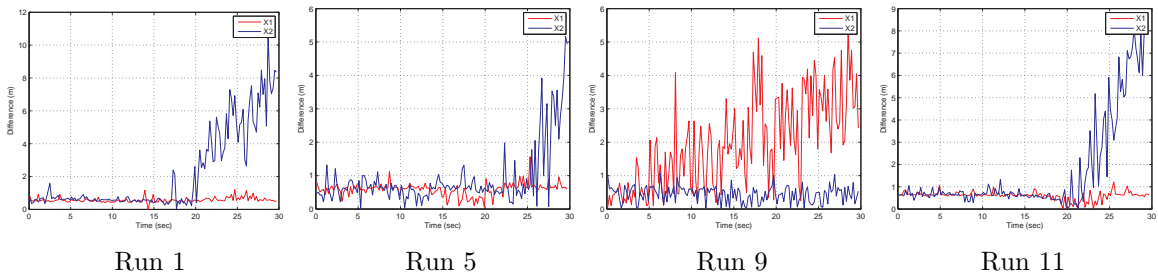
Figure 42: Case 4 - Error Plots

44

| Run 14 | Run 27 | Run 28 |
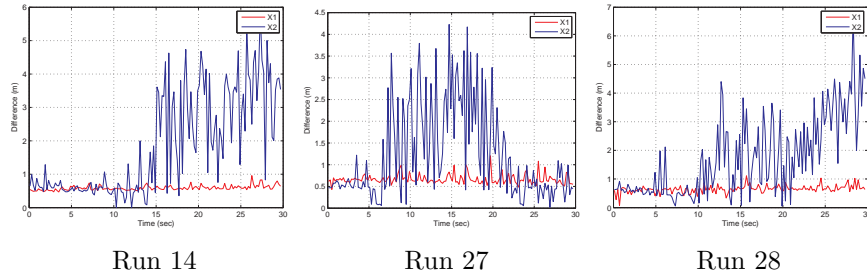
Figure 43: Case 4 - Error Plots (cont.)

Next, Run 9 was evaluated. Figures 44 and 45 show the different results. This run's points seemed to be all over the place. Both Kalman and DST Mean were widely scattered, lacking any trends. However, the differences for DST Mean showed large increases after t = 14. Kalman remained fairly level. Then unlike the other runs, DST Mean Mod did not improve Run 9. Its points were still scattered, and the differences did not decrease. Yet the DST True differences for this run were also large as seen in the Figure 45 After Difference Plot. The After Point Plots in Figure 44 shows the Kalman, the DST True, and the DST Mean Mod points. The DST True points were just as, if not more, scattered as the DST Mean Mod. The main distinction between DST Mean Mod and the others lies after $x_1 = 35$. To get better results, the probability mass function for Run 9 has to be redefined or modified again. As this run was a stand alone, this new function lies in future work. See Section 6.2.
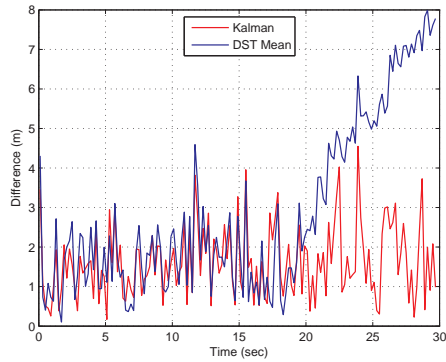

| Before | After |
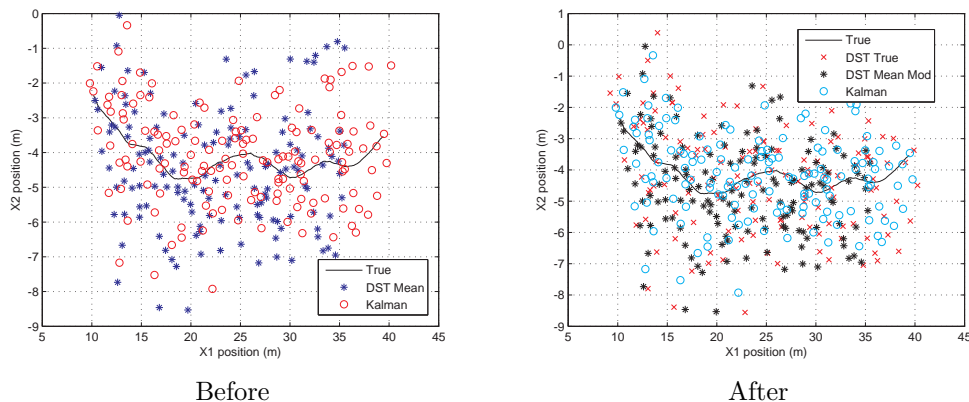
Figure 44: Run 9 - Point Plot

45

Before   After
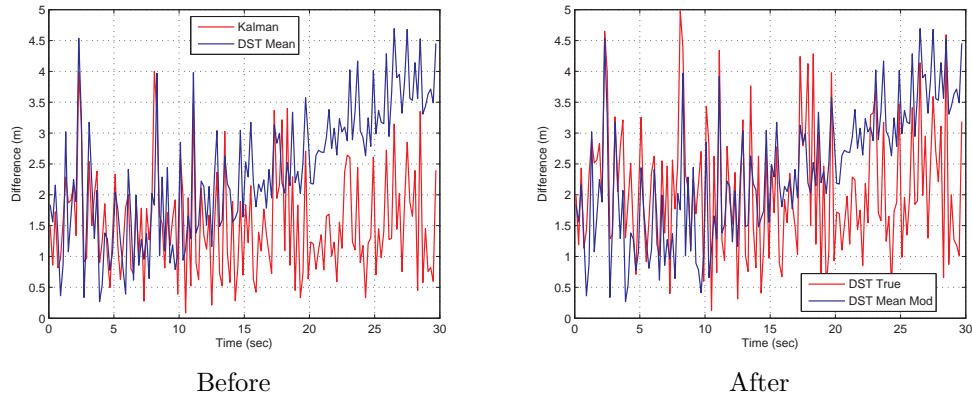
Figure 45: Run 9 - Difference Plot

The results from all of the improved runs were reflected in the positive changes in the Averaged Run. In Figure 46, there was a large group of the DST Mean points below the true path starting at t = 7 in the Before Point Plot. In the After, these points followed the true path and were very similar to the Kalman points. The Before Difference Plot in Figure 47 shows a similar trend as the problem runs' Difference Plots, particularly the major jump after t = 20. In the After Plot, the jump disappeared. The differences for Kalman and DST Mean Mod then became almost identical, and at many times t, the DST Mean Mod was smaller. Note that the scales of the Before and the After Difference Plots are not the same. Therefore from both plots, we saw significant improvement from the DST Mean Mod approach.

Before   After
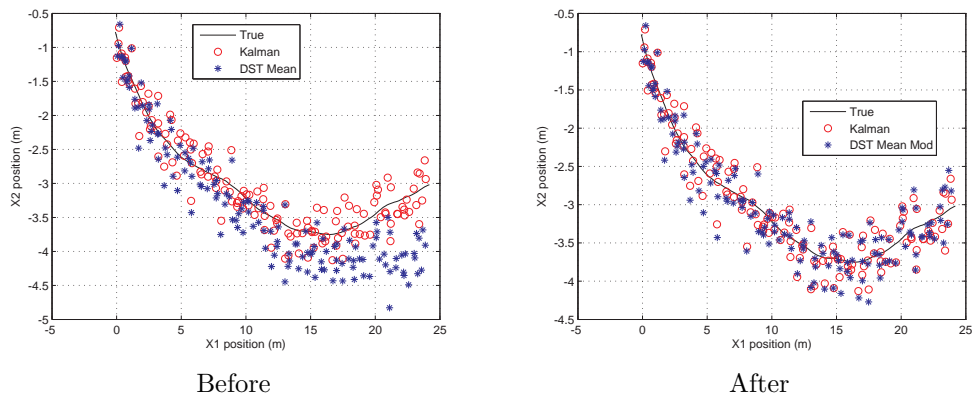
Figure 46: Averaged Run - Point Plot

Before   After
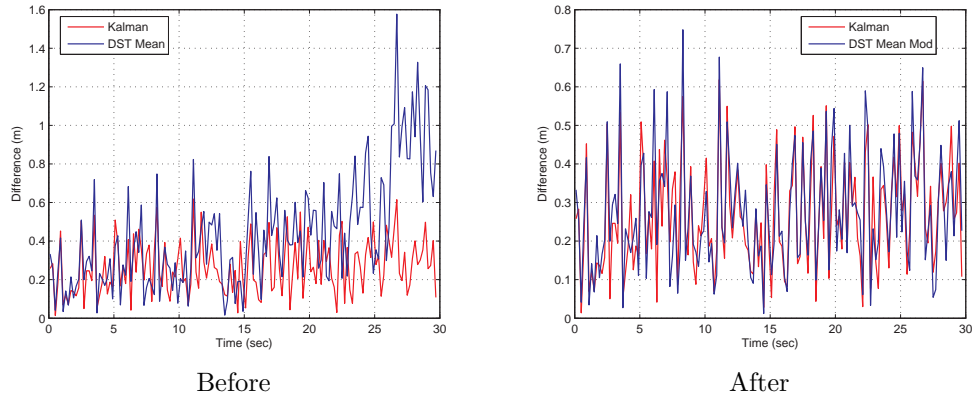
Figure 47: Averaged Run - Difference Plot

All of the MAD and the MSE values for Case 4 are listed in Tables 12 and 13. For all of the non-problematic runs, applying the DST Mean Mod approach did not change the outcome as indicated by NO CHANGE. In other words, the errors for $x_{j,t,MEAN}$ did not exceed the α threshold. For these runs, the MAD and the MSE decreased from DST True to DST Mean. For example, the MAD for Run 24 decreased from 1.8262 to 1.5541. Also in many runs, the MAD and the MSE values for the DST Mean approach were closer to the Kalman values than the DST True values.

With the improvements in each run, especially in the problem runs, the Averaged Run had excellent results. The MAD and the MSE for DST Mean Mod were 0.2757 and 0.0991, compared to the Kalman values of 0.2657 and 0.0906. Notice the large increase from DST True to DST Mean. This was due to the problematic runs; otherwise, these values would have decreased. Also similar to Case 3, all of the values were smaller than those in Case 2. The increased runs improved the results for every approach.

Table 12: Case 4-MAD/MSE Values

RUN #	MEASURE	KALMAN	DST		
			TRUE	MEAN	MEAN MOD.
1	MAD	1.6228	2.2094	2.9006	1.7601
	MSE	3.4388	6.1524	13.0258	3.9811
2	MAD	1.5166	2.0852	1.7049	NO CHANGE
	MSE	2.8601	5.2662	3.7820	NO CHANGE
3	MAD	1.4600	2.0047	1.5741	NO CHANGE
	MSE	2.6959	4.9037	3.0122	NO CHANGE
4	MAD	1.3656	1.9026	1.7074	NO CHANGE
	MSE	2.3612	4.5025	3.6389	NO CHANGE
5	MAD	1.3607	1.8875	1.8464	1.7001
	MSE	2.3674	4.4175	4.2757	3.6144
6	MAD	1.5050	2.0710	1.9223	NO CHANGE
	MSE	2.9299	5.3643	4.6380	NO CHANGE
7	MAD	1.5023	2.0448	1.7892	NO CHANGE
	MSE	2.9888	5.3266	4.2019	NO CHANGE
8	MAD	1.3531	1.8649	1.7682	NO CHANGE
	MSE	2.5728	4.6967	4.1540	NO CHANGE
9	MAD	1.5160	2.0685	2.3685	2.3633
	MSE	2.9792	5.3550	6.6978	6.6851
10	MAD	1.3826	1.9112	1.8458	NO CHANGE
	MSE	2.4010	4.4577	4.2303	NO CHANGE
11	MAD	1.3279	1.8290	2.4867	1.6534
	MSE	2.3409	4.2467	9.8899	3.4182
12	MAD	1.4738	2.0082	1.9470	NO CHANGE
	MSE	2.8660	5.1413	4.8222	NO CHANGE
13	MAD	1.4401	1.9754	1.8491	NO CHANGE
	MSE	2.7493	4.9562	4.2551	NO CHANGE
14	MAD	1.4151	1.9378	2.4033	1.8011
	MSE	2.6357	4.7513	7.0219	4.0236
15	MAD	1.4579	1.9980	1.8255	NO CHANGE
	MSE	2.7126	4.8629	4.1388	NO CHANGE
16	MAD	1.4736	2.0220	1.9453	NO CHANGE
	MSE	2.8466	5.1400	4.8573	NO CHANGE
17	MAD	1.4806	2.0094	1.9190	NO CHANGE
	MSE	2.9759	5.2083	4.6159	NO CHANGE
18	MAD	1.4047	1.9263	1.6329	NO CHANGE
	MSE	2.6431	4.7643	3.4820	NO CHANGE

RUN #	MEASURE	KALMAN	DST TRUE	DST MEAN	DST MEAN MOD.
19	MAD	1.4439	2.0012	1.5451	NO CHANGE
	MSE	2.8441	5.2250	3.1244	NO CHANGE
20	MAD	1.3844	1.9222	1.7764	NO CHANGE
	MSE	2.3393	4.3956	3.8865	NO CHANGE
21	MAD	1.3358	1.8332	1.7282	NO CHANGE
	MSE	2.3992	4.3677	3.8972	NO CHANGE
22	MAD	1.4297	1.9464	1.7353	NO CHANGE
	MSE	2.7039	4.8305	3.7407	NO CHANGE
23	MAD	1.4726	2.0103	1.6019	NO CHANGE
	MSE	2.9641	5.2810	3.5446	NO CHANGE
24	MAD	1.3367	1.8264	1.5541	NO CHANGE
	MSE	2.5201	4.4855	3.2814	NO CHANGE
25	MAD	1.5298	2.0777	1.9288	NO CHANGE
	MSE	3.0534	5.4237	4.6373	NO CHANGE
26	MAD	1.4145	1.9509	1.6970	NO CHANGE
	MSE	2.5826	4.7893	3.6524	NO CHANGE
27	MAD	1.3935	1.9092	1.6916	1.5920
	MSE	2.5283	4.5735	3.4400	3.1492
28	MAD	1.4958	2.0542	2.5149	1.7151
	MSE	2.8245	5.1694	7.6955	3.6748
29	MAD	1.5555	2.1291	1.6577	NO CHANGE
	MSE	3.1898	5.7224	3.6021	NO CHANGE
30	MAD	1.4025	1.9350	1.6739	NO CHANGE
	MSE	2.6040	4.7734	3.6926	NO CHANGE
AVG	MAD	0.2657	0.3560	0.4349	0.2757
	MSE	0.0906	0.1626	0.2766	0.0991

3.5.5 Case 5. For Case 5, the errors, σ_i, for Sensor 1 and Sensor 2 were set to 2 and 8, respectively. Then thirty runs were completed. Figure 48 shows the position measurements, $\mathbf{x}_{t,i}$, for a sample of these runs. Because Sensor 2 had a much larger error, its output was more spread out and clearly further from the true position, $\mathbf{x}_{t,ACTUAL}$. Figure 49 shows the measurements for the Averaged Run.

For this case, Run 30 was the only problematic run. We again applied the DST Mean Mod approach, in addition to the other three, and α is set to 2. Also Runs 2, 5, 9, 15, 20, 21, 25, 26, 27, and 28 (one third of the runs) remained unmodified since
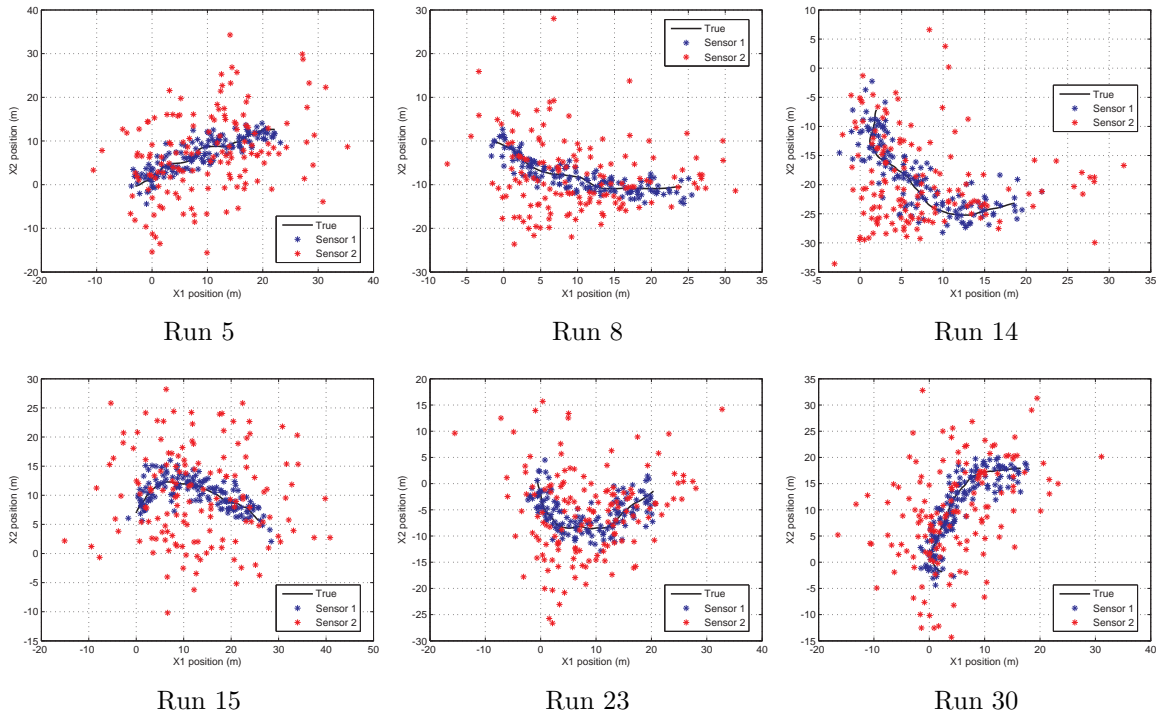
Figure 48: Case 5 Sensor Measurements
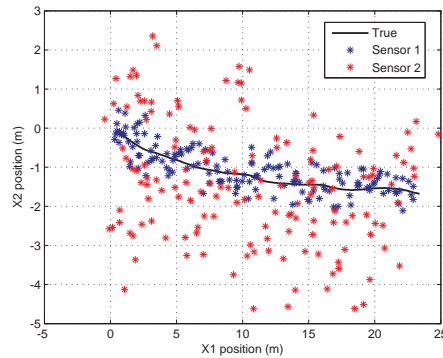
Figure 49: Case 5 Averaged Sensor Measurements

they had better results from DST Mean. Recall the final results were still denoted $x_{j,t,MEAN\ MOD}$ for the unmodified runs. Run 30 is examined after the Difference Plots.

Figure 50 shows the Point Plots for Runs 24 and 27. While the DST Mean Mod points in Run 24 followed the aircraft's trajectory, they were fairly wide spread. Notice the more points tend to be above the True line than below. However, the Kalman and the DST True points showed the same patterns. Clearly Run 27 had

better results than Run 24. The DST Mean Mod points followed very closely along the true trajectory. Most of these points were an improvement to the Kalman points. However, notice the points at $x_2 \in [0, 5]$. The DST Mean Mod points here had a wider spread, but the Kalman and the DST True did, as well. The other runs had similar results to these two.

Run 24   Run 27
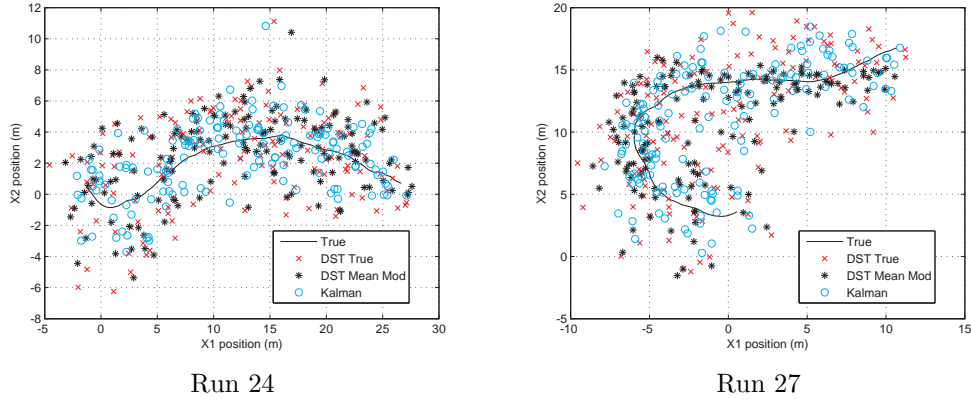
Figure 50: Case 5 Point Plots

In Figures 51 and 52, the Difference Plots show the same trends as the previous cases. In Run 24 the majority of the Kalman differences were smaller than DST Mean Mod, and the DST True differences were greater. All three approaches had spikes at the same time t. Specifically at t = 21, there were large spikes. Here DST Mean Mod was less than the other two. Also, as always there were other times t where DST Mean Mod had better results than Kalman. In Run 27, the differences were much smaller as expected from the Point Plot results. For $t > 15$, most differences for DST Mean Mod were smaller than Kalman. Against DST True, DST Mean Mod showed major improvement. Notice the large spikes at $t \in [0, 8]$, these correspond to points at $x_2 \in [0, 5]$ on the Point Plots. Overall, these same general trends existed for all runs. However, note that the differences for each run were larger than those in the previous cases. This was a result of error associated with Sensor 2.

As the Before Plots in Figures 53 and 54 show, Run 30 did not have good results from DST Mean. Similar to some previous cases, $\mathbf{x}_{t,\text{MEAN}}$ leveled out around $x_2 = 15$,

Kalman   DST True
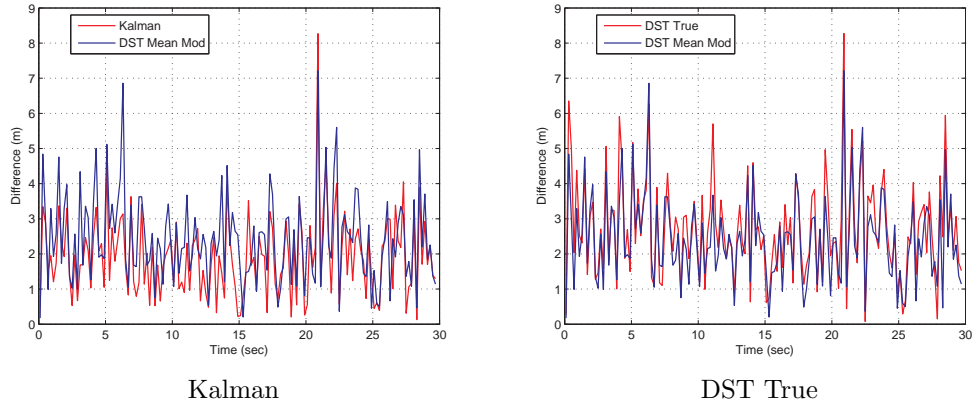
Figure 51: Run 24 - Difference Plots

Kalman   DST True
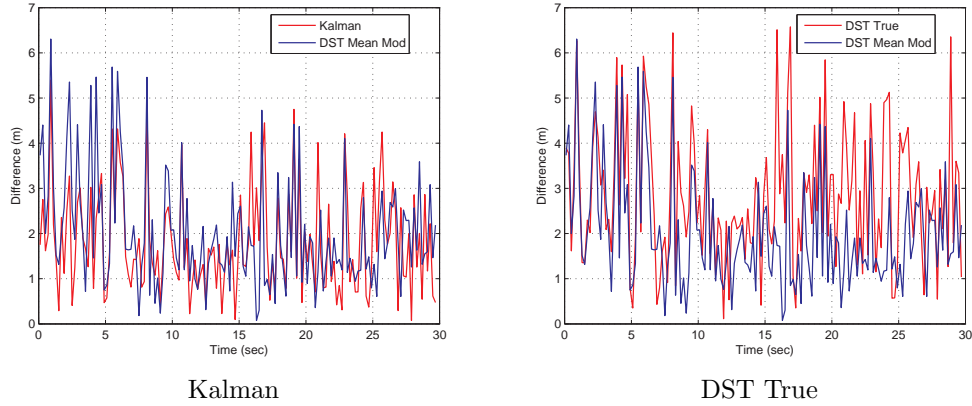
Figure 52: Run 27 - Difference Plots

and the differences for DST Mean increased significantly after t = 22. However, the MAD and the MSE values actually slightly decreased from 2.7380 and 9.4291 for DST True to 2.7018 and 9.2491 for DST Mean, respectively.

In the Error Plot in Figure 55, both x_1 and x_2 had large errors. From this plot, α was set equal to 2. Then $m^*_{j,t,i,MEAN\ MOD}$ was calculated. The improvement is clear in the After Plots. So $\mathbf{x}_{t,MEAN\ MOD}$ followed closer to the true trajectory, and the differences decreased for $t \geq 22$. The MAD and the MSE also decreased further to 2.4719 and 7.8613.

Other than the unmodified runs, the DST Mean Mod approach improved the results for each run. The Averaged Run had subtle changes based on these improve-

Before   After
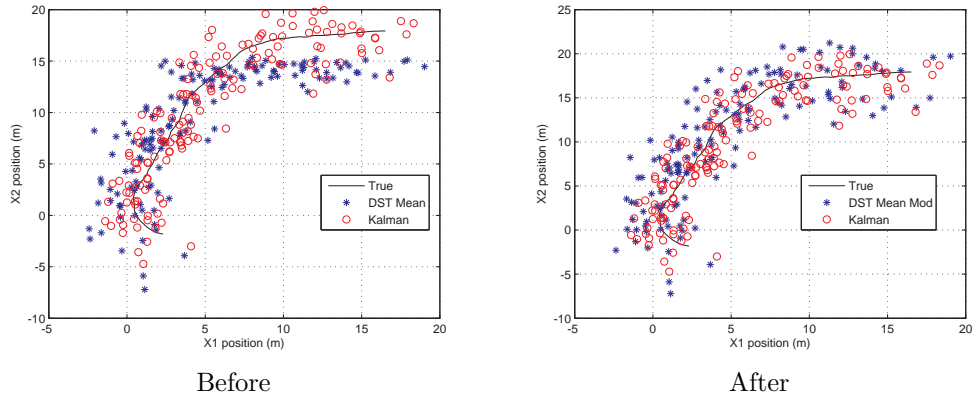
Figure 53: Run 30 - Point Plot
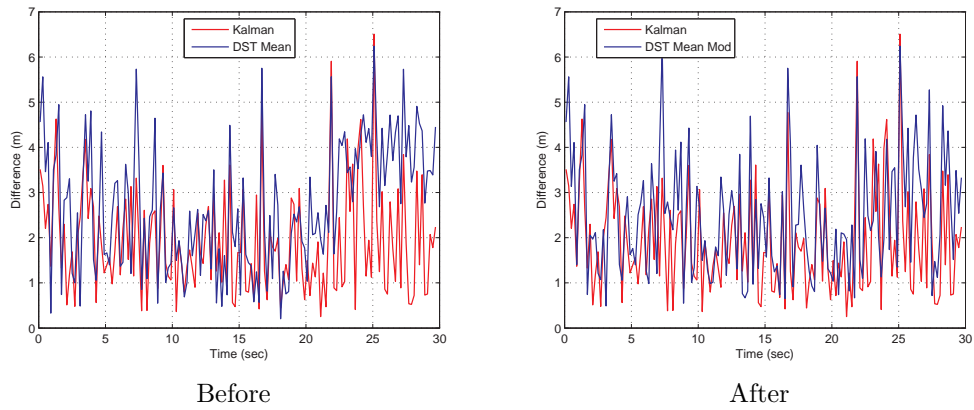
Before   After

Figure 54: Run 30 - Difference Plot
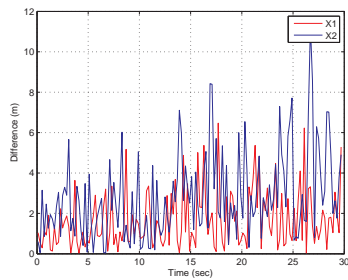
Figure 55: Case 5 Run 30 - Error Plot

ments. In the Figure 56 After Plot, the combined data for DST Mean Mod formed a tighter grouping around the True line. The large scatter of the points in the Before Plot below the True line disappeared in the After Plot. In Figure 57, the differences decreased across the whole range of times. Note that the scale is not the same for

53

both plots. The large spikes at t = 1 and t = 21 decreased from 2 to less than 1.5. The grouping at $t \geq 22$ decreased to below 1.
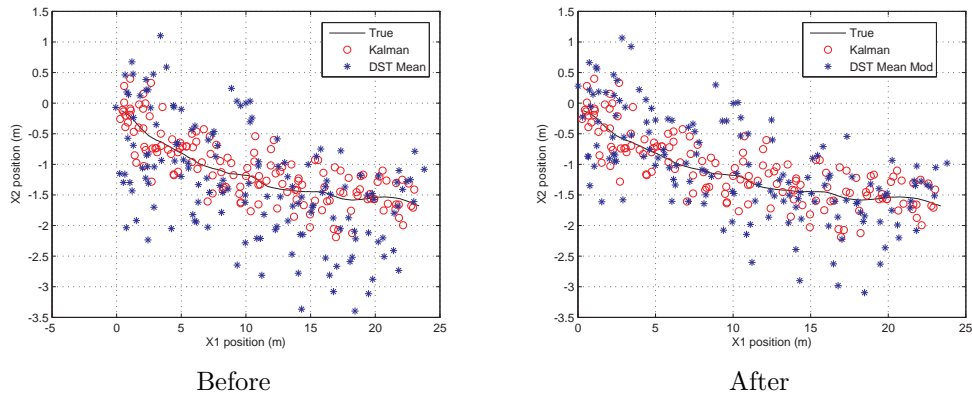
Figure 56: Averaged Run - Point Plot
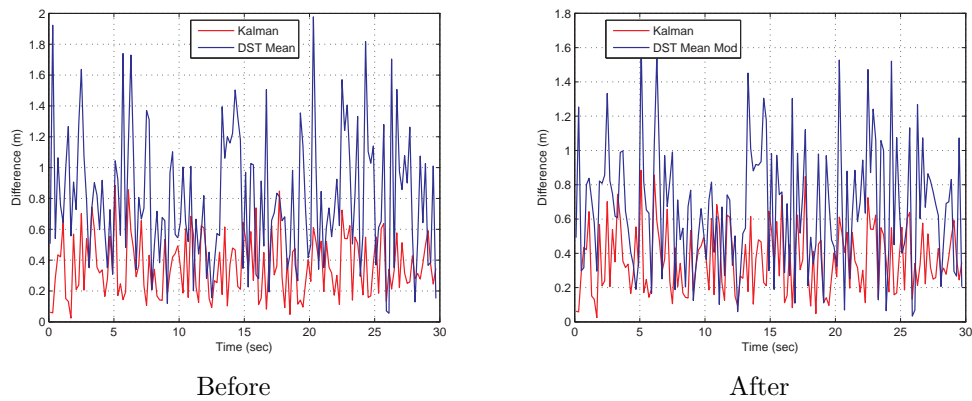
Figure 57: Averaged Run - Difference Plot

Tables 14 and 15 list the MAD and the MSE values. NA indicates the unmodified runs. All of the MAD and the MSE values decreased from the DST True to DST Mean or DST Mean Mod (depending on the run). Also in some runs, the MAD and MSE values for the final DST method were closer to the Kalman values than the DST True value. For example in Run 6, the MSE was 10.0780 for DST True and 7.7938 for DST Mean Mod. The Kalman in this run was 6.0987, clearly closer to DST Mean Mod than DST True was.

54

Table 14: Case 5-MAD/MSE Values

RUN #	MEASURE	KALMAN	DST		
			TRUE	MEAN	MEAN MOD.
1	MAD	1.7351	2.5784	2.1669	2.0787
	MSE	4.1094	8.5675	6.3376	5.7665
2	MAD	1.6849	2.4066	2.1532	NA
	MSE	3.7559	7.4342	6.1327	NA
3	MAD	1.9175	2.6007	2.4064	2.2822
	MSE	4.7888	8.5240	7.4171	6.5956
4	MAD	2.2154	3.0159	2.8029	2.5231
	MSE	6.2660	11.2969	10.2475	8.4342
5	MAD	1.8306	2.7605	2.4238	NA
	MSE	4.3692	9.7344	7.7059	NA
6	MAD	2.1734	2.8131	2.5395	2.4487
	MSE	6.0987	10.0780	8.2156	7.7938
7	MAD	2.0813	2.6691	2.3284	2.2385
	MSE	5.4348	8.8441	6.6799	6.2949
8	MAD	1.9007	2.5840	2.5167	2.3474
	MSE	4.5889	8.2697	7.8933	7.2370
9	MAD	1.9221	2.8283	2.1954	NA
	MSE	4.8221	9.7675	5.9870	NA
10	MAD	1.9325	2.7169	2.5007	2.3125
	MSE	4.9370	8.8082	7.6496	6.7334
11	MAD	2.0141	2.7417	2.5351	2.3656
	MSE	4.9776	8.9757	7.7724	6.8048
12	MAD	1.9275	2.6878	2.4963	2.2760
	MSE	4.5439	8.5838	7.3707	6.1420
13	MAD	2.1016	2.6452	2.2968	2.2156
	MSE	5.7061	8.9497	7.0753	6.4442
14	MAD	2.3410	2.7130	2.5124	2.4405
	MSE	7.2519	9.6424	8.3120	8.0199
15	MAD	1.9898	2.9551	2.4684	NA
	MSE	5.3188	10.7198	7.8199	NA
16	MAD	2.0869	2.6598	2.3040	2.3040
	MSE	5.4452	8.8718	6.9133	6.7895
17	MAD	1.9232	2.7965	2.6094	2.4943
	MSE	4.8826	9.6046	8.6018	7.8762
18	MAD	1.9518	2.8060	2.3915	2.3786
	MSE	5.0840	9.8231	7.7111	7.3762
19	MAD	1.8740	2.6918	2.5747	2.2689
	MSE	4.3211	8.8655	8.4925	6.4818

Table 15: Case 5-MAD/MSE Values (cont.)

| RUN # | MEASURE | KALMAN | DST | | |
			TRUE	MEAN	MEAN MOD.
20	MAD	2.0292	2.7770	2.2586	NA
	MSE	5.4295	9.7369	6.8166	NA
21	MAD	1.8833	2.8206	2.1294	NA
	MSE	4.6096	9.6816	5.7530	NA
22	MAD	2.0010	2.7784	2.4465	2.2933
	MSE	5.2506	9.6116	7.8275	6.8441
23	MAD	2.0890	2.7956	2.5864	2.4086
	MSE	5.7387	9.9960	8.8095	7.8017
24	MAD	1.9097	2.7003	2.5631	2.4203
	MSE	4.9370	9.2593	8.5248	7.4622
25	MAD	2.2283	2.8545	2.3939	NA
	MSE	6.3954	10.2175	7.3635	NA
26	MAD	1.7730	2.5730	2.2850	NA
	MSE	4.1921	8.4888	6.7740	NA
27	MAD	1.8053	2.8491	2.0255	NA
	MSE	4.5272	10.3421	5.7256	NA
28	MAD	1.7505	2.6124	2.4100	NA
	MSE	4.1766	8.6498	7.4647	NA
29	MAD	2.0123	2.6363	2.4271	2.2413
	MSE	5.5099	8.8515	7.8092	6.5385
30	MAD	1.9103	2.7380	2.7018	2.4719
	MSE	4.9898	9.4291	9.2491	7.8613
AVG	MAD	0.3622	0.4883	0.7958	0.6661
	MSE	0.1683	0.3018	0.8045	0.5712

Unlike the other cases, the Averaged Run did not have as much improvement as expected. While the MAD and the MSE decreased from DST Mean to DST Mean Mod, the values for DST Mean Mod were not less than the DST True values. The MSE values for DST True, DST Mean, and DST Mean Mod were 0.3018, 0.8045, and 0.5712. The MAD values were 0.4883, 0.7958, and 0.6661. Figure 58 shows the Point Plot with DST True. Note the DST Mean Mod points for $x_2 \in [-2, -3.1]$ that are further from the True line than the DST True points. Also for $x_1 \in [0, 13]$, there are groupings of DST Mean Mod points above the True line that again are further than the DST True. These points are why the MAD and the MSE were larger than expected. However, it's unclear why the DST Mean Mod points turned out like they

did. In the individual runs, all of the plots showed improvements, and for both DST Mean and DST Mean Mod, the MAD and the MSE values were smaller than the DST True. Also the Averaged Runs in the other 4 cases had improvements from DST True. Thus, it is unlikely there was a problem with the DST Mean Mod approach, but rather this was an isolated occurrence.
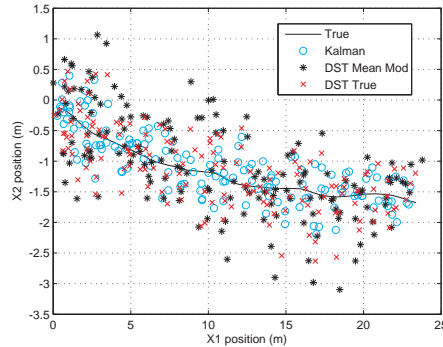
Figure 58: Averaged Run - Point Plot

3.6   Summary

Recall the scenario described in Section 3.2. We had two sensors tracking a single aircraft across a field. Using MATLAB code, we generated the sensor data for multiple runs with varying errors. Taking this data, we applied two different fusion methods: the Kalman filter and the DST. From the Dempster-Shafer Method, three approaches were developed, each having slightly different probability mass assignments. DST True relied on knowing the true position of the aircraft. DST Mean and DST Mean Mod used only the sensor data from each run. As the name indicates, DST Mean Mod is a modified approach to DST Mean. It was applied when the error from (17) exceed a set α value. With these three DST approaches and the Kalman filter approach, we combined the sensor data to obtain better positioning results for the aircraft that we were tracking.

With the four combined results in each case, we had three comparison techniques to determine how each approach did. Section 3.4 outlined these techniques and what

we expected from each. For the five cases, the Point Plots, Difference Plots, and the MAD and MSE values showed the results we were expecting for the most part. The exceptions were Case 4 Run 9 and Case 5 Averaged Run. Run 9 had poor results from both DST Mean and DST Mean Mod. In the Case 5 Averaged Run, the MAD and the MSE values for DST Mean Mod were larger than those for DST True.

In all the cases except Case 1, problematic runs were present. In these runs, the combined points from DST Mean tended to level off at a particular point, producing poor positioning results. The DST Mean Mod approach was applied to fix these runs. Again the exception was Case 4 Run 9. In addition to the problem runs, this approach also improved several other runs.

Notice Cases 1 and 3 and Cases 2 and 4 had the same sensor errors. However, one case had a different number of runs than the other. These cases were run to show the improvement in the Averaged Runs as the number of runs increased. Comparing the Point Plots, Cases 3 and 4 showed the results in a tighter grouping along the true trajectories. Also in the Difference Plots, the values were smaller. In Case 2, most of the differences were between 0 and 1, but in Case 4, they were between 0 and 0.6. Finally, the MAD and the MSE values decreased for all of the approaches. In Run 1, the DST Mean values were 0.8205 and 0.8653. In Run 3, these values dropped to 0.3877 and 0.2010. Thus, between the three comparisons, the Averaged Run improved with more runs.

In all of the cases, the Dempster-Shafer Method produced good results. Both the DST Mean and the DST Mean Mod approaches then showed significant improvement over the DST True. While the Kalman filter was more accurate, the Dempster-Shafer Method had very comparable results. Given that the sensor noise was actually from a normal distribution, this was somewhat anticipated. However, in many situations, the noise is not necessarily or known to be Gaussian, rendering the Kalman filter unusable. Therefore without making any assumptions about the error, we were able to accurately combine the sensor data using the DST.

IV. Local Navigation

4.1 Introduction

In this chapter, we applied the Dempster-Shafer Method to fuse data from a multi-sensor unit for precise local navigation. For navigation it is imperative to have extremely accurate position measurements at any given time. However, no sensor is perfect. Each has limitations, but each may have advantages too. By fusing the information from each sensor, we can reduce the uncertainty and increase the accuracy [1].

This multi-sensor unit is comprised of a Global Positioning System (GPS) sensor, a Tactical Grade Inertial Measurement Unit (IMU), and an optical imaging camera. The GPS provides very precise position data but at larger time intervals than the other sensors mentioned. For this GPS sensor, the time intervals were 0.10 sec. Also, because the GPS is dependent on satellite updates, there are often outages. The IMU is a strictly internal component with no dependence on outside systems. It provides measurements more frequently with a time interval equal to 0.01 sec. The IMU does not output the actual position. It consists of an accelerometer and a gyroscope which provide the specific force and the angular rate at a specific time [43]. Finally, the camera takes a series of still images. In each image, it measures the directions of different features [45]. However, multiple cameras and significantly more preprocessing are required. Converting all of these sensors' data into a common measurement, we can combine them and more accurately determine location.

Because the optical camera outputs measurements in relation to a feature, it only provides a two-dimensional measurement. As a result, it is very difficult to navigate with. Techniques do exist to determine distances; however, a second camera is needed [54]. For this reason, the camera was not used for sensor fusion.

The sensor data used in this chapter was provided by Major Fisher and the AFIT ANT Center. Each sensor was fixed to the body frame of a motor cart. The start location of the body frame was 0.694323082282726 rad, -1.46750437073683 rad, and 276.9 m in latitude, longitude, and altitude. The start time for data collection

was 417702.055286 GPS week seconds. The cart was then driven in a U-shaped path. Along this path, the cart entered and exited a building where a GPS outage occurred. Figure 59 shows a map of the path taken. The data collection lasted for 4.7691 minutes. The variances associated with each measurement were estimated and provided with the rest of the sensor data.

Building Interior   **Building Exterior**
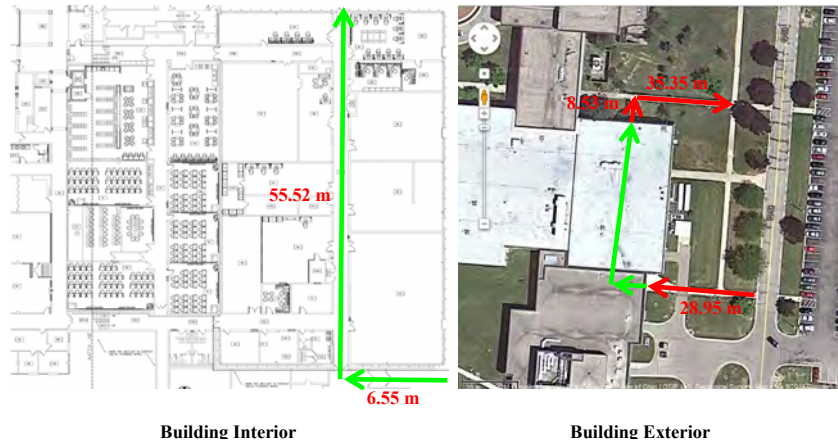
Figure 59: Cart Path

Note that each measurement is the true value plus some measurement noise, or, for the IMU, noise and scale factor error. According to the Interface Control Document (ICD) for each sensor, the noise errors, as well as other IMU errors, are modeled as Gaussian distribution. Yet, as noted in the GPS ICD, the actual measurements do not always fit the Gaussian model [44]. This is where it is advantageous to use the Dempster-Shafer Method. Specifically, we do not have to assume the prior distributions.

4.2 Sensors

In this section we describe the GPS and the IMU sensors in more detail, including what each outputs and the estimated variances.

The GPS sensor outputs three position measurements in World Geodetic System (WGS)-84 ellipsoidal coordinates: geodetic latitude, longitude, and altitude. The measured latitude and longitude are in radians, and the measured altitude is in meters

above the WGS-84 ellipsoid [44]. WGS-84 is the latest version of the World Geodetic System. It is a standard coordinate frame for Earth and the reference coordinate system for GPS [56]. The time between measurements, Δt_{GPS}, was 0.10 sec. A total of 1545 measurements were outputted, and the first measurement was at 417702.1 GPS week seconds.

Two outages occurred for this data set. The first outage lasted for 130.9 sec as the cart went through the building. The other was only for 1 sec. During these outages, the navigation position was solely based on the IMU data.

The position measurements for the GPS are combinations of the true positions and noise from the sensor. The error standard deviation for latitude, longitude, and altitude were estimated to be $\frac{4}{R}$ rad, $\frac{4}{R*cos(lat)}$ rad, and 8 m, respectively. The approximate Earth's radius, R, used for this data was 6377936 m [44]. Notice the variance for longitude is dependent on latitude and is different at each measurement. However, because change in latitude was very small, the changes in the variance were also minuscule. These variances for latitude, longitude, and altitude are denoted σ_{GPS1}^2, $\sigma_{GPS2,n}^2$, and σ_{GPS3}^2, where n is the measurement number.

The IMU outputs the integrated specific force, ΔV, and the integrated angular rate, $\Delta \theta$, over a specific time interval in the three orthogonal axes. These measurements were all taken relative to the sensor frame, which was connected to the cart body frame [46]. ΔV is measured in meters per second and $\Delta \theta$ in radians [43]. The time between measurements, Δt_{IMU}, was approximately 0.01 sec for a total of 28614 measurements. Its first measurement was taken at 417702.065286 GPS week seconds.

The IMU measurements are modeled as the following:

$$Measured = True * (1 + SF) + b + w$$

where SF is the scale factor error, b is the time-correlated bias, and w is the noise [43]. The estimated standard deviations for each were provided with the data. So the sample standard deviations, σ, for the factor error, bias, and noise were approximately

$0.0003, 9.800 * 10^{-7}$, and $9.025 * 10^{-7}$, respectively. Then the combined variance was estimated by

$$\sigma^2 = (True * \sigma_{SF})^2 + \sigma_b^2 + \sigma_w^2. \tag{19}$$

Since the True values were unknown, the Measured values were used instead.

With Δt_{IMU}, the change in distance can be determined from the IMU. Because it does not provide the actual position on the sensor, a starting location must be known. Combining the two gives the location of the vehicle according to the IMU.

4.3 Approach

With a better understanding of the two sensors, we applied the Dempster-Shafer Method to combine the two location measurements. For this data, we considered two sets of results. The first was real-time results. As the cart was moving, we determined its location based on what the sensors were immediately reporting. The second results were calculated after all of the data was collected. Knowing the GPS had a large outage, we filled in the missing GPS data. These results would be desirable if a repeat of this route was necessary, to further refine the calculations, or even to modify the sensors. However, before we could actually use our fusion method, several more steps were needed.

First, some transformations were required. Recall the GPS data was expressed in WGS-84 ellipsoidal coordinates, and the IMU data was in the sensor reference frame. Because the GPS and the IMU outputs were in difference reference frames, we needed to convert the IMU measurements to the ellipsoidal coordinates. The transformed data was provided by Dr. John Raquet of the AFIT ANT Center. The locations are denoted $loc_{n,i} = (lat_{n,i}, lon_{n,i}, alt_{n,i})$, where n is the measurement number, and i is the index denoting the sensor, GPS or IMU.

The IMU variance from (19) also had to be converted. The new variances are denoted $\sigma_{IMU1,n}^2$, $\sigma_{IMU2,n}^2$, and $\sigma_{IMU3,n}^2$, which correspond to the $lat_{n,IMU}, lon_{n,IMU}$, and $alt_{n,IMU}$, respectively. Comparing the variances for latitude and longitude, the

IMU had significantly larger values than the GPS. However, for altitude the GPS had a larger variance. This had an impact on the probability masses.

Note that the outputs of the sensors can be referenced by both their measurement number and their measured time. Starting near 417702 GPS week seconds, the IMU measured times were evaluated to one millionth of a second, and the GPS measured times were increased to one tenth of a second. Thus, it was simpler to reference the measurement numbers. However, the sensors' measurement numbers did not occur at the same measured time. Recall the IMU had 28,614 measurements, and the GPS had 1,545. For example, the measured time for $loc_{1,GPS}$ is approximately equal to $loc_{4,IMU}$. Therefore, the n is directly related to the i.

When GPS outputs were not available, the cart location was determined solely by the IMU. When both were known, the location measurements were combined via the Dempster-Shafer Method for a more precise location. These measurements are denoted $loc_{n,DST}$. So at the 1,545 GPS outputs, this method was applied. Then for the remaining 27,069 measurements, $loc_{n,DST}$ is equal $loc_{n,IMU}$. So the n in $loc_{n,DST}$ is the same n as in $loc_{n,IMU}$.

Next, to combine the GPS and the IMU data, common measured times were required. The first measurement for the GPS, $loc_{1,GPS}$, was taken at 417702.1 GPS week seconds. The remaining followed at 0.1 sec intervals. The first measurement for the IMU, $loc_{1,IMU}$, was at 417702.065286 GPS week seconds. The Δt_{IMU} is closely approximated by 0.010000000009313. As such, none of the measured times between the two sensors occurred at the same instance. To fix this problem, the IMU times were rounded up to the nearest $\frac{1}{100}th$ of a second. This created a common measured time which occurred approximately every 10 IMU measurements starting at $loc_{4,IMU}$.

Recall the IMU outputs the integrated specific force, ΔV, so a starting location must be known. The first position of the IMU in ellipsoidal coordinates was $loc_{1,IMU} =$(0.6943230822827 rad, -1.4675043707373 rad, 276.9000005569446 m). Then

the location determined by the IMU sensor was

$$loc_{n,IMU} = loc_{n-1,IMU} + \Delta V_n * \Delta t = loc_{n-1,IMU} + \Delta loc_{n,IMU}. \tag{20}$$

Figure 60 shows the position measurements for the GPS and IMU in longitude and latitude. This figure should look similar to that in Figure 59. Note the large gap in the latitude where no GPS readings occurred. According to the IMU, instead of making a 90° turn, the cart only turned approximately 45°. Thus, the IMU measurements did not agree with the GPS measurements as the connection was reacquired. Again the IMU is dependent on the previous position, $loc_{n-1,IMU}$. If the previous is off, the rest will be, too.
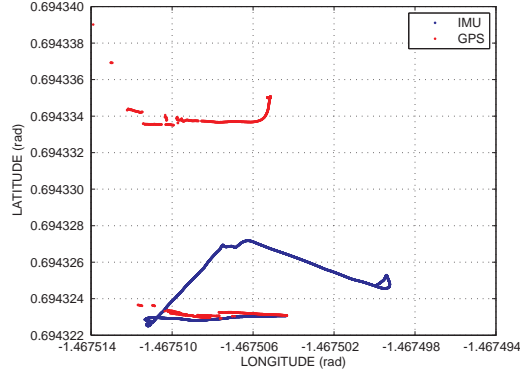
Figure 60: GPS & IMU Measurements

To fix this problem, the IMU position was updated at each combined location, $loc_{n,DST}$. The $loc_{n-1,IMU}$ in (20) was set equal to $loc_{n,DST}$. For example, $loc_{24,IMU}$ and $loc_{3,GPS}$ had the same measured time of 417702.3 GPS week seconds. So they were combined to get $loc_{24,DST}$. Then

$$loc_{25,IMU} = loc_{24,IMU} + \Delta loc_{25,IMU} = loc_{24,DST} + \Delta loc_{25,IMU}. \tag{21}$$

This provided more accurate locations for the IMU when fused with the GPS and when the GPS was not available. However, the original IMU locations were still used in some of the calculations. They are denoted $loc_{n,IMUb}$.

Knowing the cart entered and exited the building, we determined when the GPS receiver's connection began to fade, when the signal was lost, and when the connection was reacquired. The signal was completely lost from 417782.8 to 417913.7 seconds since there were no GPS outputs. These times correspond to the IMU n at 8075 and 21162. However, where a weak connection existed was determined from Figures 61 - 63. The probability masses were modified at these points for more accurate results.

In these figures, only measurements where both GPS and IMU were available were plotted. This IMU value shown is the original value, $loc_{n,IMUb}$, not the updated one. The top plots show the location measurements before the cart entered the building, and the bottom plots show after the cart exited. Note that the side axes on the two plots are not necessarily the same values. In all of the bottom plots, there is a gap between 417938 and 417939 seconds. This corresponds to the second GPS outage.

In Figure 61, we see that $lat_{n,GPS}$ did not remain continuous for the first 80 seconds. The GPS measurements slightly increased with time and then jumped down close to $lat_{n,IMUb}$ before increasing again. Around t = 417780, $lat_{n,GPS}$ had a large jump before the signal was lost. Thus, we determined that a weak signal existed if the difference between the GPS and the IMU was greater than 10^{-7} radians.

For the last 80 seconds, the first several points jumped around as the GPS signal was reacquired. After less than a second, though, $lat_{n,GPS}$ settled. There were some slight fluctuations between t = 417924 and 417934. However, $lat_{n,GPS}$ leveled out again. Thus, only the first five locations were determined to have a weak signal.

A similar pattern exists for the longitude, shown in Figure 62. At the same times as $lat_{n,GPS}$, $lon_{n,GPS}$ had jumps in the first 80 seconds. Then the values slowly decreased. Again at the same time t, $lon_{n,GPS}$ had a large jump before the signal was lost. Thus, a weak signal existed if the difference between the GPS and the IMU was greater than 10^{-7} radians.
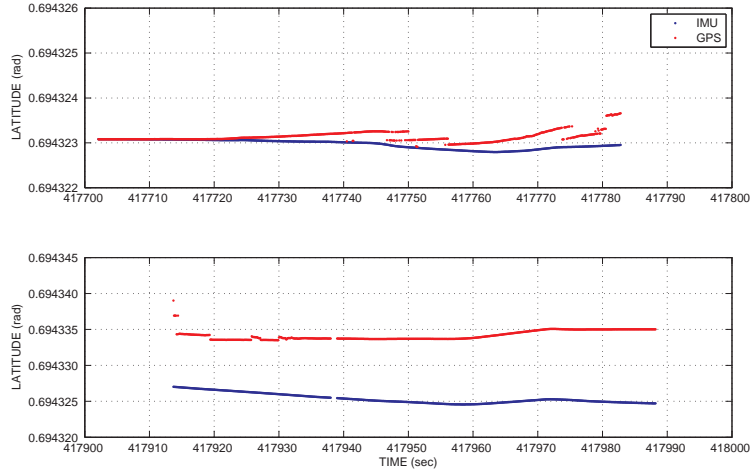
Figure 61:   GPS & IMU Latitude

For the last 80 seconds, the first several points jumped around as the GPS signal was reacquired. Less than a second later $lon_{n,GPS}$ settled. Thus, these first five locations were determined to have a weak signal.

Figure 62:   GPS & IMU Longitude

The altitude from the GPS output was quite different than the other two locations, as seen in Figure 63. The IMU and the GPS remained similar until t = 417750. After which, $alt_{n,GPS}$ began to consistently jump around. So the signal was weak if the difference between the GPS and the IMU was greater than 0.2 meters.
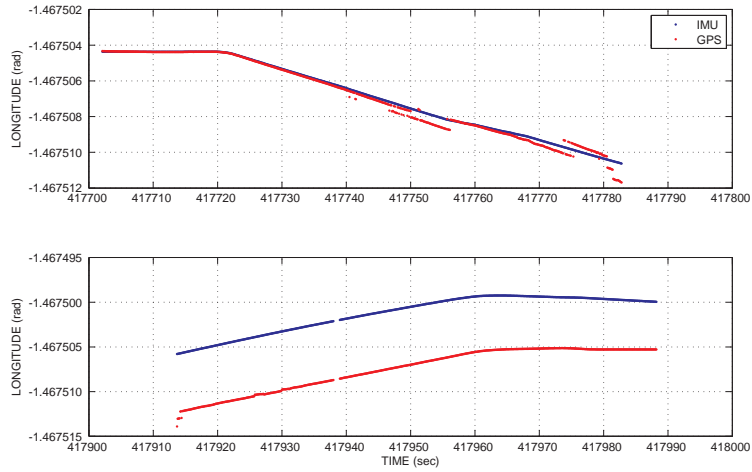
66

If the difference was greater than 0.8, $alt_{n,GPS}$ was determined unreliable, and, thus, $alt_{n,DST}$ was set by the IMU only.

For the last 80 seconds, there were many fluctuations and jumps until $alt_{n,GPS}$ settled around t = 417935. It was determined that if the difference between $alt_{n,GPS}$ and $alt_{n,IMUb}$ was more than 2.5 meters, then there was a weak signal with the GPS.
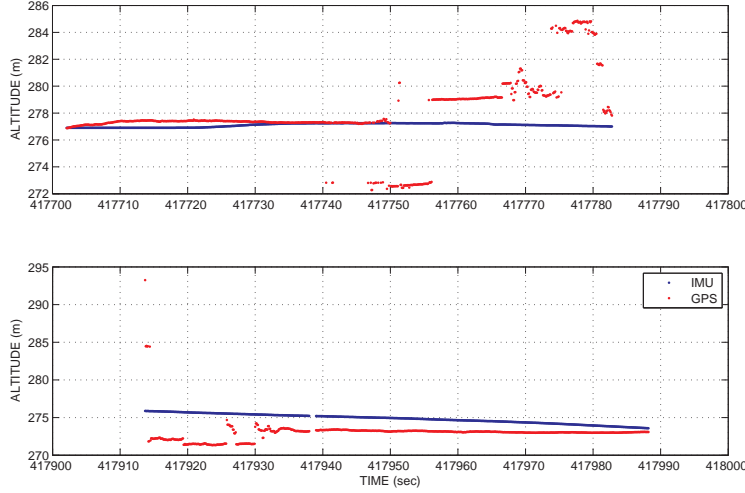
Figure 63: GPS & IMU Altitude

For the post-collection results, we interpolated in the missing GPS data for the first outage using only the data collected. We assumed the path seen in Figure 59 was unknown. To create the missing data, we took the last and first reliable GPS points before and after the outage. These points were again determined by the $loc_{n,GPS}$ plots. Recall for latitude and longitude, the first several points after the outage fluctuated before smoothing out. So for these coordinates, the last point was at IMU n = 8074, and the first point was at n = 21243. These correspond to t = 417782.8 and 417914.5. Because the altitude readings were not as consistent as the others, the last and the first were much earlier and later in time. In this case, n = 4794 and 22793, which were at t = 417750 and 417930. With these two points, we created a linear path between them and calculated $loc_{n,GPS}$ at 0.1 sec intervals. For these results, the number of GPS measurements increased to 2853. All other calculations, such as the common measured times and updated IMU locations, were completed the same way.

67

With the locations in the same reference frame, common measurement times established, and times that had weak or no GPS connection identified, the $loc_{n,IMU}$ and the $loc_{n,GPS}$ were combined. For the probability masses, two propositions exist: location known (L) and location not known (N). Thus, the frame of discernment is $\theta = \{L, N\}$, and the power set is $2^\theta = \{\emptyset, L, N, L \cup N\}$. Then we defined the probability mass functions as the following:

$$m_{n,i}(L) = \frac{1}{\sqrt{2\pi}\sigma_n^*} \exp\left(-\frac{(loc_{n,i} - \mu_n^*)^2}{2(\sigma_n^*)^2}\right), \qquad (22)$$

$$m_{n,i}(N) = 1 - m_{n,i}(L). \qquad (23)$$

So the total probability masses become:

$$m_{n,DST}(L) = K * [m_{n,IMU}(L) * m_{n,GPS}(L)], \qquad (24)$$

$$m_{n,DST}(N) = K * [m_{n,IMU}(N) * m_{n,GPS}(N)], \qquad (25)$$

where K, the normalizing constant, was calculated by (7). Because no mass was assigned to θ, the degrees of belief are equal to their probability masses. Note each mass above consists of three values for latitude, longitude, and altitude. The same is true for σ_n^* and μ_n^*. So $\sigma_n^* = (\sigma_{n,lat}, \sigma_{n,lon}, \sigma_{n,alt})$, and $\mu_n^* = (\mu_{n,lat}, \mu_{n,lon}, \mu_{n,alt})$.

For the real-time results, the parameter σ_n^* for the mass functions varied depending on the coordinate and the IMU n. In both $m_{n,IMU}(L)$ and $m_{n,GPS}(L)$, $\sigma_{n,lat}$ and $\sigma_{n,lon}$ were set equal to $\sigma_{IMU1,n}$ and $\sigma_{IMU2,n}$, respectively. For the GPS mass, $\sigma_{n,alt}$ was equal to $\sigma_{GPS3,n}$. Then $\sigma_{n,alt}$ for the IMU mass changed depending on the IMU n. These values are shown in Table 16. Recall the GPS variance for altitude was much larger than the IMU. Since $alt_{n,GPS}$ and $alt_{n,GPS}$ differed more for $n \geq 22793$, a larger value was required.

Table 16: $\sigma_{n,alt}$

n	$m_{n,IMU}$
$n < 21163$	$\sigma_{IMU3,n}$
$21163 \leq n < 22793$	$100 * \sigma_{IMU3,n}$
$n \geq 22793$	σ_{GPS3}

Then σ_n^* for $m_{n,DST}$ was calculated by (10) from Chapter III. For latitude, the two inputs were $\sigma_{IMU1,n}$ and σ_{GPS1}, and for longitude, the inputs were $\sigma_{IMU2,n}$ and $\sigma_{GPS2,n}$. For altitude, the inputs were the values for $m_{n,IMU}$ from Table 16 and σ_{GPS3}.

Next μ_n^* for the real-time results was determined by $loc_{n,GPS}$ and $loc_{n,IMU}$. Each μ_n^* was the same in all three probability masses: $m_{n,IMU}$, $m_{n,GPS}$, and $m_{n,DST}$. Recall $\mu_n^* = (\mu_{n,lat}, \mu_{n,lon}, \mu_{n,alt})$. Then $\mu_{n,j} = A * j_{n,IMU} + B * j_{n,GPS}$, where j is the coordinate. Table 17 shows the values for A and B. Notice that when the GPS signal was determined to be weak, $\mu_{n,j}$ was adjusted to give a greater weight on the IMU location.

Table 17: A & B for $\mu_{n,j}$

		$n \leq 8074$		$n > 8074$	
j	GPS signal	A	B	A	B
lat	normal	0.5	0.5	0.5	0.5
	weak	0.8*	0.2	0.7	0.3
lon	normal	0.5	0.5	0.5	0.5
	weak	0.8*	0.2	0.7	0.3
alt	normal	0.5	0.5	0.6	0.4
	weak	0.7	0.3	0.7	0.3

There are several things to note about these calculations. In Table 17, 0.8* indicates that the IMU location is not the updated one but rather $lat_{n,IMUb}$ and $lon_{n,IMUb}$. Also after reacquiring GPS connection, first five 'weak' points were between IMU n = 21163 and n = 21203. Finally, for the weak signals where $n > 8074$, the $alt_{n,IMU}$ was not updated. So if $|alt_{n,IMUb} - alt_{n,GPS}| > 2.5$, $alt_{n,IMU}$ was calculated by

$$alt_{n,IMU} = alt_{n-1,IMUb} + \Delta alt_{n,IMU}$$

69

not by (21).

The post-collection results had similar values for σ_n^* and μ_n^* to the previous. Yet because many $loc_{n,GPS}$ that had poor readings were eliminated, less changes in these parameters were needed. Still $\sigma_{n,lat}$ and $\sigma_{n,lon}$ remained the same as before. For the altitude when $n < 22793$, the IMU's $\sigma_{n,alt}$ equaled $10 * \sigma_{IMU3,n}$, and all others for both GPS and IMU equaled σ_{GPS3}. The final mass's σ_n^* was again calculated by (10) with the inputs of the GPS and the IMU variances. Then μ_n^* was the average of the GPS and the updated IMU measurements except for $n \leq 8074$. Here $\mu_{n,lat}$ and $\mu_{n,lon}$ were calculated the same as the real-time results.

Like the total probability masses in Chapter III, several $m_{n,DST}(L)$ were equal to zero or one. So like (16), $m_{n,DST}(L)$ was again modified by adding or subtracting 10^{-16} if it equaled zero or one, respectively. This modification fixed any $loc_{n,DST}$ that were infinite or undefined.

Finally, after determining $loc_{n-1,DST}$, $loc_{n,IMU}$ was updated. The results are shown in Section 4.4. Note that the true latitude, longitude, and altitude of the cart path are unknown. So there was no way to determine the accuracy of these results. The map in Figure 59 did, however, provide a rough estimate.

4.4   Results

The following figures show the results of applying the Dempster-Shafer Method to the data from the GPS and the IMU sensors. Again the true location is unknown. We first examined the real-time results and then the post-collection results. Last we looked at the results where the second GPS outage occurred.

Note that the IMU indicated in the figures is $loc_{n,IMUb}$. The updated IMU was very similar to $loc_{n,DST}$ and, thus, not shown in the plots. Also where $loc_{n,DST}$ (green line) on the plots cannot be seen, it is almost equal to $loc_{n,GPS}$ (red line). At these points, the green line is under the red.

70

Figure 64 shows the latitude for the two sensors and the combined given the real-time fusion. In the first part, the DST locations were continuous, instead of jumping like the GPS did. Then $lat_{n,DST}$ was slightly greater than $lat_{n,IMUb}$ because $lat_{n,GPS}$ was taken into account. Around t = 417780, $lat_{n,DST}$ had another small increase above $lat_{n,IMUb}$. Notice the last GPS outputs had a large jump at the end. This caused the increase in $lat_{n,DST}$. The effect can be seen better in Figure 66, discussed later. Then once the GPS signal is lost, the DST locations ran parallel to the IMU. As the signal was reacquired, $lat_{n,DST}$ jumped around similar to but not as extreme as $lat_{n,GPS}$. Next $lat_{n,DST}$ smoothed out as the GPS signal did. Finally at the end, the latitude for the DST was slightly less than the GPS as $lat_{n,IMU}$ was accounted for, as well.
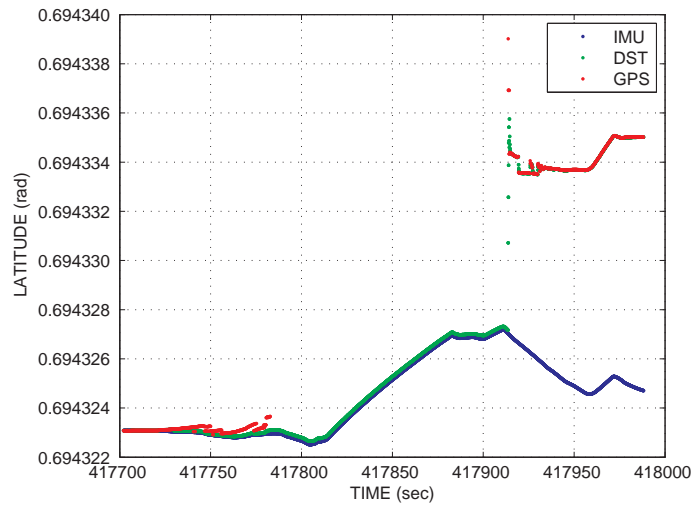

Figure 64: Latitude

The longitude results are shown in Figure 65. Since $lon_{n,GPS}$ and $lon_{n,IMUb}$ had similar trends as the latitude, the results for the longitude did, too. Again where the GPS signal was weak, $lon_{n,DST}$ did not show large jumps. The combined locations were between $lon_{n,IMUb}$ and $lon_{n,GPS}$. However, where $lon_{n,GPS}$ drifted further and jumped around, $lon_{n,DST}$ was slightly closer to $lon_{n,IMUb}$. Then at the same t that the latitude had a small increase, $lon_{n,DST}$ had a small decrease. Again $lon_{n,GPS}$ had two large decreases, making the DST value smaller. Next, $lon_{n,DST}$ ran parallel to

$lon_{n,IMUb}$ until the GPS signal was reacquired. At this time, we saw the same series of jumps for the DST as before. Once the GPS locations settled, $lon_{n,DST}$ and $lon_{n,GPS}$ followed very closely to one another. However, $lon_{n,DST}$ is smaller. Notice unlike the latitude, the GPS and the IMU were almost exactly parallel. Had the IMU not angled up, the two would have likely overlapped. This can also be seen in Figure 66.
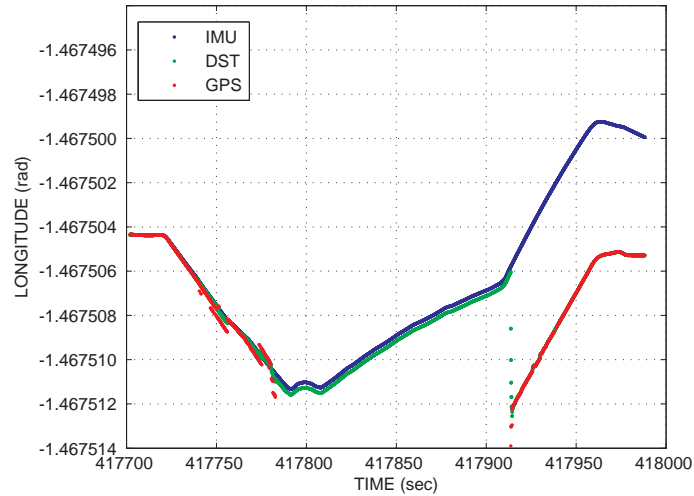

Figure 65: Longitude

In Figure 66, we saw the same results as the previous plots, just now in relation to the cart path. Recall around t = 417780 where $lat_{n,DST}$ had an increase and $lon_{n,DST}$ had a decrease. These coincide with the bottom left of the plot. Notice the DST results extended past the IMU. This placed them closer to the actual path. Then if the IMU had produced a 90° angle instead of a 45°, the DST results would have likely connected at the left end of the values as the GPS signal was reacquired. This would be similar to what we saw in the post-collection results.

Finally, Figure 67 shows the altitude for the two sensors and the DST. Clearly at most of the n's, $alt_{n,GPS}$ did not produce good locations and had significant jumps. However before t = 147750, both sensors had usable results. Here $alt_{n,DST}$ was between the GPS and the IMU and then slightly above. As $alt_{n,GPS}$ made large jumps, and the signal was completely lost, $alt_{n,DST}$ was solely determined by $alt_{n,IMU}$. Thus, like the other coordinates, $alt_{n,DST}$ ran parallel to the IMU outputs. Again for the
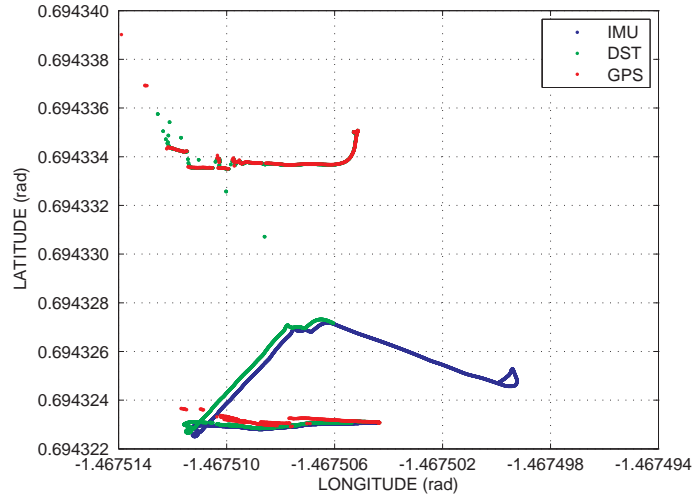
Figure 66: Longitude vs. Latitude

latter part, $alt_{n,GPS}$ jumped around before settling. The first five points had fairly large jumps. These were the same points that did so in the latitude and longitude. After these points, $alt_{n,DST}$ fell between the GPS and the IMU. Instead of the pattern of the GPS output, the DST results were reasonably continuous. Finally, after t = 417935, $alt_{n,GPS}$ smoothed out, and $alt_{n,DST}$ was similar but slightly less than the GPS measurement. Notice how the GPS and IMU began to converge at the end. Had the data collection continued, these values may had aligned.

Figure 67: Altitude

73

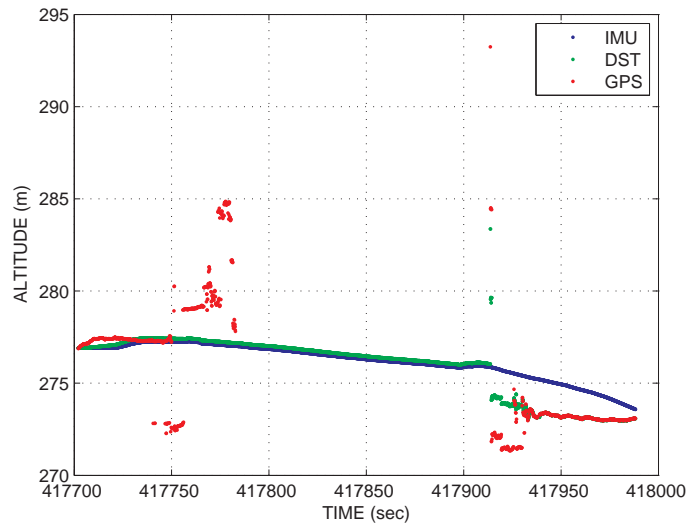Figures 68 - 71 show the results for the post-collection. Because we had estimated GPS data, we were able to apply the DST over the large outage. Also $loc_{n,IMU}$ was updated where previously it was not. For the latitude and the longitude, changes only occurred over this outage. So instead of running parallel to $loc_{n,IMUb}$, the combined made nearly continuous and direct path to locations as the cart exited the building. In both coordinates, there was a slightly jump at the beginning. This is best seen in Figure 70. Recall from Figure 66 the DST values extended past the IMU once combined with the last GPS measurement before the outage. This jump was a result of having new GPS measurements. Although it's difficult to see in the plots, $loc_{n,DST}$ was not equal to $loc_{n,GPS}$ over the outage. The combined latitude was slightly less than the GPS, and the combined longitude was slightly more.
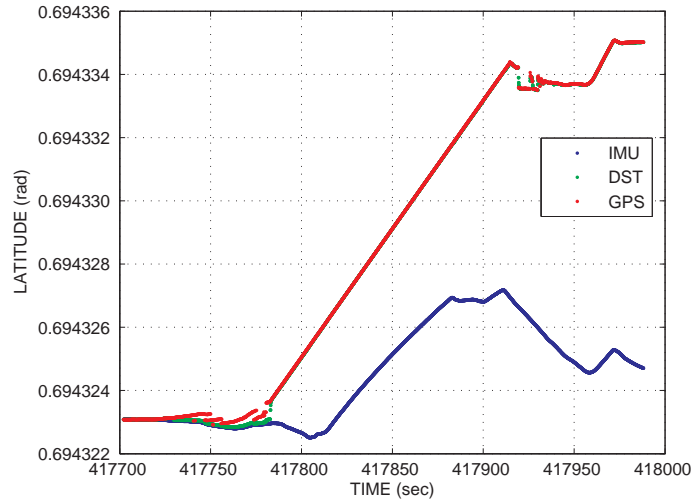
Figure 68: Post - Latitude
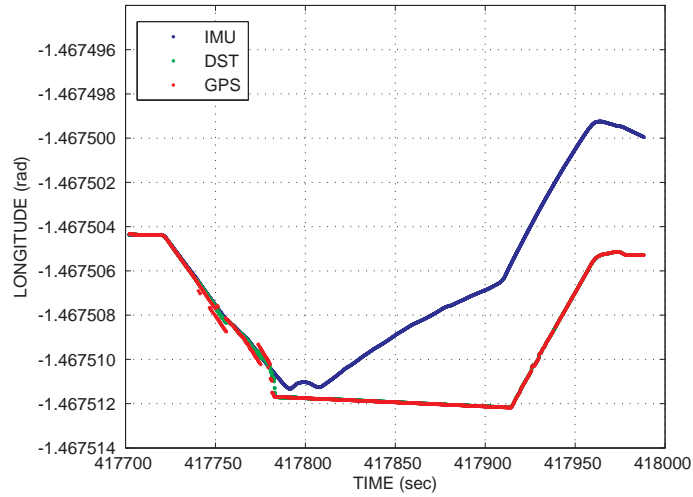
Figure 69: Post - Longitude
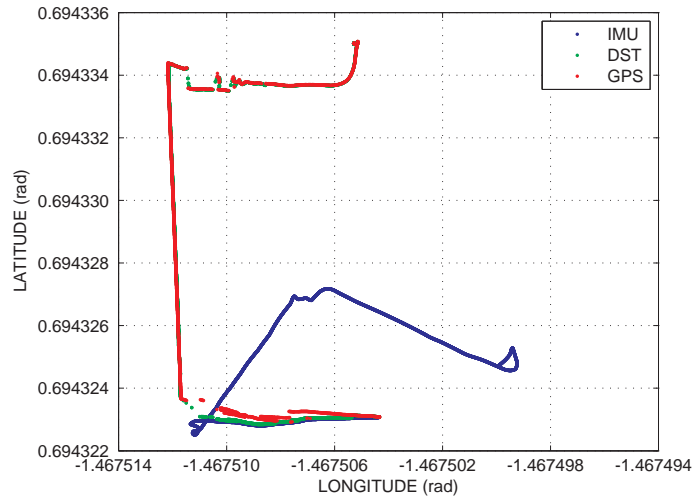
Figure 70: Post - Longitude vs. Latitude

Because of the greater fluctuations in its measurements, the results for the altitude differed more than the other coordinates. As about half of the GPS data before and after the outage was rather unreliable, the post-collection results disregarded these measurements. In this result, $alt_{n,DST}$ followed more closely to $alt_{n,GPS}$ at the beginning. Then when $alt_{n,GPS}$ was estimated, $alt_{n,DST}$ ran slightly above the estimates. Notice the small changes in $alt_{n,DST}$ that correspond to the changes in the IMU. The remaining $alt_{n,DST}$ at the end were the same as before.
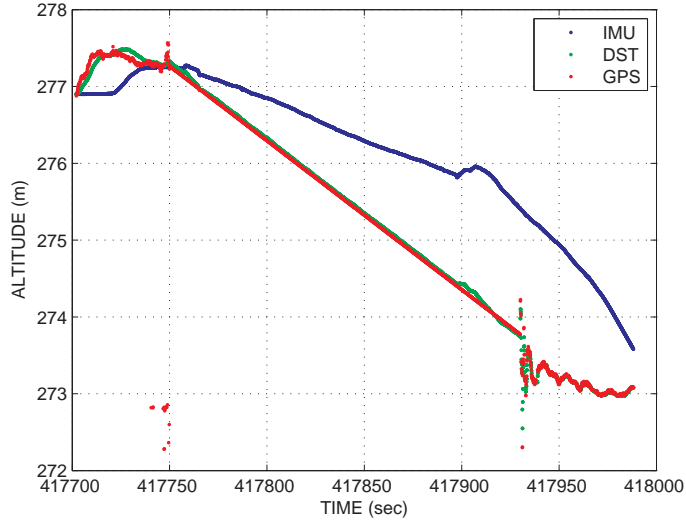
Figure 71: Post - Altitude

Figures 72 - 74 show the results of the DST when the GPS had a short outage. Between t = 417943 and 417944, the GPS briefly lost its connection. So $loc_{n,DST}$ was determined solely by $loc_{n,IMU}$. Note that in each figure the side axes for the two plots are not the same. For all of the coordinates, the slope of $loc_{n,DST}$ obvious matched that of the IMU. Then as soon as the GPS signal returned, and the IMU was updated with more accurate data, the points were again closely aligned with $loc_{n,GPS}$. Since the slopes of $lon_{n,GPS}$ and $lon_{n,IMU}$ were practically identical, it was almost impossible to tell if an outage occurred. Unfortunately the same was not true for latitude and altitude. For these, there was a slight jump as the GPS outputs returned.
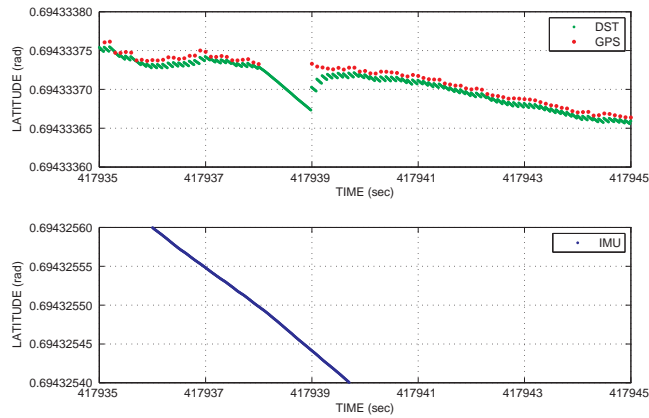
Figure 72: Latitude Outage
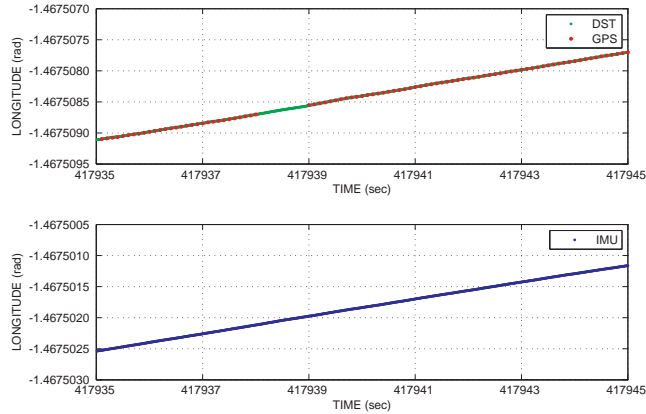
Figure 73:   Longitude Outage
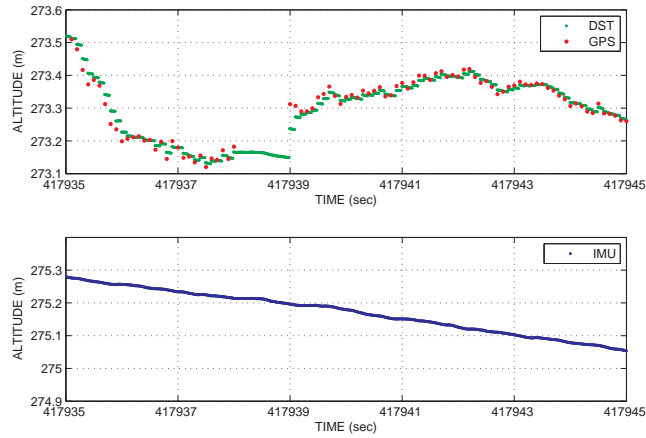
Figure 74:   Altitude Outage

4.5   Summary

With data from the GPS and the IMU sensors, we obtained the cart's location first in real-time and then after all the data was collected. For the real-time, the Dempster-Shafer Method produced positive results. Even during the outages we had slight improvements over the measurements of the single sensor. Then by completing the post-collection analysis, we were able to more accurately determine the true path that the cart traveled. Again these results can be used to repeat the same route if necessary, to further refine the calculations, or to modify the sensors.

Therefore by not making any assumptions about the two sensor models and with no prior information, we were able to combine the location data from a multi-sensor unit for a more precise determination of the cart's location. The Dempster-Shafer Method allowed us to assign evidence to probability mass functions. Then for different situations, such as a weak GPS signal, we were able to easily make modifications to these functions for better results. Because there was no true data, it was difficult to determine the accuracy of these results. However, with Figure 59 we saw improved results from $loc_{n,DST}$, thus, indicating another area where the DST was effectively applied.

V. Gait Analysis

5.1   Introduction

Gait means "a manner of walking or moving on foot" [16]. Gait analysis is the "evaluation of the manner or style of walking, usually done by observing the individual walking naturally in a straight line" [17]. Figure 75 shows the gait cycle, also known as a stride [18]. Everyone has a slightly different gait; however, a person's gait can still tell you a lot about him. For medical purposes, it can indicate an illness or injury. In athletics, people are able to improve their running by studying their gait[11]. Recently gait analysis has been used for identification purposes. The gait characteristics of a suspect can be compared to that of an unrecognizable criminal caught on camera [38]. Gait analysis is also being used to identify people with concealed weapons, such as potential suicide bombers. A person who appears to be heavy but is not will have a different gait than a person who is actually heavy [15].
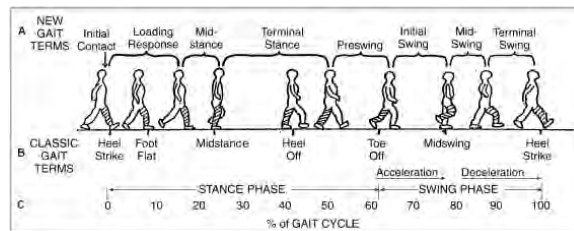
Figure 75:   Gait Cycle

Many different factors and parameters are involved in gait analysis. They include cadence, stride length, step length, joint angles (hip, knee, ankle), speed, and ground contact time [11; 27]. These measurements are easy to obtain because they can be made through observational analysis, either by a camera or an observer.

In the following two examples, the DST and gait analysis combined will be used to make decisions about individuals. Because this theory does not require prior knowledge, it is an advantage to use. By merely observing individuals, we can come to conclusions without having to obtain or assume any other information about them. We do, however, rely on the expertise of the observer to make the probability mass functions. The first example has two specialists determining if a runner will match

his previous run time after an injury. In the other, observers decide on the source of a patient's pain.

These examples focused on four factors: speed, step length, ground contact time, and ankle angle. Note that while many of these factors work in conjunction, we choose to only focus on their individual impacts. Speed is distance divided by time with the focus on cadence. Step length is "the distance from the initial contact of one foot to initial contact of the opposite foot" [11, 9]. An illustration of step length is shown in Figure 76 [20]. The average adult has a step length of 2.3 feet [42]; however, person running can have a step length upwards of 3.85 feet [32]. Ground contact time
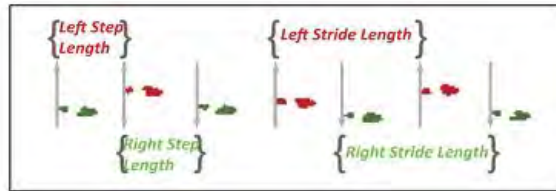
Figure 76: Step Length

is the amount of time that foot is in contact with the ground from heel strike to toe lift off, shown in Figure 77 [12]. By decreasing contact time, runners can increase their cadence and, thus, speed. Sprinters have ground contact times as small as 0.09 sec [64], but most runners are between 0.09-0.22 sec [32]. Finally, the ankle angle is

Figure 77: Ground Contact Time

the measure of degrees when the ankle is rotated up and down. When standing with legs perpendicular, 90°, to the floor, the ankle angle is at zero. Figure 78 illustrates this measurement [36]. When the foot strikes the ground, the ankle is extended down and then rotates up until the foot lifts off. When running the ankle will usually rotate

from -4° to 20°; walking from -8° to 14° [27]. The proper angles of strike and lift off allow the body to better absorb the force of impact [11].
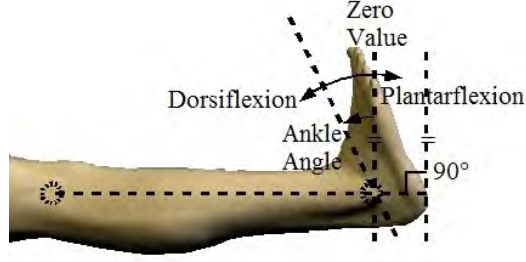
Figure 78: Ankle Angle

5.2 *Injured Runners*

Two athletic specialists were trying to determine if a runner, who recently had a knee injury, would match his 1.5 mile run time from the previous year. The propositions are then Yes (Y) and No (N). Thus, the frame of discernment is $\theta = \{Y, N\}$, and the power set is $2^\theta = \{\emptyset, Y, N, Y \cup N\}$. The specialists decided to consider three factors: step length, ground contact time, and ankle angle. For the last two, measurements were only taken on the same leg that the knee injury occurred. For each factor, they calculated the percent change from the previous year. Let $l_1, t_1, (a_{1,s}, a_{1,l})$ be last year's measurements for length, time, and angle and $l_2, t_2, (a_{2,s}, a_{2,l})$ be this year's, where $a_{i,s}$ is the angle at strike and $a_{i,l}$ at lift. Then the percent changes were calculated by the following:

$$\Delta l = \frac{l_1 - l_2}{l_1},$$

$$\Delta t = \frac{|t_1 - t_2|}{t_1}, \ \&$$

$$\Delta a = \sqrt{\frac{(a_{1,s} - a_{2,s})^2 + (a_{1,l} - a_{2,l})^2}{a_{1,s}^2 + a_{1,l}^2}}.$$

81

Based on their expertise, they assigned evidence to each proposition. Because they were not 100% certain, some of the evidence was assigned to θ, i.e. ignorance. For step length, they gave the following the probability masses:

$$
m_{A,l}(Y, N, \theta) = \begin{cases} (0.90, 0.05, 0.05), & \text{if } \Delta l \leq 0 \\ (0.80, 0.15, 0.05), & \text{if } 0 < \Delta l \leq 0.20 \\ (0.50, 0.45, 0.05), & \text{if } 0.20 < \Delta l \leq 0.40 \\ (0.40, 0.55, 0.05), & \text{if } \Delta l > 0.40 \end{cases}
$$

&

$$
m_{B,l}(Y, N, \theta) = \begin{cases} (0.90, 0.04, 0.06), & \text{if } \Delta l \leq 0 \\ (0.70, 0.24, 0.06), & \text{if } 0 < \Delta l \leq 0.20 \\ (0.45, 0.49, 0.06), & \text{if } 0.20 < \Delta l \leq 0.40 \\ (0.30, 0.64, 0.06), & \text{if } \Delta l > 0.40. \end{cases}
$$

For ground contact time, the probability masses are

$$
m_{A,t}(Y, N, \theta) = \begin{cases} (0.85, 0.05, 0.10), & \text{if } if \ \Delta t = 0 \\ (0.65, 0.25, 0.10), & \text{if } 0 < \Delta t \leq 0.25 \\ (0.50, 0.40, 0.10), & \text{if } 0.25 < \Delta t \leq 0.50 \\ (0.35, 0.55, 0.10), & \text{if } \Delta t > 0.50 \end{cases}
$$

&

$$
m_{B,t}(Y, N, \theta) = \begin{cases} (0.90, 0.02, 0.08), & \text{if } \Delta t = 0 \\ (0.70, 0.22, 0.08), & \text{if } 0 < \Delta t \leq 0.25 \\ (0.45, 0.47, 0.08), & \text{if } 0.25 < \Delta t \leq 0.50 \\ (0.30, 0.62, 0.08), & \text{if } \Delta t > 0.50. \end{cases}
$$

Finally for ankle angle, the probability masses are

$$
m_{A,a}(Y, N, \theta) = \begin{cases} (0.92, 0.04, 0.04), & \text{if } \Delta a \le 0.05 \\ (0.70, 0.26, 0.04), & \text{if } 0.05 < \Delta a \le 0.15 \\ (0.48, 0.48, 0.04), & \text{if } \Delta a > 0.15 \end{cases}
$$

&

$$
m_{B,a}(Y, N, \theta) = \begin{cases} (0.90, 0.03, 0.07), & \text{if } \Delta \le 0.05 \\ (0.75, 0.18, 0.07), & \text{if } 0.05 < \Delta a \le 0.15 \\ (0.45, 0.48, 0.07), & \text{if } \Delta a > 0.15. \end{cases}
$$

Note these probability mass assignments were determined based on information from [25; 27; 33].

Again the expertise of the specialists is not prior knowledge. However, anything known about the runners beyond the percent changes is. For instance, Specialist A has prior knowledge if he knows that Runner X injured his knee several years before and then did not met his previous run time.

Using MATLAB, we generated random values between 0 and 1 for the length's and the contact time's percent changes for 15 runners. For the ankle angle's change, values were generated between 0 and 0.50 since the ankle can only rotate a set number of degrees. The percent changes are shown in Figure 18.

With these percent changes, we first determined whether the runner would at least match his time based on the individual factors. In other words, we combined the evidence from each specialist for step length, contact time, and ankle angle. Then we combined these three results for a final decision whether the runner's time would decrease based on all of the factors. Each decision was made by selecting the proposition with the largest probability mass (degree of belief). The results are in Table 19. 'Combined' indicates the combination of the three factors and, thus, the final result.

Table 18: % Changes

	FACTOR		
RUNNER	Length	Time	Angle
1	0.8147	0.9058	0.1270
2	0.9134	0.6324	0.0975
3	0.2785	0.5469	0.1576
4	0.9706	0.9572	0.3854
5	0.8003	0.1419	0.2218
6	0.9157	0.7922	0.0357
7	0.8491	0.9340	0.1922
8	0.6555	0.1712	0.0318
9	0.2769	0.0462	0.0971
10	0.8235	0.6948	0.1171
11	0.9502	0.0344	0.4387
12	0.3816	0.7655	0.1369
13	0.4898	0.4456	0.2760
14	0.6797	0.6551	0.1626
15	0.1190	0.4984	0.1404

Table 19: Will the Runner Match His Time?

	FACTOR			
RUNNER	Length	Time	Angle	Combined
1	NO	NO	YES	YES
2	NO	NO	YES	YES
3	YES	NO	NO	NO
4	NO	NO	NO	NO
5	NO	YES	NO	YES
6	NO	NO	YES	YES
7	NO	NO	NO	NO
8	NO	YES	YES	YES
9	YES	YES	YES	YES
10	NO	NO	YES	YES
11	NO	YES	NO	YES
12	YES	NO	YES	YES
13	NO	YES	NO	NO
14	NO	NO	NO	NO
15	YES	YES	YES	YES

Figures 79 and 80 show the probability masses for the four results. Because the probability masses were based on a range of percentages, some of the runners had

the same probability mass for one or more of the factors. Notice some of the masses clearly indicated Yes or No. Runner 8's $m_t(Y)$ was greater than 0.80. However, others were less conclusive. These masses for Yes and No were almost equal. For instance, $m_a(Y) = 0.49$ and $m_a(N) = 0.51$ for Runner 4.
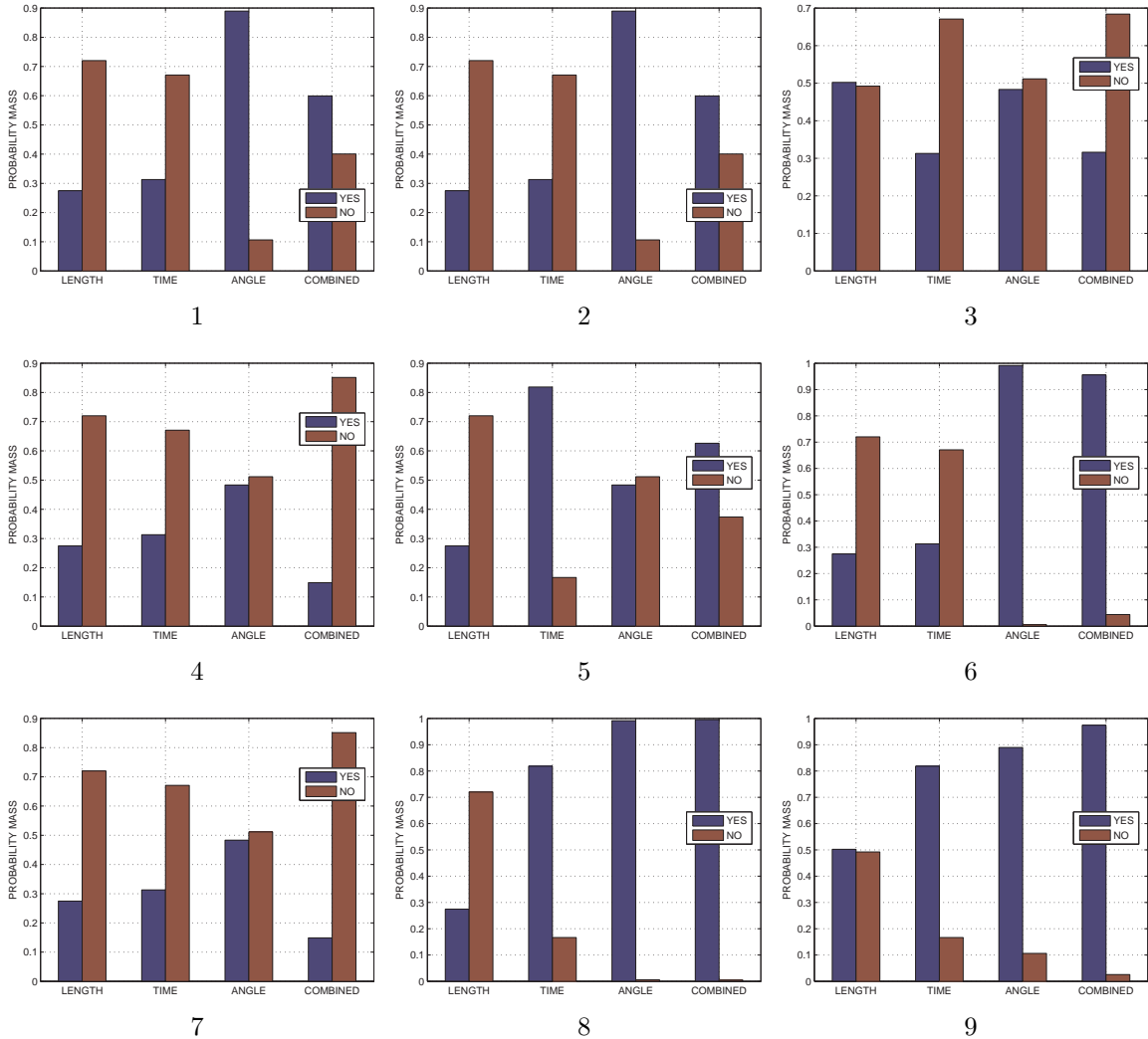

Figure 79: Probability Masses

Notice the Combined conclusions for runners 1, 2, 5, 6, 10, and 11 in Table 19. Although two of the three factors indicated that they would not match their run times, the Combined results showed that they would. Looking at their probability masses, we can see why. For Runners 1, 2, and 10, the ankle angle mass for Yes was
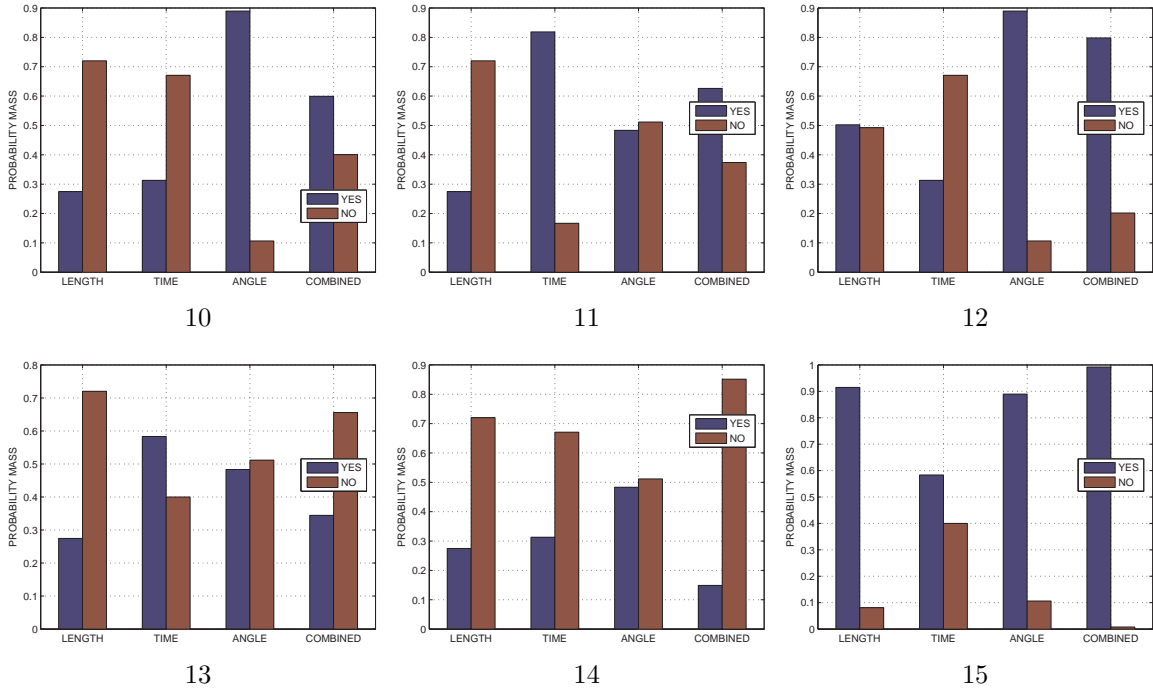
Figure 80: Probability Masses (cont.)

very high, approximately 0.90. Yet the length and time masses for No were only near 0.70. Then the final decisions came out very close with $m(Y, N) \approx (0.60, 0.40)$. For Runners 5 and 11, the Combined masses were not as close but still close. In this case, $m_a(N)$ was slightly greater than $m_a(Y)$. Then we had the length's mass strongly concluding No and the time's strongly concluding Yes. Since $m_t(Y) > m_l(Y)$, the Combined concluded Yes. Finally, Runner 6's Combined probability mass was very conclusive for Yes, $m(Y) = 0.95$. Clearly this result was heavily impacted by the ankle angle. As the chart shows, $m_a(Y) \approx 0.99$. The masses for the other factors were around 0.30. Thus, in combining the three, the probability mass for Yes came out much stronger than for the previous runners.

As outlined in Section 2.1, degrees of belief and plausibility define uncertainty intervals. Because evidence was assigned to ignorance, the length of this interval was not zero. We had a small "freedom of motion." Then for each factor and the Combined, $Bel_x(b_i) = m_x(b_i)$ and $Pl_x(b_i) = m_x(b_i) + m_x(\theta)$ for $b_i \in 2^\theta$. Thus $m_x(\theta)$ is the length. For example, $m_t(Y, \theta) = (0.8185, 0.014815)$ for Runner 5. So its uncertainty

86

interval was $[Bel_t(Y), Pl_t(Y)] = [0.8185, 0.833315]$. Similarly the Combined interval for No was $[Bel(N), Pl(N)] = [0.3739, 0.373902]$. The ignorance or the length of each interval is shown in Table 20. Notice as more evidence was combined, the ignorance decreased. In other words, $m_x(\theta)$ was smaller than $m_{A,x}(\theta)$ and $m_{B,x}(\theta)$, but $m(\theta)$ was the smallest.

Table 20: Ignorance

RUNNER	$m_l(\theta)$	$m_t(\theta)$	$m_a(\theta)$	$m(\theta)$
1	0.005181	0.016260	0.004124	0.00000253
2	0.005181	0.016260	0.004124	0.00000253
3	0.005430	0.016260	0.005058	0.00000173
4	0.005181	0.016260	0.005058	0.00000141
5	0.005181	0.014815	0.005058	0.00000213
6	0.005181	0.016260	0.002990	0.00000263
7	0.005181	0.016260	0.005058	0.00000141
8	0.005181	0.014815	0.002990	0.00000099
9	0.005430	0.014815	0.004124	0.00000085
10	0.005181	0.016260	0.004124	0.00000253
11	0.005181	0.014815	0.005058	0.00000213
12	0.005430	0.016260	0.004124	0.00000195
13	0.005181	0.016667	0.005058	0.00000183
14	0.005181	0.016260	0.005058	0.00000141
15	0.004267	0.016667	0.004124	0.00000059

Discussed in Section 2.3, when the degrees of conflict are high, Dempster's Rule can produce the wrong conclusion. To make sure this did not occur, we shifted focus onto the degrees of conflict for each runner. Figure 81 shows the degrees for each factor and the Combined. Since the probability mass for the Combined was the result of combining three masses (m_l, m_t, m_a), Dempster's Rule was applied twice. Thus, its degree of conflict was the average of the degrees from the two applications. For the individual factors, the degrees were all below 0.50. The Combined degrees were all below 0.61, also an acceptable value. For the six runners previously mentioned, their degrees of conflict were slightly larger than the others, but nothing extreme that would lead to the wrong result. For instance, Runner 10 had a Combined degree of

conflict of 0.59 while Run 3's degree was 0.49. Therefore, there is no concern that the degrees of conflict adversely affected the final conclusions.
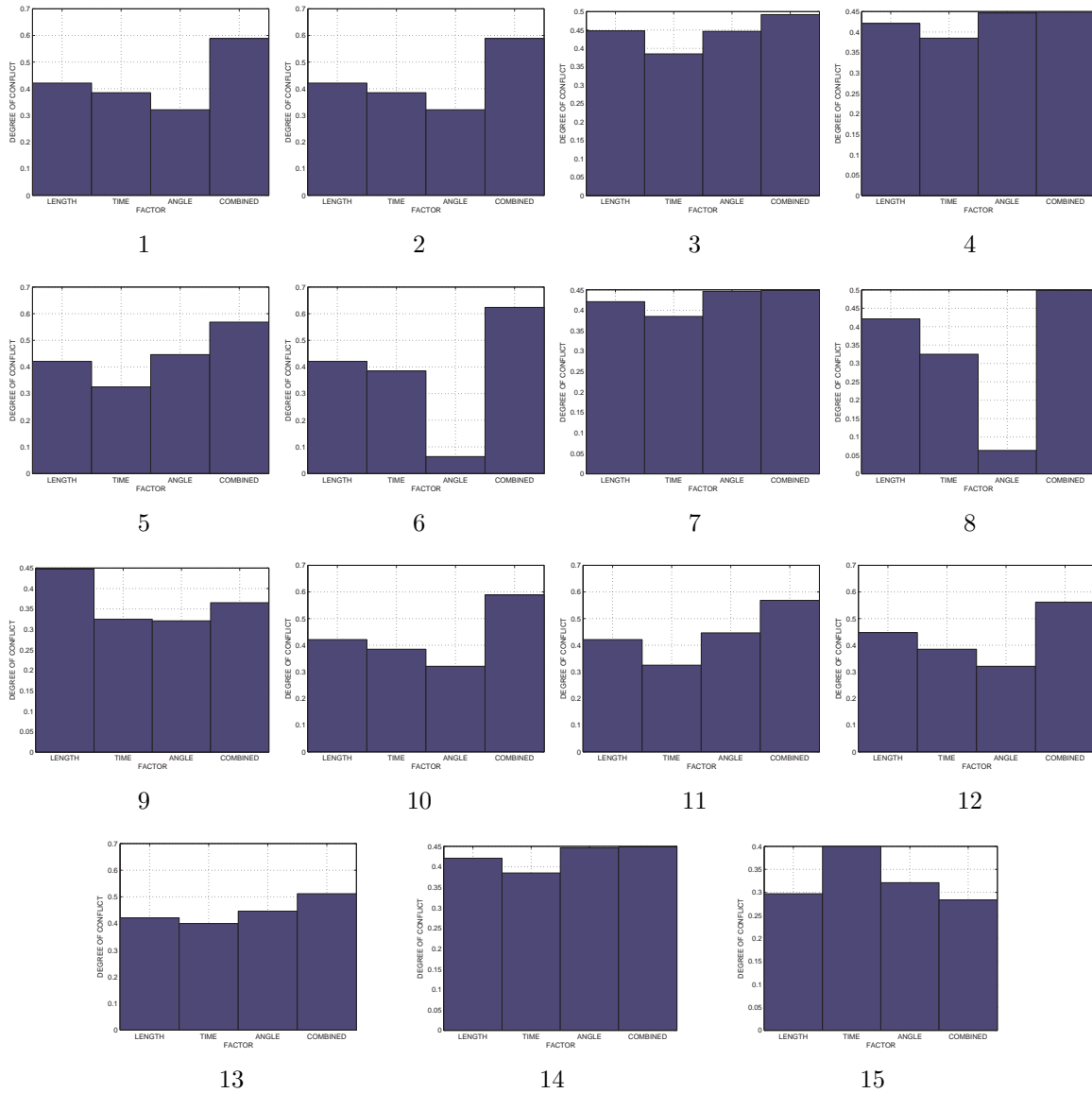

Figure 81: Degrees of Conflict

Thus without concern for problems with the degrees of conflict, we have an accurate method to combine the evidence given by the specialists. Through mere observation and not relying on other information about the runners, we were able to conclude whether these runners would meet their previous run times.

5.3 Diagnosis & Degrees of Conflict

Two observers decided to use gait analysis to diagnose the source of a physical pain. Each observer had two different basic probability assignments. The first version is denoted LOW, and the second HIGH. One resulted in an accurate conclusion; the other incorrect. Using these two assignments, we illustrate the major criticism of the DST, discussed in Section 2.3. As the degree of conflict increases, there's a greater chance that Dempster's Rule will produce an incorrect result.

After watching a group of people over a certain time period, two observers were attempting to diagnosis whether a person is having back (B), knee (K), or ankle (A) pain. So the frame of discernment is $\theta = \{B, K, A\}$, and the power set is $2^\theta = \{\emptyset, B, K, A, B \cup K, B \cup A, K \cup A, B \cup K \cup A\}$. Because a problem with one of these usually affects the other two, the observers were looking for the root cause and excluded any interactions. That is, each pain was treated as mutually exclusive.

The observers considered the following factors: walking speed, step length, ground contact time, and ankle angle. The latter two were again measured on the problem leg. Unlike in Section 5.2, the observers were only looking for any change that occurred by more than 10% within these factors, not how much it changed.

In the LOW version, Observer A assigned each factor the following probability masses:

$$
m_A(B, K, A, \theta) = \begin{cases} (0.33, 0.33, 0.33, 0.01), & \text{if speed changes} \\ (0.85, 0, 0.05, 0.10), & \text{if length changes} \\ (0.15, 0.75, 0, 0.10), & \text{if time changes} \\ (0, 0.10, 0.80, 0.10), & \text{if angle changes.} \end{cases}
$$

Observer B disagreed slightly to the other observer's masses and used the following assignments:

$$
m_B(B, K, A, \theta) = \begin{cases} (0.34, 0.32, 0.33, 0.01), & \text{if speed changes} \\ (0.85, 0.10, 0, 0.05), & \text{if length changes} \\ (0, 0.80, 0.10, 0.10), & \text{if time changes} \\ (0.15, 0, 0.80, 0.05), & \text{if angle changes.} \end{cases}
$$

Note both observers assigned evidence to ignorance. Also the four masses from each observer do not have much agreement, but there is more agreement between the observers. This impacted the degrees of conflict, discussed later.

The probability masses were based on personal experience and slightly manipulated to fix the context of the example. With more expertise, these masses can be improved.

As noted in Section 5.2, no prior knowledge is required for these probability masses. For example, one of the observers knowing that a patient has reoccurring back problems is prior knowledge. We assumed that the observers' contact with the patients was limited to watching them walk.

Requiring at least two types of changes to occur, there are eleven different combinations possible to make a diagnosis. For these combinations, (X_1, X_2, X_3, X_4) means a change in (speed, length, time, angle) when $X_i = 1$ and no change when $X_i = 0$. Figure 82 shows probability masses for the diagnoses from each observer and the Combined. 'Combined' refers to the orthogonal sum of the probability masses of Observers A and B. The diagnosis was determined by selecting the proposition with the largest probability mass (degree of belief).
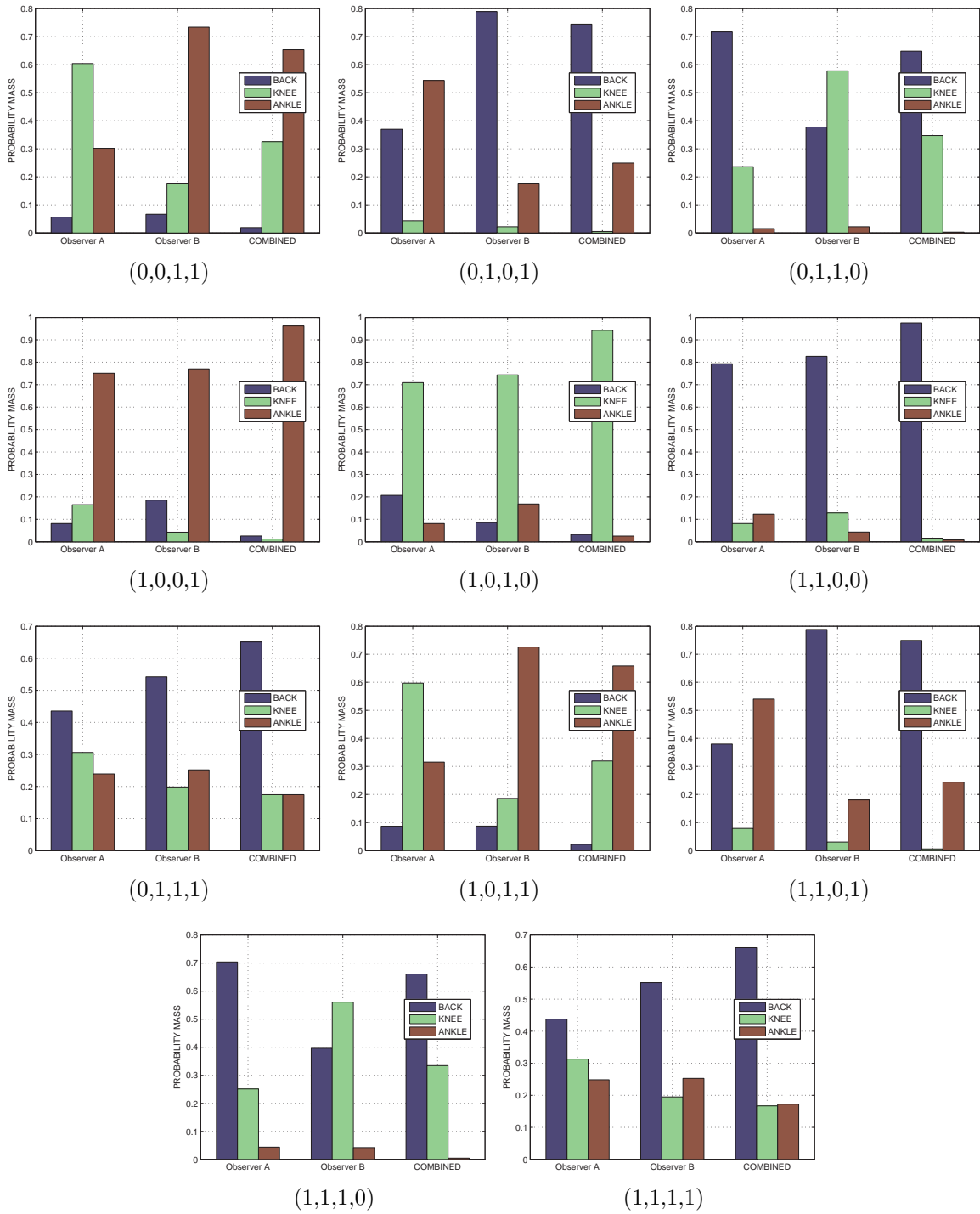
Figure 82: LOW Probability Masses

Each observer was strongly in favor of one source in almost every case. In other words for each observer, the largest probability mass was greater than 0.50 and

was at least 0.10 higher than the other two masses. In (0,1,0,1), $m_A(B, K, A) \approx$ (0.38, 0.04, 0.53). The exceptions were (0,1,1,1) and (1,1,1,1). For these, $m_A(B)$ was still greater than $m_A(K)$ and $m_A(A)$ by more than 0.10, but it was not greater than 0.50. These two cases made having the second observer more important.

However, in more than half of the combinations, the observers' conclusions did not agree. In (0,0,1,1), Observer A concluded Knee as the source of pain, but Observer B concluded Ankle. Notice, in these cases, the proposition with the largest mass for one observer was the proposition with the second largest for the other. Then this second largest mass was at least 0.30 if this largest mass was greater than the other largest mass. This is best illustrated in an example. In (1,1,1,0), $m_A(B) = 0.70 >$ $m_B(K) = 0.56$, but $m_B(B) = 0.40$. Because of these two factors, the Combined resulted in the source of pain that had the largest overall mass between the two observers. In (1,1,1,0), $m_A(B) = 0.70$ was the largest between the observers, so in the Combined, $m(B) = 0.66$ was largest. Therefore, while one observer did not agree with the conclusion of the other, he still gave approximately one third of the evidence in support of the other's conclusion. Also this other gave more evidence in support of his conclusion than the first.

Finally, much like each observer, the Combined probability masses showed strong evidence in favor of only one proposition. In every combination, the largest mass was greater than 0.65. In three cases, the largest mass was above 0.90. Based on all of these conclusions, the resulting sources of pain seemed to have strong evidence in favor of them, and there was little to suggest that conflict was an issue. Still we looked into the degrees of conflict later in this section.

Then the observers decided to modify their probability assignments. In this version, there were similar disagreements between the four masses, but there was much less agreement between the observers. However, each was still confident in his decision, and both observers assigned the same amount of evidence to ignorance. So

for HIGH, Observer A's basic probability assignment became:

$$m_A(B, K, A, \theta) = \begin{cases} (0.33, 0.33, 0.33, 0.01), & \text{if speed changes} \\ (0.05, 0, 0.85, 0.10), & \text{if length changes} \\ (0.75, 0.15, 0, 0.10), & \text{if time changes} \\ (0, 0.80, 0.10, 0.10), & \text{if angle changes.} \end{cases}$$

And Observer B's was then the following:

$$m_B(B, K, A, \theta) = \begin{cases} (0.34, 0.32, 0.33, 0.01), & \text{if speed changes} \\ (0.10, 0.85, 0, 0.05), & \text{if length changes} \\ (0, 0.10, 0.80, 0.10), & \text{if time changes} \\ (0.80, 0, 0.15, 0.05), & \text{if angle changes.} \end{cases}$$

Again requiring at least two types of changes to occur, there are eleven different combinations possible to make a diagnosis. Figures 83 and 84 show the probability masses for the diagnoses from each observer and the Combined.
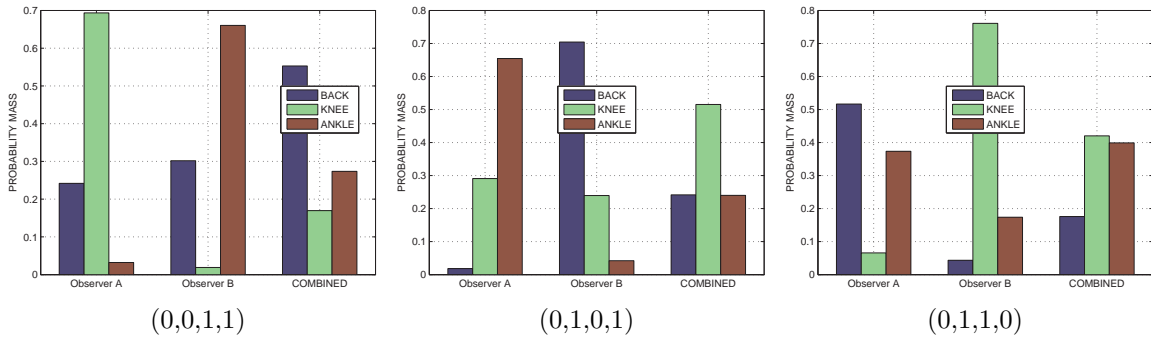

Figure 83: HIGH Probability Masses

Like the LOW version, each observer had strong evidence in favor of one source in every case except in (0,1,1,1) and (1,1,1,1). The largest probability mass was greater than 0.50 and was at least 0.10 higher than the other two masses. In (0,1,1,0), $m_A(B, K, A) \approx (0.51, 0.07, 0.38)$. However, in (0,1,1,1) and (1,1,1,1), the probability

(1,0,0,1)

(1,0,1,0)

(1,1,0,0)

(0,1,1,1)

(1,0,1,1)

(1,1,0,1)

(1,1,1,0)

(1,1,1,1)
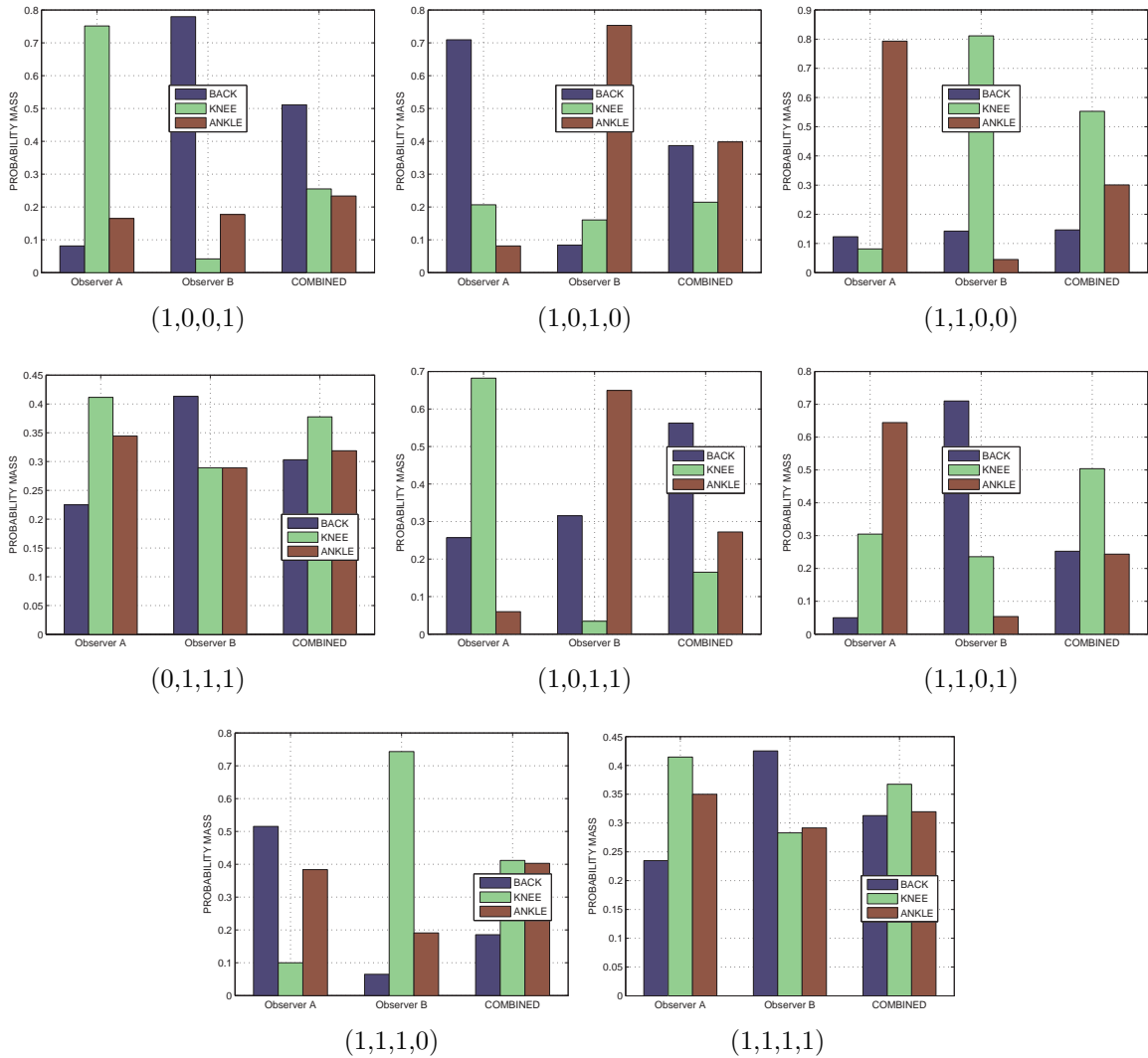
Figure 84: HIGH Probability Masses (cont.)

masses for both observers were closer together. While one mass was clearly larger than the others, it was not greater than 0.50. Again having the second observer became more important. Note that these were the same combinations that had this problem in the LOW version.

A major change from LOW was that none of the observers' conclusions agreed. If A thought it was back pain, then B concluded knee or ankle. Also the propositions with the second largest probability masses were always the same. For example in (1,1,1,0), ankle pain had the second largest mass for Observers A and B, but the

largest for Observers A and B was back and knee, respectively. Because of these two factors, the Combined result had much less evidence in support of it and possibly contradicted both observers' conclusions.

For every case in the Combined results, the largest probability mass was at most 0.55. In five of the eleven cases, the results were fairly inconclusive. In (0,1,1,0), (1,0,1,0), and (1,1,1,0), the two largest masses were almost equal. For example in (0,1,1,0), $m(K, A) = (0.41, 0.40)$. In the other two, (0,1,1,1) and (1,1,1,1), each mass was approximately one third of the total evidence.

In another four of the cases, the Combined results contradicted the observers'. The concluded source of pain for the Combined was not the same as those of the observers. In (0,0,1,1) Observer A concluded Knee, and Observer B concluded Ankle. Yet the Combined concluded Back. Also the largest probability masses were greater than 0.50 with the 2 smaller masses less than 0.30. For example in (0,1,0,1), $m(B, K, A) = (0.22, 0.51, 0.22)$.

In the last two cases, (1,0,0,1) and (1,1,0,0), the Combined conclusion came out the same as Observer B's with a mass greater than 0.50. However, Observer A strongly concluded a different diagnosis with a mass greater than 0.75. Thus one would assume that the Combined would come out fairly inconclusive, but obviously from the figures it did not. Because of all of these results, we examined the degrees of conflict.

In both versions, evidence was assigned to ignorance. So we again had uncertainty intervals. Like Section 5.2, $Bel_x(b_i) = m_x(b_i)$, and $Pl_x(b_i) = m_x(b_i) + m_x(\theta)$ for $b_i \in 2^\theta$. For example, $m_A(A, \theta) = (0.7512, 0.002463)$ for LOW (1,0,0,1). Then its interval was $[Bel_A(A), Pl_A(A)] = [0.7512, 0.753663]$. Also the Combined interval for Knee was $[Bel(K), Pl(K)] = [0.0122, 0.012205]$. Table 21 shows the ignorance for each case.

Notice some of the values are larger than others. For HIGH (0,1,0,1), $m_A(\theta) = 0.036364$ and for HIGH (1,1,1,0), $m_A(\theta) = 0.001191$. Also for LOW (0,1,1,0), $m(\theta) =$

Table 21: Ignorance

CASE	VERSION	$m_A(\theta)$	$m_B(\theta)$	$m(\theta)$
(0, 0, 1, 1)	LOW	0.037736	0.022222	0.00214133
	HIGH	0.032258	0.018868	0.00385356
(0, 1, 0, 1)	LOW	0.043478	0.011111	0.00108992
	HIGH	0.036364	0.014085	0.00320000
(0, 1, 1, 0)	LOW	0.031496	0.022222	0.00151976
	HIGH	0.043956	0.021739	0.00472255
(1, 0, 0, 1)	LOW	0.002463	0.001335	0.00000544
	HIGH	0.002463	0.001312	0.00002527
(1, 0, 1, 0)	LOW	0.002463	0.002513	0.00001097
	HIGH	0.002463	0.002469	0.00003827
(1, 1, 0, 0)	LOW	0.002463	0.001314	0.00000479
	HIGH	0.002463	0.001368	0.00002737
(0, 1, 1, 1)	LOW	0.019139	0.007634	0.00038081
	HIGH	0.019139	0.008264	0.00046680
(1, 0, 1, 1)	LOW	0.001034	0.000629	0.00000186
	HIGH	0.000893	0.000531	0.00000327
(1, 1, 0, 1)	LOW	0.001179	0.000313	0.00000092
	HIGH	0.000999	0.000398	0.00000277
(1, 1, 1, 0)	LOW	0.000873	0.000630	0.00000130
	HIGH	0.001191	0.000626	0.00000408
(1, 1, 1, 1)	LOW	0.000543	0.000219	0.00000032
	HIGH	0.000543	0.000238	0.00000040

0.00151976, but for LOW (1,1,1,1), $m(\theta) = 0.00000032$. This was the result of two factors. First, as more probability masses were combined, we reduced the uncertainty from our data. Compare (0,0,1,1) and (0,1,1,1). For both the LOW and the HIGH versions, $m_x(\theta)$ decreased in (0,1,1,1). The other factor was the amount of ignorance. If the speed changed, $m_x(\theta) = 0.01$. This mass combined with any other significantly reduced the overall ignorance.

The degrees of conflict are shown in Figure 85. The degrees for the last five combinations for Observers A and B were averages of the degrees from each application of Dempster's Rule. Again LOW indicates the first version and HIGH the second.

Notice that the degrees of conflict for Observers A and B were relatively the same between LOW and HIGH. In both versions, 32 of the 44 degrees of conflict for
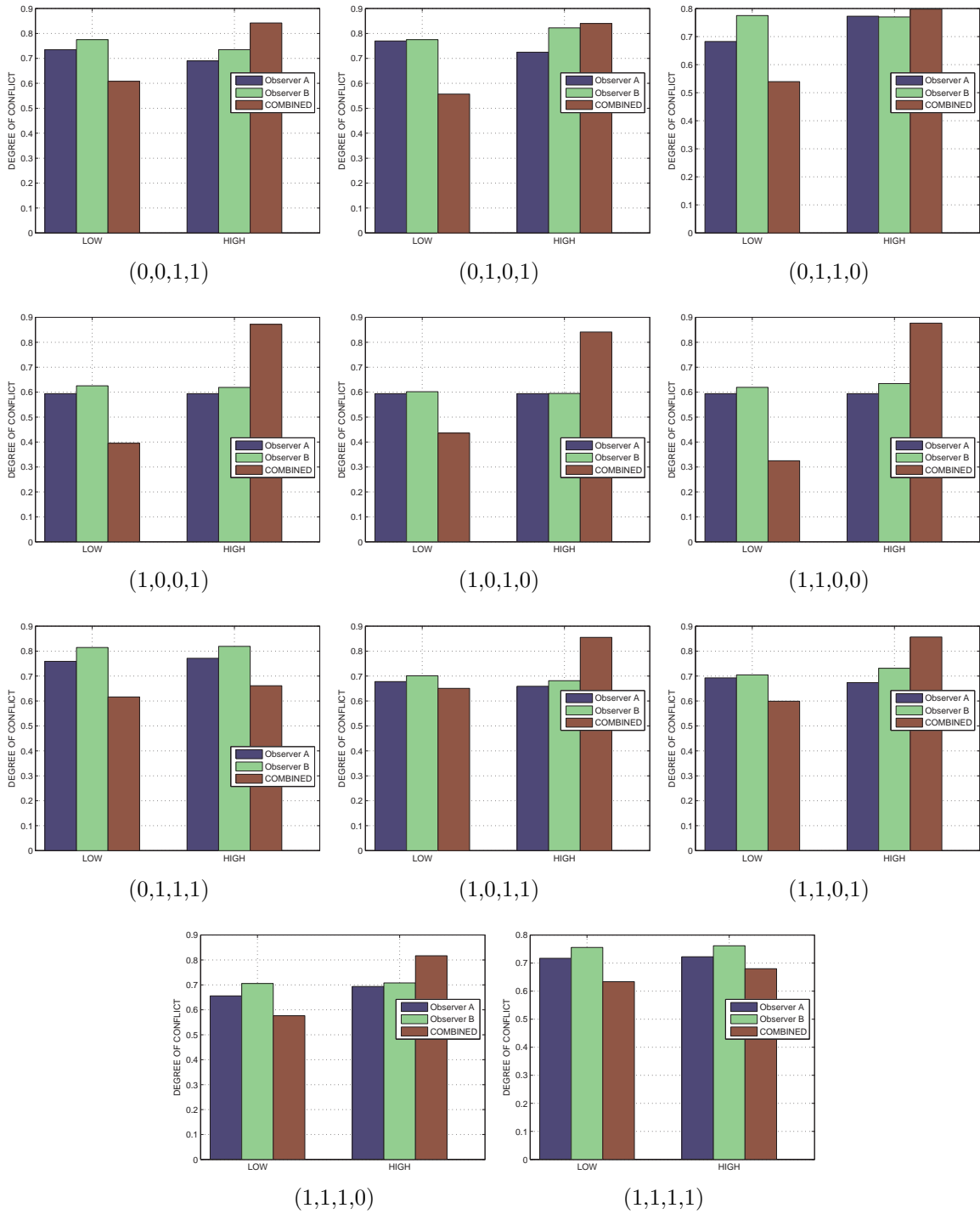
Figure 85: Degrees of Conflict

both observers were greater than 0.70, but only three of 32 were above 0.80. The remaining twelve were around 0.60. These values were somewhat expected as a result

of probability mass assignments. Excluding the assignments for speed changes, the others gave the majority of evidence to one proposition and a small amount to another. Then for each type of change (length, time, and angle), the propositions that had evidence also changed. For instance in the LOW version $m_A(B, K, A) = (0.85, 0, 0.05)$ if the step length changed, but $m_A(B, K, A) = (0.15, 0.75, 0)$ if the ground contact time changed. So the results we obtained were anticipated.

The degrees of conflict for the Combined were quite different. For the LOW version, most of the degrees were below 0.60, but the largest was only 0.65. Recall, though, all of the results had strong supporting evidence. For HIGH, the degrees of conflict were much greater. In eight of eleven cases, the degrees were greater than 0.80, and in every case, the degrees were greater than those from LOW. In almost all cases, the differences between LOW and HIGH were at least 0.20 but in (1,1,0,0) the difference was 0.50. Yet in (0,1,1,1) and (1,1,1,1) the difference between the degrees was less than 0.05. Recall for the HIGH version, these cases were somewhat inconclusive; the probability masses for each pain were almost equal. Hence, as the HIGH version illustrated, high degrees of conflict between probability masses result in less supporting evidence and even incorrect conclusions.

Therefore the agreement between sources on how evidence is assigned clearly has a significant impact on the final conclusions. When the sources output conflicting information, Dempster's Rule is more likely to result in incorrect decisions. This was shown in the HIGH version. However, in cases where there's slightly more agreement, such as LOW, we can still obtain fast and accurate results through the Dempster-Shafer fusion process.

5.4 Summary

The examples in this chapter illustrated how the DST can be used in conjunction with gait analysis to make decisions about individuals. Through observation only we concluded how a runner would performed after an injury compared to the previous

year and on a person's source of pain by the change in his walk. Also because there was some uncertainty, evidence was assigned to ignorance. Thus, uncertainty intervals were produced, and we had "freedom of motion" for the probabilities. However, given higher conflict, we had problems obtaining accurate results.

VI. Conclusions

6.1 Summary

The Dempster-Shafer Theory is a data fusion method that assigns evidence based on belief. With this idea, ignorance is not an issue. We can represent ignorance by assigning evidence to $m(\theta)$ and can work with incomplete information. We are not required to know prior information about the data we obtain. Also, no assumptions have to be made, and the final results of the data fusion are not negatively influenced.

Using probability mass functions, evidence is assigned to belief. There is a lot of latitude with these functions. As seen in this research, equations, such as (13), can be used for large continuous or discrete data sets, where the parameters are change to get the desired outcome. Simple assignments, such as those in Chapter V, work, as well.

The DST does have problems as the degree of conflict approaches one. In some cases, Dempster's Rule produces incorrect results. Examples of this were shown in Sections 2.3 and 5.3.

The Dempster-Shafer Method has applications in many fields with excellent results. These include detection, recognition, classification, and decision-making. We used this method to determine an object's location and to make a conclusion about the status of an individual. Both areas of application showed promising results.

In Chapter III, we generated sensor data to track an aircraft's trajectory. Using four approaches, we fused the position measurements from the two sensors. Then in comparison to the Kalman filter, we had favorable results from the Dempster-Shafer Method.

In Chapter IV, real sensor data from a GPS and an IMU was combined to find the coordinates of a moving cart. By applying this method, we were able to more accurately determine the cart's path even when the GPS had outages.

Finally, after making a series of observations about individuals, evidence was assigned to probability masses in Chapter V. Then Dempster's Rule was used to

combine multiple masses. From the results, we made decisions about whether injured runners would meet their previous run times and the source of a patient's pain. Also because evidence was assigned to ignorance, we obtained uncertainty intervals. Thus, the probability that each proposition was true was not exact but lied within a range. Again in the second example, we showed what can happen with a high degree of conflict.

Without making assumptions and without prior knowledge, we applied the DST to combine evidence from multiple sources. Through this research we demonstrated that the Dempster-Shafer Method provides a solid approach for multi-sensor fusion.

6.2   Future Work

The research presented here showed many encouraging results for the application of the Dempster-Shafer Method. However, these results are still preliminary. Future work is required. Recall the basic probability assignments are user-defined. Thus with further research they can be modified to produce better results. Particularly this is applicable to Case 4 Run 9 in Section 3.5.4 where this method did not provide good positioning data. Further refinement on (11) is needed. Also Chapters IV and V only have results from applying the DST. Additional fusion methods should be used to determine how well the Dempster-Shafer Method performed. Next, in Chapter IV due to the long outage of the GPS, determining the exact location of the cart was difficult. Obtaining data from a third sensor, such as the imaging camera, would allow a more in-depth analysis of this method's performance. Finally, no real sensor data was obtained for Chapter V. It is possible to place a single camera or multiple cameras at different angles in a high traffic area and to gather a series of images for analysis.

Bibliography

1. Abidi, Mongi A. and Rafael C. Gonzalez. Ed. *Data Fusion In Robotics and Machine Intelligence.* San Diego: Academic Press, 1992.

2. Aregui, Astride. "Constructing Predictive Belief Functions from Continuous Sample Data Using Confidence Bands." *Fifth International Symposium on Imprecise Probability: Theories and Applications.* Prague: 2007.

3. Betz, John W, Jerry L. Prince, and Martin G. Bello. "Representation and Transformation of Uncertainty in an Evidence Theory Framework." *IEEE Computer Society Conference on Computer Vision and Pattern Recognition.* 646-652. San Diego CA: June 1989.

4. Bhattacharya, Prabir. Professor, College of Engineering and Applied Science, University of Cincinnati. Email. 22 November 2011.

5. Boston, J.R. "A Signal Detection System Based on Dempster-Shafer Theory and Comparison to Fuzzy Detection." *IEEE Transactions on Systems, Man, and Cybernetics-Part C: Applications and Reviews*, 30: 45-51 (February 2000).

6. Chaabane, Salim Ben, Farhat Fnaiech, Mounir Sayadi, and Eric Brassart. "Estimation of the Mass Function in the Dempster-Shafer's Evidence Theory using Automatic Threshold for Color Image Segmentation." *2nd International Conference on Signals, Circuits and Systems.* 1-5. Monastir, Tunisia: November 2008.

7. Chen, Thomas M. and Varadharajan Venkataramanan. "Dempster-Shafer Theory for Intrusion Detection in Ad Hoc Networks." *IEEE Internet Computing*, 9: 35-41 (November 2005).

8. Chen, Qi and Uwe Aickelin. "Anomaly Detection Using the Dempster-Shafer Method." http://arxiv.org/ftp/arxiv/papers/0803/0803.1568.pdf. 15 May 2011.

9. Chunhong, Jiang and Chen Zhe. "Multisensor Fusion Based on Decision-making in INS/CCD/SAR Integrated Systems." *IEEE Region 10 Conference on Com-*

puters, Communications, Control and Power Engineering, 1: 695-698 (October 2002).

10. Dezert, Jean, Albena Tchamova, Florentin Smarandache, and Pavlina Konstanti-nova. "Target Type Tracking with PCR5 and Dempster's Rules: A Comparative Analysis." *9th International Conference on Information Fusion*. 1-8. Florence: July 2006.

11. Dugan, Sheila A. and Krishna P. Bhat. "Biomechanics and Analysis of Running Gait." *Physical Medicine and Rehabilitation Clinics of North America*, 16: 603-621 (August 2005).

12. "Excessive Pronation Pt 1." *London Personal Trainer.* 2012. http://www.juranring.co.uk/2010/11/foot1/. 27 January 2012.

13. Faux, F. and F. Luthon. "Robust face tracking using colour Dempster-Shafer fusion and particle filter." *9th International Conference on Information Fusion.* Florence: July 2006.

14. Fenton, N., et al. "Assessing dependability of safety critical systems using diverse evidence." *IEE Proceedings Software*, 145: 35-39 (February 1998).

15. Fisher, Kenneth. Deputy Director, ANT Center, AFIT. Personal Conversation. 9 January 2012.

16. "Gait." *Merriam-Webster's Collegiate Dictionary.* 10th edition. 2002.

17. "Gait Analysis." *The Free Dictionary by Farlex.* 2012. http://medical-dictionary.thefreedictionary.com/gait+analysis. 18 January 2012.

18. "Gait Cycle." http://www.ncbi.nlm.nih.gov/books/NBK27235/. 25 January 2012.

19. Gao, Huisheng, Jing Zhu, and Congcong, Li. "The Analysis of Uncertainty of Network Security Risk Assessment Using Dempster-Shafer Theory." *Twelfth International Conference on Computer Supported Cooperative Work in Design.* 754-759. Xi'an: April 2008.

20. Gilliss, Adam C., Randel L. Swanson II, Deanna Janora, and Venkat Venkataraman. "Use of Osteopathic Manipulative Treatment to Manage Compensated Trendelenburg Gait Caused by Sacroiliac Somatic Dysfunction." *The Journal of the American Osteopathic Association*, 110(2): 81-86 (1 February 2010). http://www.jaoa.org/content/110/2/81/F3.expansion. 27 January 2012.

21. Gordon, Jean and Edward H. Shortliffe. "The Dempster-Shafer Theory of Evidence." *Readings in Uncertain Reasoning*. Ed. Glenn Shafer and Judea Pearl. CA: Morgan Kaufmann Publishers, 1990.

22. Haenni, Rolf. "Shedding New Light on Zadeh's Criticism of Dempster's Rule of Combination." *7th International Conference on Information Fusion*. 879-884. July 2005.

23. Hall, David L. and Sonya A.H. McMullen. *Mathematical Techniques in Multisensor Data Fusion* (2nd edition). Norwood MA: Artech House, 2004.

24. Hegarat-Mascle, Sylvie Le, Isabelle Bloch, and D. Vidal-Madjar. "Application of Dempster-Shafer Evidence Theory to Unsupervised Classification in Multisource Remote Sensing." *IEEE Transactions on Geoscience and Remote Sensing*, 35: 1018-1031 (July 1997).

25. Ivanic, Curb. "Running Stride Length." http://www.corerunning.com/stride_length.html. 18 January 2012.

26. Jing, Jiang, Guo Jing, Luo Peng Fei, Liu Fu Sheng, and Sun Zhong Kong. "Multisensor Multiple-Attribute Data Association." *CIE International Conference of Radar*. 393-396. Beijing: October 1996.

27. "Joint Function & GAIT Analysis." http://wings.buffalo.edu/eng/mae/courses/417-517/Orthopaedic%20Biomechanics/lecture%204.pdf. 18 January 2012.

28. Kay, Rakowsky Uwe. "Fundamentals of the Dempster-Shafer Theory and its applications to system safety and reliability modeling." *International Journal of Reliability Quality and Safety Engineering*, 14: 579-592 (2007).

29. Klein, John, Christele Lecomte, and Pierre Miche. "Preceding car tracking using belief functions and a particle filter." *19th International Conference on Pattern Recognition.* 1-4. Tampa FL: December 2008.

30. Klein, Lawrence A. *Sensor and Data Fusion: A Tool for Information Assessment and Decision Making.* Bellingham WA: SPIE, 2004.

31. Kouemou, Guy, Christoph Neumann, and Felix Opitz. "Exploitation of Track Accuracy Information in Fusion Technologies for Radar Target Classification using Dempster-Shafer Rules." *12th International Conference on Information Fusion.* 217-223. Seattle WA: July 2009.

32. Kovacs, Mark. "Speed Training: Linear Acceleration." http://www.nsca-lift.org/HotTopic/download/Speed%20Training.pdf. 18 January 2012.

33. Lee, Jimson. "Velocity = Contact Length / Ground Contact Time." 25 March 2011. http://speedendurance.com/2011/03/25/velocity-contact-length-ground-contact-time/. 18 January 2012.

34. Liu, Zheng, David S. Forsyth, Mir-Saeed Safizadeh, and Abbas Fahr. "A Data-Fusion Scheme for Quantitative Image Analysis by Using Locally Weighted Regression and Dempster-Shafer Theory." *IEEE Transactions on Instrumentation and Measurement*, 57: 2554-2560 (November 2008).

35. Mahler, Ronald P.S. *Statistical Multisource-Multitarget Information Fusion.* Norwood MA: Artech House, 2007.

36. "Measurement and evaluation of the human dynamic characteristics." http://www.dh.aist.go.jp/bodyDB/a/HQL-00-04e.html. 18 January 2012.

37. Mejdoubi, Mustapha, Driss Aboutajdine, Mounir Ait Kerroum, and Ahmed Hammouch. "Combining Classifiers using Dempster-Shafer Evidence Theory to Improve Remote Sensing Images Classification." *International Conference on Multimedia Computing and Systems.* 1-4. Ouarzazate: 2011.

38. Merlijn, Menno. "Gait parameters for identification purposes." June 2000. http://geradts.com/html/Documents/gait.htm. 18 January 2012.

39. Mourad, Farah, Hichem Snoussi, Fahed Abdallah, and Cedric Richard. "A Robust Localization Algorithm for Mobile Sensors Using Belief Functions." *IEEE Transactions on Vehicular Technology*, 60: 1799-1811 (May 2011).

40. Murphy, Robin R. "Dempster-Shafer Theory for Sensor Fusion in Autonomous Mobile Robots." *IEEE Transactions on Robotics and Automation*, 14: 197-206 (April 1998).

41. Pagac, Daniel, Eduardo M. Nebot, and Hugh Durrant-Whyte. "An Evidential Approach to Map-Building for Autonomous Vehicles." *IEEE Transactions on Robotics and Automation*, 14: 623-629 (August 1998).

42. Patton, Jim and Ellen Humphrey "'Normal' Gait Part of Kinesiology." http://www.smpp.northwestern.edu/~jim/kinesiology/partA_introGait.ppt.pdf. 18 January 2012.

43. Raquet, John, Ed. *ICD-ASPN1-01*. Revised 18 October 2011.

44. Raquet, John, Ed. *ICD-ASPN1-02*. Revised 18 October 2011.

45. Raquet, John, Ed. *ICD-ASPN1-03*. Revised 18 October 2011.

46. Raquet, John, Ed. *ICD-ASPN1-100*. Revised 30 November 2011.

47. Reineking, Thomas. "Particle filtering in the Dempster-Shafer Theory." *International Journal of Approximate Reasoning*, 52: 1124-113 (2011).

48. Rey, M., J.K.E. Tunaley, and T. Sibbad. "Use of the Dempster-Shafer Algorithm for the Detection of SAR Ship Wakes." *IEEE Transactions on Geoscience and Remote Sensing*, 31: 1114-1118 (September 1993).

49. Ribo, Miguel, Axel Pinz. "A comparison of three uncertainty calculi for building sonar-based occupancy grids." *Robotics and Autonomous Systems*, 35: 201-209 (2001).

50. Sarkar, Anjan, et al. "Landcover Classification in MRF Context Using Dempster-Shafer Fusion for Multisensor Imagery." *IEEE Transactions on Image Processing*, 14: 634-645 (May 2005).

51. Sarkar, Manish. "Modular Pattern Classifiers: A Brief Survey." *IEEE International Conference on Systems, Man, and Cybernetics*, 4: 2878-2883 (October 2000).

52. Seraji, Homayoun and Navid Serrano. "A Multisensor Decision Fusion System for Terrain Safety Assessment." *IEEE Transactions on Robotics*, 25: 99-108 (February 2009).

53. Shafer, Glenn. *A Mathematical Theory of Evidence*. New Jersey: Princeton University Press, 1976.

54. Smearcheck, Mark. Research Engineer, ANT Center, AFIT. Email. 1 February 2012.

55. Valin, Pierre, Pascal Djiknavorian, and Eloi Bosse. "A Pragmatic Approach for the use of Dempster-Shafer Theory in Fusing Realistic Sensor Data." *Journal of Advances in Information Fusion*, 5: 32-40 (June 2010).

56. "World Geodetic System." *Wikipedia: The Free Encyclopedia.* 2012. http://en.wikipedia.org/wiki/World_Geodetic_System. 30 January 2012.

57. Wu, Huadong, Mel Siegel, and Sevim Ablay. "Sensor Fusion Using Dempster-Shafer Theory II: Static Weighting and Kalman Filter-like Dynamic Weighting." *20th IEEE Instrumentation and Measurement Technology Conference.* 907-912. Vail CO: May 2003.

58. Xiong, Wei. "Analyzing a Paradox in Dempster-Shafer Theory." *Fifth International Conference on Fuzzy Systems and Knowledge Discovery.* 154-158. Jinan Shandong: October 2008.

59. Yager, Ronald R. "Decision Making Under Dempster-Shafer Uncertainties." *Classic Works of the Dempster-Shafer Theory of Belief Functions: Studies in Fuzziness and Soft Computing*, 219: 619-632 (2008).

60. Yang, Dakai, Baigen Cai, and Yifang Yuan. "An Improved Map-Matching Algorithm Used in Vehicle Navigation System." *IEEE Intelligent Transportation Systems*, 2: 1246-1250 (December 2003).

61. Yao, Junfeng, et al. "A New Evidence Combining Method Based on WAFCM and the Improved Weighted Average Method." *Journal of Computational Information Systems*, 7: 3955-3962 (2011).

62. Yao, Junfeng, et al. "A New Method of Information Decision-making Based on D-S Evidence Theory." *IEEE International Conference on Systems Man and Cybernetics*. 1804-1811. Istanbul: October 2010.

63. Yi, Zou, et al. "Multi-ultrasonic Sensor Fusion for Mobile Robots." *Proceedings of the IEEE Intelligent Vehicles Symposium*. 387-391. Dearborn MI: October 2000.

64. Young, Michael. "Maximal Velocity Sprint Mechanics." http://www.scarboroughtrack.com/sprintingmechanics.pdf. 18 January 2012.

65. Zervas, E., et al. "Multisensor data fusion for fire detection." *Information Fusion*, 12: 150-159 (2011).

66. Zhao, Wentao, Tao Fang, and Yan Jiang. "Data Fusion Using Improved Dempster-Shafer Evidence Theory for Vehicle Detection." *Fourth International Conference on Fuzzy Systems and Knowledge Discovery*. 487-491. Haikou: December 2007.

AFOSR/NE

REPORT DOCUMENTATION PAGE

1. REPORT DATE *(DD–MM–YYYY)*	2. REPORT TYPE	3. DATES COVERED *(From — To)*
03-2012	Master's thesis	May 2011 - Mar 2012

4. TITLE AND SUBTITLE	5a. CONTRACT NUMBER
A Dempster-Shafer Method for Multi-Sensor Fusion	5b. GRANT NUMBER
	5c. PROGRAM ELEMENT NUMBER

6. AUTHOR(S)	5d. PROJECT NUMBER
Foley, Bethany G., Captain, USAF	5e. TASK NUMBER
	5f. WORK UNIT NUMBER

7. PERFORMING ORGANIZATION NAME(S) AND ADDRESS(ES)	8. PERFORMING ORGANIZATION REPORT NUMBER
Air Force Institute of Technology Graduate School of Engineering and Management (AFIT/EN) 2950 Hobson Way WPAFB OH 45433-7765	AFIT/GAM/ENC/12-03

9. SPONSORING / MONITORING AGENCY NAME(S) AND ADDRESS(ES)	10. SPONSOR/MONITOR'S ACRONYM(S)
Air Force Office of Scientific Research Sensing Surveillance and Navigation Attn: Jon A. Sjogren 875 N. Randolph Arlington, VA 22203-1768 (703) 696-6564 (DSN: 426-6564)	11. SPONSOR/MONITOR'S REPORT NUMBER(S)

12. DISTRIBUTION / AVAILABILITY STATEMENT

APPROVED FOR PUBLIC RELEASE, DISTRIBUTION UNLIMITED

13. SUPPLEMENTARY NOTES

14. ABSTRACT

The Dempster-Shafer Theory, a generalization of the Bayesian theory, is based on the idea of belief and as such can handle ignorance. When all of the required information is available, many data fusion methods provide a solid approach. Yet, most do not have a good way of dealing with ignorance. In the absence of information, these methods must then make assumptions about the sensor data. However, the real data may not fit well within the assumed model. Consequently, the results are often unsatisfactory and inconsistent. The Dempster-Shafer Theory is not hindered by incomplete models or by the lack of prior information. Evidence is assigned based solely on what is known, and nothing is assumed. Hence, it can provide a fast and accurate means for multi-sensor fusion with ignorance. In this research, we apply the Dempster-Shafer Theory in target tracking and in gait analysis. We also discuss the Dempster-Shafer framework for fusing data from a Global Positioning System (GPS) and an Inertial Measurement Unit (IMU) sensor unit for precise local navigation. Within this application, we present solutions where GPS outages occur.

15. SUBJECT TERMS

Dempster-Shafer Theory, belief functions, data fusion, uncertainty, stochastic process

16. SECURITY CLASSIFICATION OF:			17. LIMITATION OF ABSTRACT	18. NUMBER OF PAGES	19a. NAME OF RESPONSIBLE PERSON
a. REPORT	b. ABSTRACT	c. THIS PAGE			Aihua W. Wood (ENC)
U	U	U	UU	117	**19b. TELEPHONE NUMBER** *(include area code)* (937) 255-3636 x 4272